This is to certify that the
dissertation entitled

NANOSTRUCTURING OF HIGHLY AROMATIC GRAPHENE NANOSHEETS – FROM OPTOELECTRONICS TO ELECTROCHEMICAL ENERGY STORAGE APPLICATIONS

presented by

Sanjib Biswas

has been accepted towards fulfillment
of the requirements for the

Doctoral degree in CHEMICAL ENGINEERING

Lawrence T. Drzal

Lawrence T. Drzal
Major Professor's Signature

March 2nd 2010

Date

MSU is an Affirmative Action/Equal Opportunity Employer

NANOSTRUCTURING OF HIGHLY AROMATIC GRAPHENE NANOSHEETS – FROM OPTOELECTRONICS TO ELECTROCHEMICAL ENERGY STORAGE APPLICATIONS

By

Sanjib Biswas

A DISSERTATION

Submitted to
Michigan State University
in partial fulfillment of the requirements
for the degree of

DOCTOR OF PHILOSOPHY

Chemical Engineering

2010

ABSTRACT

NANOSTRUCTURING OF HIGHLY AROMATIC GRAPHENE NANOSHEETS – FROM OPTOELECTRONICS TO ELECTROCHEMICAL ENERGY STORAGE APPLICATIONS

By

Sanjib Biswas

The exceptional electrical properties along with intriguing physical and chemical aspects of graphene nanosheets can only be realized by nanostructuring these materials through the homogeneous and orderly distribution of these nanosheets without compromising the aromaticity of the native basal plane. Graphene nanosheets prepared by direct exfoliation as opposed to the graphene oxide route are necessary in order to preserve the native chemical properties of graphene basal planes. This research has been directed at optimally combining the diverse physical and chemical aspects of graphene nanosheets such as particle size, surface area and edge chemistry to fabricate nanostructured architectures for optoelectronics and high power electrochemical energy storage applications.

In the first nanostructuring effort, a monolayer of these ultrathin, highly hydrophobic graphene nanosheets was prepared on a large area substrate via self-assembly at the liquid-liquid interface. Driven by the minimization of interfacial energy these planar graphene nanosheets produce a close packed monolayer structure at the liquid-liquid interface. The resulting monolayer film exhibits high electrical conductivity of more than 1000 S/cm and an optical transmission of more than 70-80% between wavelengths of 550 nm and 2000 nm making it an ideal candidate for optoelectronic applications. In the second part of this research, nanostructuring was used to create a configuration suitable

for supercapacitor applications. A free standing, 100% binder free multilayer, flexible film consisting of monolayers of graphene nanosheets was prepared by utilizing the van der Waals forces of attraction between the basal plans of the graphene nanosheets coupled with capillary driven and drying-induced collapse. A major benefit in this approach is that the graphene nanosheet's attractive physical and chemical characteristics can be synthesized into an architecture consisting of large and small nanosheets to create an aligned network designed to maximize device performance. Monolayers of large sized graphene nanosheets function as highly electrically conducting current collectors within a mesoporous network of smaller graphene nanosheets for improved rate capability of the electrical double layer capacitor (EDLC) electrode. This nano-architecture produces an electrode with superior performance for high power EDLC applications: a high frequency capacitative response; a nearly rectangular cyclic voltammogram at a scanning rate of 1000 mV/sec; a rapid current response; small equivalent series resistance (ESR); and fast ionic diffusion. Integration of this nanostructured graphene nanosheet architecture with conductive polymers or metal oxide nanostructures was also investigated to produce similar multilayered structures for electrochemical energy storage applications.

These inexpensive graphene nanosheets coupled with this facile and robust nanostructuring process make both this new material and method highly advantageous for many potential applications ranging from optoelectronics to high power electrochemical energy storage applications.

To my parents

ACKNOWLEDGMENTS

I am chiefly indebted to my advisor professor Lawrence T. Drzal for the patience, support and sincerity he showed to me during the completion of my dissertation. I am likewise thankful to my committee members, professors Robert Y. Ofoli, Tim Hogan and Ilsson Lee and to the department of Chemical Engineering and Materials Science.

I am grateful to all the research staff in the Composite Materials and Structures Center. I would like to thank Mike Rich, Per Askaland, Brian Rook, Ed Drown, Bob Jurek, Wanjun Liu, Hwanman Park, Toshiya Kamae, Xiaobing Li, and Hazel-Ann Hosein for their generous assistance. I would also like to thank Hiroyuki Fukushima and Inhwan Do for their tireless support to my research. Karen Lillis and Inger Weitlauf were of great to help me as well. My special thanks goes to everyone in the EB1105 office to Pat, Xian, Dana, Anchita, Steve, Tao, Jingley, Debkumar, Salil, Huang, Frederic and Madhu for encouragement, coffee breaks and fun.

Finally, I wish to thank my parents for their unconditional love and unwavering support in the course of my studies and in my life. They have always stood by my side, especially in the strenuous times during my studies.

TABLE OF CONTENTS

LIST OF TABLES

LIST OF FIGURES

CHAPTER 1

INTRODUCTION

Graphene, a single layer two dimensional aromatic macromolecule, is prevalent in one of the most abundant elements on earth, graphite [1-6]. Graphite is made of stacks of single graphene layers, held together by van der Waals force of attraction [1-6]. A single layer graphene can be considered as a two dimensional lattice, one atom thick, where the covalently bonded carbon atoms are arranged in a honeycomb structure [1-6]. Strong sp^2 bonded network of carbon atoms inside the graphene plane creates a chemically inert and thermally stable aromatic macromolecule [1-6]. The delocalized π-electron structure of graphene is unique and this semimetal material has the unusual feature in which the conduction and valence band meet at a point to cause a zero band gap [1,2, 8-10]. The charge carrier velocity in graphene is constant and the electrons move as if they have no mass [8-10]. This two dimensional macromolecular structure exhibits an in plane electrical resistivity as low as 50×10^{-6} Ω cm [8,11].

Exfoliated graphite nanoplatelets, xGnP, consists of stacks of single layers of graphene with thicknesses ranging from 1 to 15 nm [12]. The lateral dimension of these nanoplatelets can be controlled from submicron to more than 50 micrometers [12]. Platelets with an average lateral dimensions 1 and 15 μm are known as xGnP-1 and xGnP-15 respectively [12]. In addition to the unique electronic properties, the mechanical stiffness of individual nanoplatelets is comparable to that of carbon nanotubes. While the theoretical tensile modulus is more than 1000 GPa, the low density of only 2.0 gm/cm^3

makes xGnP light in weight yet ultra stiff [7,12]. The breaking strength of graphene is 200 times stronger than steel [56]. The in plane thermal conductivity of a single and multilayer layer graphene was reported to be more than 3000 W/mK, which is much higher than any other allotrope of carbon Where as the weak interlayer coupling results in low thermal conductivity of graphite of at least four order of magnitude less in the c-axis than the graphene basal plane [13-14,55]. This unique combination of electronic, thermal and mechanical properties demonstrates tremendous potential of exfoliated graphite nanoplatelets in various applications such as nanoelectronics, electrochemical energy storage devices or in polymeric nanocomposite materials [1-7].

1.1 Background and Literature review:

1.1.1 Carbon nanomaterials for optoelectronics application

1.1.1.1 Current state and materials:

Electrically conductive and optically transparent films are essential components of optoelectronics [15-19]. Organic photovoltaic cells, dye sensitized solar cells and display devices ubiquitously require a transparent and electrically conductive electrode [15-19]. Electrically conductive films are also important for electrostatic charge dissipation coating and sensor devices. Indium tin oxide (ITO) and fluorine tin oxide (FTO) are widely used as optically transparent and electrically conductive material for the above mentioned applications [15-19]. Both ITO and FTO exhibit an optical transparency of more than 80% in the visible spectrum of electromagnetic radiation [15-19]. The average electrical conductivity of 100 nm thick ITO coated film is 1000 S/cm or more [15-16].

However, the use of these metal oxide electrodes are increasingly challenging considering i) the limited availability of indium ii) thermal degradation at a temperature more than 200 C iii) chemical degradation in the presence of acid or base iv) poor infrared transparency v) susceptibility to ion diffusion with polymer and vi) current leakage due to structural defects [18-19]. Therefore, inexpensive material having high chemical and thermal stability coupled with high electrical conductivity and optical transparency should be an ideal replacement for these metal oxides.

1.1.1.2 Graphene nanosheets and other carbon nanomaterials for optoelectronics applications:

Over the last decade, a significant amount of research has been conducted on carbon nanotubes [20-21]. The electronic, thermal and mechanical properties of carbon nanotubes are very similar to those of parent graphene sheet [21]. However, the application of this novel material as optically transparent and electrically conductive electrodesdepends on its electronic properties. The electronic properties of carbon nanotubes are solely determined by the chiral vector of the rolled graphene sheet. Among the three different configurations chiral, armchair and zigzag, armchair is the only configuration which shows a metallic character and excellent electronic properties [20-21]. Separating these high purity metallic nanotubes from a mixture of other configurations is very challenging and the resulting product is also very expensive [20-21]. Such configurational asymmetry does not arise for a two dimensional graphene layer and the material is nearly defect free [2-3]. However, the major challenge remains in

transferring this novel electronic property from the nanoscale to the macroscale for realistic technological applications.

Over the last four years, a graphite oxide route has been gaining popularity as a method not only to create single or multilayer graphene sheets but also to achieve a stable colloidal dispersion in water [22-26]. Hummers method and the Staudenmaier method are two ways to produce sheets of graphite oxides through severe oxidation of natural graphite [22-26]. In this technique, natural graphite is treated with a strong oxidizing agent such as potassium chlorate, sodium nitrate, potassium permanganate or potassium dichromate in the presence of fuming sulfuric acid and nitric acid mixture [22-26]. This severe oxidation introduces hydroxyl, epoxy and carboxyl groups in the aromatic basal plane of graphene and the sp^2 carbon becomes sp^3 hybridized [22-26]. Introduction of these oxygen functional groups causes the graphene oxide layers to 'wrinkle' which aids in their separation and subsequent chemical exfoliation in water results in a stable dispersion of single or multilayer graphene nanosheets. The presence of hydroxyl, carboxylic acid and epoxy groups in the basal plane of graphite oxide makes it possible to get a stable colloidal dispersion in water [22-26]. Such a stable dispersion of graphite oxide allows these nanosheets to be deposited on hydrophilic substrates either by dip coating or spin coating processes [22-26]. Xuan et al. has reported a dip coating process from the stable dispersion of graphite oxide to prepare ultrathin film on glass substrate of various thicknesses from 5 to 20 nm [22]. Hector et al. used the same stable dispersion of graphite oxide at various concentrations in water to spin coat these nanosheets on the glass substrate of various thicknesses from 5 to 50 nm [23]. In a different approach, Supinda et al. took the advantage of highly hydrophilic character of graphite oxide

nanosheets to prepare graphite oxide silica nanocomposite thin film from tetramethyl orthosilicate (TMSO) [26].

Vacuum filtration is another technique to create ultra thin to multilayer free standing film of graphite oxide. In this approach a stable dispersion of graphite oxide at various concentrations is vacuum filtered through alumina filter membrane or cellulose ester membrane [25,26]. Goki et al. has successfully prepared a flexible ultrathin layer of graphite oxide film of less than 5 nm thickness by vacuum filtration through cellulose ester membrane [24]. The film was removed from the filter paper by pressing and drying the film against a solid hydrophilic substrate for more than 10 hrs [24]. Following the same approach Dmitriy et al. vacuum filtered a highly concentrated colloidal dispersion of graphite oxide to prepare a multilayer free standing film, popularly known as "graphite oxide paper" [25]. The presence of strong interlayer hydrogen bonding between graphite oxide nanosheets creates a multilayer free standing film, which shows exceptional mechanical properties having a tensile modulus of more than 32 GPa [25].

However, a shortcoming of the above mentioned process is that the graphite oxide films are electrically non-conductive. In the oxidized graphite, the presence of sp^3 hybridized carbon atom reduces the aromaticity of graphene basal plane and leaves graphite oxide electrically nonconductive [4-6,22-26]. Therefore, reduction of oxygen functional groups is essential to regain the aromatic character of the basal plane [4-6,22-26]. This is done by chemical or thermal reductive treatment on the ultrathin or multilayer free standing film of graphite oxide [4-6, 22-26]. In the chemical reduction treatment, the prepared film of graphite oxide is treated with strong reducing agent such as hydrazine monohydrate for more than 24 hours to reduce the oxygen functional groups [4-6, 22-26]. In thermal

reductive treatment, the graphitization of graphite oxide film is carried out either in inert atmosphere or in vacuum at a temperature as high as 1100 C [23]. At this high temperature graphitization occurs with rapid evolution of carbon monoxide from graphite oxide. This severe oxidation and reduction treatment to produce graphite oxide and graphene, however, leave a large concentration of defects on the graphene basal plane as compared to pure natural graphene [22-24]. Nevertheless, with the regeneration of partial aromatic character, the film attains electrically conductivity [22-24]. The average sheet resistance of the graphene film was reported as 10^3-10^6 Ω/sq corresponding to a electrical conductivity 750 S/cm [22-23]

The optical transparency of reduced graphite oxide or graphene film is a linear function of film thickness. A recent report has revealed that a single layer graphene absorbs around 2.3% of the white light due to its unique electronic structure and each additional layer increases the absorption by 2.3% [27]. Therefore with increasing thickness, the graphene film transparency decreases with enhanced white light absorption from the visible spectrum of electromagnetic radiation. For ultrathin graphene film, prepared from graphite oxide route as mentioned earlier, the optical transparency was reported from 60% to 80% at 500 nm wavelength [22-26]. Such film transparency was only obtained with a film thickness of less than 10 nm [22-26].

The graphite oxide route to produce transparent and electrically conductive electrode or multilayer free standing film electrode is chemically hazardous and expensive [4-6]. In addition, severe oxidation of natural graphite and reduction of graphite oxide to graphene produces defects in the graphene basal plane and it is very difficult to retrieve the complete aromatic character [4-6]. Moreover this oxidation and reduction process require

highly reactive chemicals such as potassium chlorate, mixture of fuming nitric and sulfuric acid and hydrazine monohydrate [4-6]. Thus the process is chemically hazardous and in some instances the chemical oxidation can also result in explosion and release of highly toxic gas such as chlorine dioxide. Exfoliated graphite nanoplatelets (xGnP), developed in the Drzal Group on the other hand, are prepared from microwave exfoliation of acid intercalated graphite [12]. The process is simple and much less hazardous than graphite oxide route [12]. These xGnP nanoplatelets are chemically highly pure and the aromatic character is completely retained without requiring any oxidation or reduction of graphene basal plane [12]. An XPS analysis of xGnP reveals an oxygen atomic concentration of less than 6%, which is negligible compared to graphite oxide. However, xGnP is highly hydrophobic and it is not water processable like graphite oxide [28]. Therefore, understanding the fundamentals of dispersion and subsequent fabrication of these highly hydrophobic nanosheets onto a planar solid substrate is the key to the successful transformation of novel properties of these nanoscale materials to macroscale technological applications.

1.1.2 Graphene based electrochemical energy storage applications:

With increasing demand for alternative energy resources such as solar power or wind energy the need for energy storage systems are also on the rise [29]. Hence there is a noticeable development on the studies of electrochemical supercapacitors and batteries over the last decade [29]. In comparison to batteries, electrochemical capacitors can deliver all the stored energy in few seconds and thus it finds applications for high power

delivery operations [29-33]. Another major advantage of electrochemical capacitors as compared to batteries is there high cycle life. These capacitors can run for more than 10^5 cycles with minimum degradation of their electrical performances [30-33]. Electrochemical capacitors are widely used in different market applications. These are used as power buffer to the batteries in small devices such as toys, cameras, video recorders or in mobiles phone [29-33]. Tools, which require maximum power delivery in minimum time such as electrical cutters or screwdrivers, widely use electrochemical capacitors with the cycle life of these capacitors more than that of the tools [29-33]. In large devices, these high power capacitors find applications in electrically operated emergency doors in jumbo jets such as Airbus A380 [29]. In the automobile market, the electrochemical capacitors are now considered as a backup system to the lithium ion batteries to provide high power during fast acceleration and breaking energy recovery [29-33].

1.1.2.1 Working principle of electrochemical capacitors:

An electrochemical capacitor is presented in Figure 1.1, where two electrically conductive electrodes are immersed in an ionic electrolyte system.

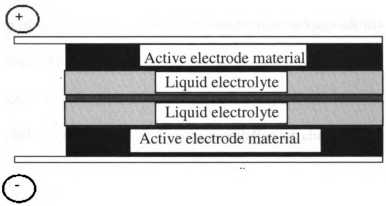

Figure 1.1: Schematic diagram of electrochemical capacitor

The energy storage in an electrochemical capacitor is governed by the electrical and ionic charge separation at the electrode electrolyte interface. For a plane capacitor, the capacitance is given by the equation [34],

$$C = A\varepsilon/d$$

Where 'A' is the area of the individual parallel plates separated by a distance 'd' and ε is the dielectric constant of the medium. The charge accumulation for electric double layer is similar to that of the plate capacitor. However, the opposite charges are not separated by dielectric media rather the charge accumulates at the interface between the solid electrode and liquid electrolyte [34]. In comparison to the working principle of batteries, an electrochemical double layer capacitor does not involve any chemical reaction [34]. The transfer of valence electrons across the electrode-electrolyte interface provides higher charge storage density for batteries as compared to electrochemical capacitors where an electrical double layer is formed at the electrode electrolyte interface involving conduction band electrons only. Thus the energy density for electrochemical capacitors is

lower than batteries. However, low electronic and ionic resistance associated with the formation of the electrical double layer makes these devices ideally suited for high power applications [34].

As a function of potential, an excess or deficiency of electrons develops a charged layer on the solid electrode surface. This accumulation of charge is then counterbalanced by the oppositely charged ions from the ionic liquid electrolyte. The electrical double layer has been explained by different models such as Helmholtz model, Gouy-Chapman model, and Gouy-Chapman-Stern model [34-36]. The formation of electrical double layer is shown in Figure 1.2.

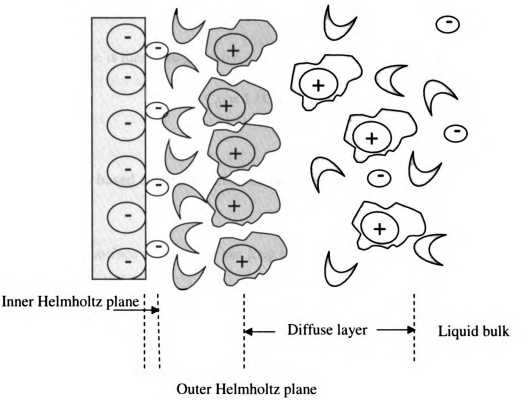

Figure 1.2: Electrical double layer model showing the charge distribution of ionic counterparts in the solvent medium defined by different charged planes [34]

The inner layer is known as Helmholtz plane or Stern layer [34-36]. The inner Helmholtz plane consists of specifically adsorbed ions and the outer plane corresponds to the closest distance to which the solvated ions can approach towards the charged electrode surface [34-36]. The stern layer consists of inner and outer Helmholtz plane where the potential decreases linearly with distance [34-36]. Outside the stern layer the potential decreases exponentially with distance in the three dimensional diffusive layer [34-36]. The thickness of the three dimensional diffusive layer is determined by the concentration of the solvated ions. The double layer capacitance is made up from the parallel combination of total charge density obtained from non specifically adsorbed ions in the stern layer (C_H) and the excess charge density in the diffuse layer (C_{diff}) [34-36]. The total double layer capacitance is therefore given by,

$$1 / C_{dl} = 1 / C_H + 1 / C_{diff}$$

1.1.2.2 Carbon based electrochemical capacitors and graphene:

Activated high surface area carbon has long been used as an active electrode material for electrochemical supercapacitor. The capacitance contribution from the aromatic basal plane area of graphitic carbon is an average 10-20 $\mu F/cm^2$, where as the oxygen functional group rich edge area contributes 50-70 $\mu F/cm^2$ [34,39]. For activated carbon, the high surface area micro porous carbon presents a large interfacial area between the electrode and the electrolyte [37-39]. However, the large inter particle electronic resistance associated with the small particle size of activated carbon restricts the high rate

capability of these electrodes [37-39]. Recent progress on carbon nanotubes based electrochemical supercapacitors has shown high specific capacitance and rapid charge discharge characteristics for high power applications [40,41]. The electrodes from carbon nanotubes are usually prepared by vacuum filtration of dispersed nanotubes in a liquid medium or by directly growing carbon nanotubes on a metal current collector surface. While the fibrous network of vacuum filtered sample offers easy access for ionic electrolytes to reach the porous network, the vertically grown carbon nanotubes on the other hand provides much larger inter tube distance for quick access to the electrolyte ions. At the same time, the vertically grown carbon nanotubes have the inherent advantage of facile electronic conduction from direct attachment of individual nanotubes on the metal current collector surface [40-43]. Thus in addition to high surface area the improved electronic conduction for carbon nanotubes based electrodes offers high specific capacitance and rapid charge discharge characteristics [40-43].

For graphene based electrodes, the high surface area material is prepared by the graphite oxide route. The average surface area of graphite oxide is more than 700 m^2/g [44,45]. However, the material is non conductive as discussed earlier. The material is reduced back to chemically modified graphene (CMG) to make it electrically conductive. Chemically modified graphene has also been tried as an electrode material for electrochemical capacitors. This material exhibits high specific capacitance of an average 120 F/g in aqueous electrolyte [44-48]. However, the charge discharge characteristics can not match the carbon nanotube based electrodes due to increased electronic resistivity from severe oxidation and reduction of aromatic graphene basal plane [44-48].

Exfoliated graphene nanosheets (xGnP), on the other hand, are highly aromatic and therefore highly electrically conductive. Moreover, the large particle dimension creates minimum inter particle contact resistance over large macroscopic areas. In addition, the attachment of oxygen functional groups on the edges of these nanosheets can be easily manipulated by controlling the size. With decreasing particle size, the edge to basal plane area increases with corresponding increase in the amount of oxygen functional groups bound to the active edge sites. With the edge sites contributing more towards the total capacitance of the system, a multilayered nano architecture can be developed with the large sized nanosheets providing fast electronic conduction for rapid charge discharge characteristics for high power electrochemical capacitor applications.

1.1.2.3 Graphene based pseudocapacitor:

The specific capacitance of double layer electrochemical capacitors depends on the available surface area. Even with high surface area material, the inaccessibility of ionic electrolytes to the micro porous structure often limits the specific capacitance to reach the theoretical limit. As compared to electrostatic double layer formation, for pseudocapacitors the capacitance originates from the faradic charge transfer reactions [29,34]. Similar to batteries, the charge transfer takes place across the interface rather that at the interface. Here the capacitance, C is a direct function of the extent of accumulated charge, Q as a function of applied potential V [29,34]

$$C = \delta(\Delta Q) / \delta(\Delta V)$$

For pseudocapacitors, the faradic charge transfer across the interface requires the active electrode material to be redox active. Since the valence electrons are required to participate in the faradic charge transfer reaction, more electrons are involved during the pseudocapacitative charge transfer mechanism as compared to double layer electrostatic charge storage mechanism [29,34]. Therefore, much higher capacitance is obtained from a pseducapacitor as compared to a layer capacitor. Conductive polymers such as polypyrrole or polyaniline are typical examples of pseudocapacitative materials [49-54]. The π conjugated structure of these polymers imparts good electrical transport properties in the oxidized or the reduced state [34]. In the oxidized state, with the withdrawal of electrons the conductive polymer is known as a p-type polymers whereas in the reduced state with the injection of excess electrons the polymer is said to be n-type [34]. However, the concept of p doping or n doping is different from that of semiconductor. Instead of doping the material with electron deficient or electron rich atoms, the conductive polymers are electrochemically oxidized or reduced to create positive or negative charged sites on the polymer backbone [34]. The charge developed under applied potential is counter-balanced by the ions present in the liquid electrolyte. The charge storage mechanism for conductive polymers is shown in Figure 1.3.

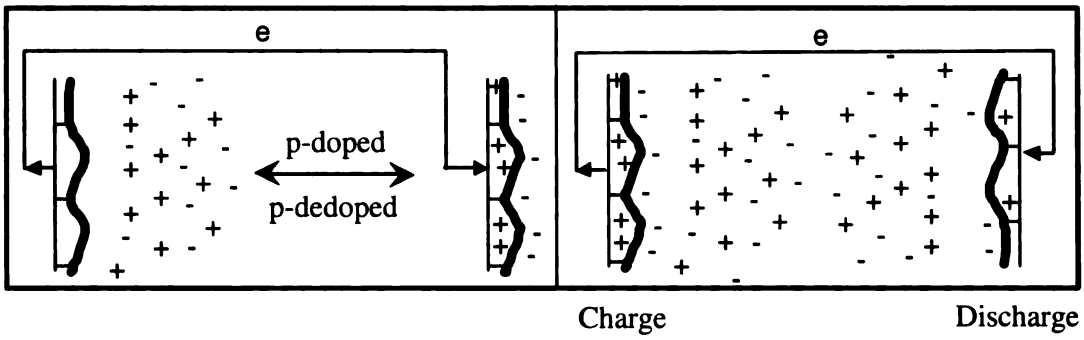

Figure 1.3: Representative mechanism of electrochemical oxidation and doping of conductive polymer chain to a p-doped state and corresponding counter charge balance from oppositely charged ions from the solution [34]

As explained in Figure 1.3, during the p doping process, electrons are withdrawn through an external circuit to create an electrical double layer with the oppositely charged ions in the electrolyte solution. In the reverse cycle, the total accumulated charge gets completely discharged with p-dedoping of the polymer backbone. Either the p-doped or n-doped configuration is stable from the resonating π conjugated structure of the polymer backbone [34].

However, the electrochemical cyclic stability of these polymers is not as good compared to a carbon based electrical double layer capacitor and the cycle life of pseudocapacitors are at least one order of magnitude smaller [49-54]. The degradation of this electrical property with increasing electrochemical cycles is a major concern in conductive polymer based pseudocapacitors [49-54].

For the graphene-based pseudocapacitor in this research, we have combined the exfoliated graphene nanosheets with a conductive polymer in a layered architecture to investigate the effect of enhanced charge transfer mechanism from strong van der Waals

force of attraction between the aromatic graphene basal plane and π conjugated polymer backbone on the cyclic stability of this composite pseudocapacitor.

1.2 Dissertation Objective:

The aromatic purity of the graphene basal plane is essential to retain high electronic transport and exceptional in plane mechanical strength for diverse technological applications. In contrast, the edge area of graphene basal plane is not aromatic and sp^3 bound oxygen functional groups are found at the edges. Therefore, the physicochemical properties of these nanosheets are strongly affected by the ratio of edge to basal plane area. With decreasing particle size and increasing oxygen content, the dispersion of these nanosheets in common solvents such as water improves however at the cost of increasing interparticle resistance over large microscopic area for the fabricated devices. Large sized graphene nanosheets on the other hand offer minimum interparticle resistance over large macroscopic areas. However the high degree of aromaticity limits the formation of a stable dispersion of these nanosheets in common solvents such as water.

Different technological applications such as optoelectronics or electrochemical energy storage devices from graphene nanosheets require not only high electronic transport from highly aromatic graphene basal plane but also the ability to achieve high ionic accessibility depending on the extent of oxygen functional groups present at the edges. The ability to control the particle dimension, aromatic purity and oxygen functional groups of exfoliated graphene nanosheets presents us a unique opportunity to apply this

material for different technological applications. However, with changing particle dimension and chemical functionalities the solvent processability of these nanosheets changes and offers a new challenge to fabricate devices from the nanoscale to macroscale regime without altering the native chemical properties of the parent graphene basal plane. Utilizing these nanosheets for optoelectronics applications necessitates the fabrication of monolayer of highly aromatic large sized graphene nanosheets over large macroscopic areas for improved transparency and better electrical conductivity. On the other hand, electrochemical energy storage applications require an optimized and well ordered design of large and small sized nanosheets inside the bulk macroscopic configuration to maximize the device performances for desired applications.

In the first part of this dissertation, the results of an investigation into the effect of different physical and chemical forces such as capillary force, evaporation induced convective transport, liquid-liquid interfacial adsorption, van der Waals or electrostatic force of attraction and the role of aromatic purity on the fabrication of devices from the nanoscale to a bulk will be reported. The essential component of this research has been the fabrication of macroscopic devices from graphene nanoplatelets without altering the native chemical properties of the graphene basal plane. In the last part of this research report, I try to investigate the role of chemical functional groups at the edges of graphene nanosheets on the electronic, electrochemical capacitative and cyclic stability of the electrode for supercapacitors applications will be reported.

References:

1. Geim. A. K. and Novoselov. K. S., Nature Materials, 2007, 6, 183-191

2. Allen. M. J., Tung. V. c., And Kaner. R. B., Chemical Review, 2010, 110, 132-145

3. Rao. C. N. R., Sood. A. K., Subrahmanyam. K. S., Govindaraj. A., Angewandte Chemie-International Edition, 2009, 48, 7752-7777

4. Geim. A. K., Science, 2009, 324, 1530-1534

5. Ruoff, Rodney, Nature nanotechnology, 2008, 3, 10-11

6. Park, Sungjin; Ruoff, Rodney S., Nature Nanotechnology 2009, 4, 217-224

7. Gao. Y. W., Hao. P., Physica E-Low-Dimensional Systems & Nanostructures, 2009, 41, 1561-1566

8. Seyller. T., Bostwick. A., Emtsev. K. V., Horn. K., Ley. L., McChesney. J. L., Ohta. T., Riley. J. D., Rotenberg. E., Speck. F., Physica Status Solidi B-Basic Solid State Physics, 2008, 245, 1436-1446

9. Kertesz. M., Choi. C. H., and Yang. S., Chemical Review, 2005, 105, 3448-3481

10. Schleyer. P. V. R., Chemical review, 2005, 105, 3433-3435

11. Wu. J., Pisula. W., and Müllen K., Chemical Review, 2007, 107, 718-747

12. Fukushima. H., Ph.D. Dissertation, Michigan State University, East Lansing, MI, 2003.

13. Balandin. A. A., Ghosh. S., Bao. W. Z., Calizo. I., Teweldebrhan. D., Miao. F., Lau. C. N., Nano letters, 2008, 8, 902-907

14. Ghosh. S.,Nika. D. L.,Pokatilov. E. P., Balandin. A. A., New journal of physics, 2009, 11, 095012

15. Michael W. Rowell, Mark A. Topinka, Michael D. McGeheea, Hans-Jürgen Prall, Gilles Dennler, Niyazi Serdar Sariciftci, Liangbing Hu and George Gruner. Appl. Phys. Lett. 2006, 88, 233506-1-3

16. L. Schmidt-Mende, A. Fechtenkotter,K. Mullen, E. Moons, R. H. Friend, J. D. MacKenzie. Science 2001, 293, 1119-1122

17. Annica Andersson, Nicklas Johansson, Per Bröms, Nu Yu, Donald Lupo, and William R. Salaneck, Advanced Materials 1998, 10, 859-863

18. Schlatmann, A. R.; Floet, D. W.; Hilberer, A.; Garten, F.; Smulders, P. J. M.; Klapwijk, T. M.; Hadziioannou, G. Applied Physics Letter 1996, 69, 1764-1766

19. S. T. Lee, Z. Q Gao, L. S Hung, Applied Physics Letter 1999, 75, 1404–1406

20. Riichiro Saito, G. Dresselhaus "Physical Properties of Carbon Nanotubes", Imperial College Press, 1998

21. Alexander A. Green, Mark C. Hersam. Nanoletters 2008, 8, 1417-1422

22. Xuan Wang, Linjie Zhi, and Klaus Mullen. Nanoletters 2008, 8, 323-327

23. Héctor A. Becerril, Jie Mao, Zunfeng Liu, Randall M. Stoltenberg, Zhenan Bao, and Yongsheng Chen. ACS Nano 2008, 2, 463-470

24. Goki Eda, Giovanni Fanchini, Manish Chhowalla Nature Nanotechnology 2008, 3, 270 – 274

25. Dmitriy A. Dikin, Sasha Stankovich, Eric J. Zimney, Richard D. Piner, Geoffrey H. B. Dommett, Guennadi Evmenenko, SonBinh T. Nguyen & Rodney S. Ruoff Nature 2007, 448, 457-460

26. Supinda Watcharotone, Dmitriy A. Dikin, Sasha Stankovich, Richard Piner, Inhwa Jung, Geoffrey H. B. Dommett, Guennadi Evmenenko, Shang-En Wu, Shu-Fang Chen, Chuan-Pu Liu, SonBinh T. Nguyen, and Rodney S. Ruoff, Nanoletters 2007, 7 , 1888–1892

27. R. R. Nair, P. Blake, A. N. Grigorenko, K. S. Novoselov, T. J. Booth, T. Stauber, N. M. R. Peres, A. K. Geim. Science 2008, 320, 1308

28. Troy R. Hendricks, Jue Lu, Lawrence T. Drzal, and Ilsoon Lee. Advanced Materials, 2008, 20, 2008-2012

29. Simon. P., and Gogotsi. Y., Nature Materials, 2008, 7, 845-854

30. Pandolfo. A.G., Hollenkamp. A.F., Journal of power sources, 2006, 157, 11-27

31. Frackowiaka. E., Beguin. F., Carbon 2001, 39937-950

32. Lewandowski. A., Galinski. M., Journal of power sources, 2007, 173, 822-828

33. Winter. M., Brodd. R.J., Chemical review, 2004, 104, 4245-4270

34. Conway, B. E. "Electrochemical Supercapacitors: Scientific Fundamentals and Technological Applications" Publisher Kluwer, 1999.

35. C. Hiemenz, and Raj Rajagopalan, "Principles of colloid and surface chemistry", Publisher Science, 2000

36. Hiroyuki Ōhshima and Kunio Furusawa "Electrical phenomena at the interfaces: fundamentals, measurements and applications" Publisher Science, 1998

37. Obreja. V. V. N., Physica E, 2008, 40, 2596-2605

38. Chmiola. J., Yushin. G., Gogotsi. Y., Portet. C., Simon. P., Taberna. P. L., Science 2006, 313, 1760-1763

39. Lota. G., Centeno. T. A., Frackowiak. E., Stoeckli. F., Electrochimica Acta 2008, 53, 2210-2216

40. Talapatra. S., Kar. S., Pal. S. K., Vajtai. R., Ci. L., Victor. P.,Shaijumon. M. M., Kaur. S.,Nalamasu. O., and Ajayan. P. M., Natrure nanotechnology, 2006, 1, 112-116

41. Lua. W., Qub. L., Henrya. K., Dai. L., Journal of power sources, 2009, 189, 1270-1277

42. Futaba. D. N., Hata. K.,Yamada. T., Hiraoka. T., Hayamizu. Y., Kakudate. Y., Tanaike. O., Hatori. H., Yumura. M., and Iijima. S., Nature materials, 2006, 5, 987-994

43. Lee. S. W., Kim. B. S., Chen. S., Horn. Y. S., and Hammond. P. T., Journal of American Chemical Society, 2009, 131, 671-679

44. S. R. C., Rout. C. S., Subrahmanyam. K. S., Govindaraj. A., and Rao. C. N. R., Journal of chemical sciences, 2008, 120, 9-13

45. Stoller. M. D., Park. S. J., Zhu. Y. W., An. J. H., Ruoff, R. S., Nano letters, 2008, 8, 3498-3502

46. Lv. W., Tang. D. M., He. Y. B., You. C. H., Shi. Z. Q., Chen. X. C., Chen. C. M., Hou. P. X., Liu. C., Yang. Q. H., ACS Nano, 2009, 3, 3730-3736

47. Liang. M. H., Luo. B., Zhi. L.J., International Journal Of Energy Research, 2009, 33, 1161-1170

48. Zhao. X., Tian. H., Zhu. M. Y., Tian. K., Wang. J. J., Kang. F. Y., Outlaw. R. A., Journal of power sources, 2009, 194, 1208-1212

49. Wang. H. L., Hao. Q. L.,Yang. X. J., Lu. L. D., Wang. X., Electrochemistry communications, 2009, 11, 1158-1161

50. Wu. Q. F., He. K. X., Mi. H. Y., Zhang. X. G., Materials chemistry and physics, 2007, 101, 367-371

51. Zhou. C., Kumar. S., Chemistry of materials, 2005, 17, 1995-2002

52. An. K. H., Jeon. K. K., Jeong. K. H., Lim. S. C., Bae. D. J., Lee. Y. H., Journal of electrochemical society, 2002, 149, A1058-A106

53. Gupta. V., and Miuraa. N., Electrochemical and solid state letters, 2005, 8, A630-632

54. Najafabadi. A. I., Tan. D. T. H., Madden. J. D., Syntehtic metal, 2005, 152, 129-132

55. Sun, K., Stroscio, M. A., Dutta, M., Supperlattices and microstructure, 2009, 45, 60-64

56. Frank, I. W., Tanenbaum, D. M., van der Zande, A. M., McEuen, P.L., Journal of vacuum science Technology B, 2007, 25, 2558-2561

CHAPTER 2

A NOVEL APPROACH TO CREATE A HIGHLY ORDERED MONOLAYER FILM OF GRAPHENE NANOSHEETS AT THE LIQUID-LIQUID INTERFACE

Abstract: A monolayer of ultrathin sheets of highly hydrophobic graphene nanosheets was prepared on a large area substrate via self assembly at the liquid-liquid interface. Driven by the minimization of interfacial energy these planar shaped graphene nanosheets produce a closed packed monolayer structure at the liquid-liquid interface. This monolayer film shows high electrical conductivity of more than 1000 S/cm and an optical transmission of more than 70% at a wavelength of 550 nm. Interfacial self assembly of these nanosheets demonstrates a promising route for the application of this novel material in optoelectronics applications.

Significance of the research: Transparent, conductive and highly ordered monolayer of ultrathin hydrophobic graphene nanosheets were prepared on a large area substrate via self assembly at the liquid-liquid interface. Driven by the minimization of interfacial energy these planar shaped graphene nanosheets produce a closed packed monolayer structure at the liquid-liquid interface without agglomeration and restacking. This research has shown that the highly hydrophobic nature of the graphene nanosheet can be used to self assemble graphene nanosheets at the hydrophobic liquid - hydrophilic liquid interface into a close packed monolayer. Unlike the graphite oxide route, in this approach the native properties of graphene are preserved without requiring the chemical transformation of graphene to graphite oxide and back to graphene again. The use of large micron sized graphene nanosheets to comprise the film reduces the contact

resistance over the macroscopic area of the film. The resulting graphene nanosheet monolayer film is highly compact, optically transparent and highly electrically conductive.

Introduction: Transparent and electrically conductive glasses have a wide range of applications in solar cells, sensor devices, and electrostatic charge dissipating coatings [1-4]. The use of metal oxides like indium tin oxide (ITO) and fluorine tin oxide (FTO) are experiencing limited availability, susceptibility to ion diffusion in polymers and reduced transparency in the infra-red (IR) region [4-6]. Carbon nanotubes and graphite oxide nanosheets are possible alternatives to these metal oxides [7-11]. However, these graphite oxide nanosheets require extensive chemical treatment to produce and are electrically nonconductive due to the absence of a delocalized π-electron network on the basal plan [10-12]. The electrical performance of these nanomaterials depends strongly on the relative effectiveness of severe chemical and thermal reductive treatments [10-12]. However, attaining very high electrical conductivity is one of the prerequisite for high performance transparent films [8]. For graphene based systems, the presence of chemical defects as well as contact resistance over large macroscopic areas are key to the electrical property. While the chemical defects originate from oxidation and reduction of graphite basal plane, the contact resistance over large macroscopic areas depends on the size and the nature of overlaps between the particles within the film. The use of large sized graphene nanosheets with minimum chemical defects into a compact monolayer over large macroscopic area is therefore promising towards the application of this novel material as transparent conductor.

Exfoliated graphene nanosheets consisting of few layers of graphene, prepared from natural graphite through a simple intercalation and exfoliation process, contain the aromaticity of the graphite basal plane without extensive chemical treatments [13]. The average thickness of these nanosheets can be varied from 3 to 10 nm and the average size can be varied from submicron range to 100 μm [13]. These nanosheets exhibit low electrical resistivity of 50 x 10^{-6} Ωcm [13] and are also highly hydrophobic. Dispersion of these nanosheets in water results in immediate agglomeration even after sonication [14,15]. The use of surfactants in water shows limited improvement in dispersion quality of these large sized nanosheets [13]. Among the non polar solvents, chlorinated liquids like chloroform produce better dispersion. However, conventional drop coating coupled with spin coating or dip coating from chlorinated dispersions results in an irregular structure of agglomerated nanosheets after solvent evaporation.

Directed self assembly of nano or micro sized particles at the liquid-liquid interface is a potentially alternative approach to fabricate a particle monolayer in regular two dimensional array in a controllable manner [16-20]. Self assembly of micrometer sized colloidal particles has been demonstrated at the liquid-liquid interface [27]. A reduction in interfacial energy between the oil and water phase drives the particles to assemble at the interface. Size dependent self assembly of hydrophobic CdSe nanoparticles at the liquid-liquid interface was earlier demonstrated by Lin and co workers [16]. In comparison to microscopic particles, the influence of thermal energy on the stability of nanoparticles at the liquid-liquid interface is considerable. A balance between thermal fluctuation and interfacial free energy controls the size and shape selective adsorption of nanoparticles at the liquid-liquid interface [16,17,18]. At the interface, the difference in

wettability of the particle by the two liquid phases can cause the interface to curve around the particle to form a meniscus [22]. The overlap of menisci around each particle generates an attractive lateral capillary force, leading to the formation of a highly ordered particle monolayer at the liquid-liquid interface [18,22,29]. This research reports on an investigation of the stability and energetically favorable formation of close packed monolayer of highly hydrophobic graphene nanosheets at a liquid-liquid interface and the potential to utilize this approach to produce transparent and electrically conductive monolayer.

Result and discussion: Graphene nanosheets were first sonicated in chloroform at a concentration of 0.1mg/ml. The dispersion was centrifuged for 10 minutes at 5000 rpm to separate the thinner nanosheets from the semi transparent supernatant liquid at the top. Figure 2.1a,b shows the FESEM image of a typical graphene nanosheet deposited on a cellulose acetate filter membrane from the centrifugally separated chloroform dispersion. The average size of the nanosheet is estimated to be 8 to 10 micron. The average thickness of the starting graphene nanosheets was previously estimated to be less than 10 nm [24]. However, after the separation of the thinner nanosheets by centrifuging, AFM was used to measure the thickness of individual nanosheets. Figure 2.1c shows that the average nanosheet thickness is 3 to 4 nm. However, it should be noted that nanosheets are not completely lying flat on the substrate and thus there is some variation in the height.

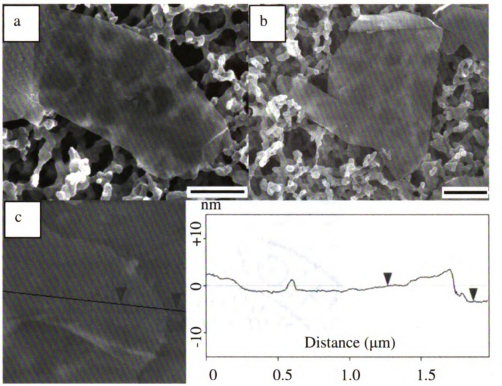

Figure 2.1: **FESEM morphological characterization** (a,b) FESEM image of graphene nanosheet deposited on cellulose acetate filter membrane. The average size of the nanosheet is estimated to be 8 to 10 μm. The scale bar is 2 μm. (c,d) In the tapping mode AFM image the average thickness of flat nanosheet is 4nm.

Figure 2.2 illustrates various steps to produce the two dimensional arrays of graphene nanosheets at the liquid-liquid interface. First nanosheets are dispersed in chloroform and after water is added to the mixture, two distinct phases formed containing graphene nanosheets dispersed in the chloroform phase. However, to transport the nanosheets completely from the bulk phase to the liquid-liquid interface requires an input of mechanical work through sonication for a brief period of time. The external mechanical

force breaks the two immiscible liquid phases into numerous drops and bubbles creating a large interfacial area between the two liquids. Driven by the minimization of interfacial free energy, the graphene nanosheets are preferentially adsorbed at the chloroform-water interface.

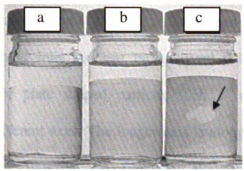

Figure 2.2: **Adsorption of graphene nanosheets at the liquid interface**: 2a represents distinct phases of two pure liquids, chloroform and water in contact with each other. In 2b graphene nanosheets are dispersed in the chloroform phase and water was added on the top to get two distinct phases with graphene nanosheets dispersed in the chloroform phase. This two-phase mixture was then briefly sonicated to adsorb the nanosheets at the liquid-liquid interface. Figure 2.2c clearly shows the film of graphene nanosheets covering the liquid-liquid interface and then extends up the chloroform glass interface. On the marked area of figure 2.2c a part of the film has been cracked with a spatula to show the liquid inside.

However, interfacial adsorption of particles at the interface reduces the entropy by the Boltzmann factor. Therefore the gain in the interfacial energy is responsible for the stability of the particles at the interface [16-18,21,22]. The three interfacial energies at the particle-oil interface γ_{po}, particle-water interface γ_{pw} and oil-water interface γ_{ow} are

related to each other through the three phase contact angle by the Young's equation as [23],

$$Cos\theta = (\gamma_{po} - \gamma_{pw}) / \gamma_{ow}$$

Apart from the three interfacial energies, the role of particle size and shape are paramount to the gain in the total interfacial energy of the system. Following an analysis, developed by Binks, the energy of attachment of the disk or flat shaped particle over various contact angles at the liquid-liquid interface can be analyzed [21]. In contrast to spherical nanoparticles, a disk or plate shaped particle, such as this graphene nanosheet is characterized by two different axes. The longer axis is along the width of the nanosheet and the aspect ratio 'a/b' is thus the ratio of two axes along the width and thickness of the nanosheets. With the thickness and average width of the nanosheets taken as 4 nm and 10 micron respectively, the aspect ratio a/b is 2500. Assuming that particles are attached to a planar oil water interface, the free energy of detachment of a planar nanosheet into the water and the chloroform phase is given as,

$$\Delta G_{dw} = \gamma_{ow}\pi b^2(1-\cos\theta)^2[1+(a/b-1)^2/(1-\cos\theta)+2(a/b-1)(\sin\theta-\theta\cos\theta)/(1-\cos\theta)^2] \quad \text{.....(i)}$$

$$\Delta G_{chl} = \Delta G_{dw} + 2\pi\gamma_{ow}b^2\cos\theta[(a/b-1)^2+\pi(a/b-1)+2] \quad \text{.....(ii)}$$

Where, ΔG_{dw} and ΔG_{chl} are the free energies of detachment of the particle from the interface into the water and the chloroform phase respectively. 'γ_{ow}' is the interfacial energy at the chloroform water interface. Equation (i) describes the free energy of detachment of the particle into the water phase at contact angle between 0 to 90^o and Equation (ii) corresponds to the free energy of detachment of the particle into the

chloroform phase at contact angle between 90^{o} to 180^{o}. The free energy of particle detachment as compared to the thermal energy at various contact angle θ is shown in Figure 2.3.

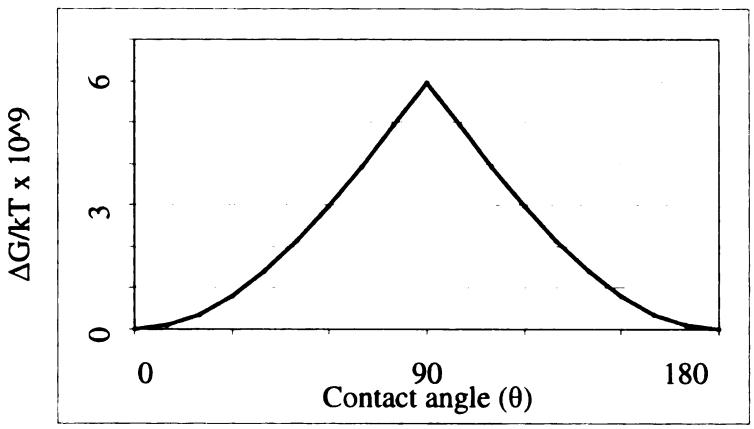

Figure 2.3: **Free energy of particle detachment** – The above figure shows the variation in free energy of detachment of particle as a function of contact angle (θ). The particle thickness and width are 4 nm and 10 micron respectively.

At equilibrium, free energy of attachment of the particle to the liquid-liquid interface is $\Delta G_a = - \Delta G_d$ With the measured three phase contact angle between water and chloroform on the graphene nanosheet close to 94^{o}, the above calculation predicts that the particle attachment at the liquid-liquid interface is energetically highly favorable. Therefore, the larger and thinner the nanosheet, the higher would be the aspect ratio and it is more

favorable for the nanosheets to get adsorbed at the interface with substantial gain in the interfacial energy.

In natural graphite, the layers of graphene are strongly attached to each other by van der Waals force of attraction. The cohesive energy was determined to be 5.8 kJ/mol with each layer separated by a distance of 3.36 A^{o} [24,25,26]. After intercalation and exfoliation these layers are separated from each other. However, the attractive interaction energy between the graphene nanosheets is strong. In this study, the thinner nanosheets of graphene, separated by centrifugation in chloroform, is stable for days without any visible settling keeping the individual nanosheets separated from each other. Introduction of the water phase and subsequent sonication produces a large interfacial area between these two immiscible liquids. At this point, the nanosheets gain interfacial free energy by adsorption at the liquid-liquid interface rather than re-stacking and settling out of the suspension. Thus with increasing concentration, nanosheets are expected to concentrate at the liquid-liquid interface. Experimentally it was found that with increasing nanosheet concentration the extent of the interfacial adsorption area covered with the nanosheets increased. The graphene nanosheet film extended downwards towards the edge of the chloroform phase with a thin layer of water outside (Figure 2.3c). However, at higher concentration, thick layers of nanosheets were found near the interface resulting in agglomeration and coalescence. Thus, while the gain in interfacial energy drives nanosheets to form a monolayer at the liquid-liquid interface, the concentration of the nanosheets must be controlled to prevent nanosheet agglomeration and coalescence.

The thin graphene nanosheet film formed at this liquid-liquid interface was transferred onto a glass substrate and the morphology and orientation of the graphene nanosheets were characterized by the high resolution FESEM imaging. Representative images taken from different sections of the film are shown in Figure 2.4.

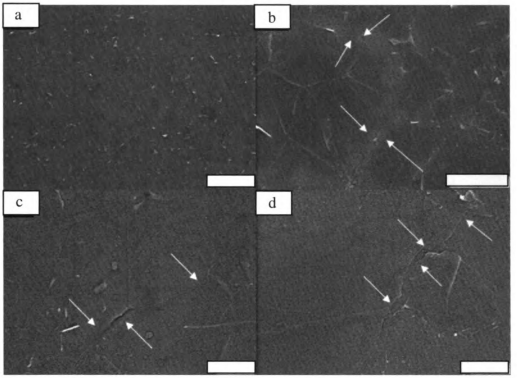

Figure 2.4: **Monolayer film of graphene nanosheets** – (a-d) FESEM micrographs of graphene nanosheets deposited on the glass slide. The specimen was sputter coated with gold to get better contrast on the image. Images, taken from different areas, clearly exhibit how the planar nanosheets are interconnected with each other. Without coming on top of each other, nanosheets are well interconnected, forming a monolayer over the large area of the substrate. The arrows, shown in the images, indicate the edge of nanosheets. Scale bar 50, 2, 1, 1 μm respectively

From the FESEM characterization, it is evident that the graphene nanosheets form a close packed array with remarkable uniformity over a macroscopic sized area. The graphene nanosheets are well dispersed and interconnected at the edges with little detectable gaps. Furthermore, there was very little overlapping of the graphene nanosheets observed.

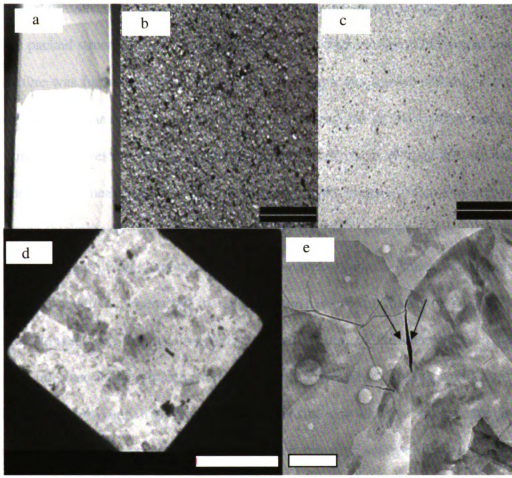

Figure 2.5: **TEM and optical microscopy characterization:** shows the metallic luster of graphene nanosheet film under white light. The film is deposited on microscopic glass slide. Figure 2.5b,c represents optical microscopy images of film prepared from two different nanosheet thicknesses. Numerous dark spots in Figure 2.5b give clear evidence of the presence of thicker nanosheets of average thickness of 10 nm. Under similar condition, film prepared from thinner nanosheets of an average thickness of 3 to 4 nm shows much higher transparency as shown in figure c. The scale bar is 500 μm (figure c). High magnification TEM micrograph in figure 2.5e explains the morphology of the film with individual nanosheets touching each other at the edges without any complete overlap. The arrows on the image 5e indicate how two individual nanosheets are interconnected through the edges.

The metallic luster of the graphene nanosheet film, as shown in figure 2.5a, indicates a close packed structure over large macroscopic area. The formation of compact monolayer structure was further evident from the optical microscopy image of films prepared from two different nanosheet thicknesses. The darker regions in the optical micrograph of Figure 2.5b represent film prepared from nanosheets with an average thickness of 10 nm. Under similar measurement condition, however, films prepared from nanosheets with an average thickness of 3 to 4 nm shows high transparency over large macroscopic area as shown in Figure 2.5c. A complete overlap between thinner nanosheets in Figure 2.5c, however, would have resulted in reduced transparency as shown in Figure 2.5b. This result substantiates the fact that individual adsorption of the nanosheets at the liquid-liquid interface is energetically more favorable than restacking and agglomerating with each other. Low and high magnification transmission electron microscopy images in Figure 2.5d,e also reveals compact monolayer structure with two individual nanosheets touching each others at the edges as shown in Figure 2.5e.

Thus the above investigations from FESEM, TEM and optical microscopy suggests that once the minimization of interfacial energy drives the nanosheets from the bulk phase to the liquid-liquid interface, they self assemble as a result of force of interaction between them to create a large area close packed monolayer structure.

These graphene nanosheets are highly hydrophobic. However, a very small amount of oxygen functional groups always covers the edge of the nanosheet [13]. Therefore, it is expected that the presence of both hydrophobic and hydrophilic faces at the edge of the nanosheet can perturb the interface large enough to generate a menisci around the particle

[28,29]. Attractive lateral capillary force generates from the overlap of such 'like' menisci around the particle to form a close packed structure at the liquid-liquid interface. Directed self assembly through the formation of "capillary bond" for particles with both hydrophilic and hydrophobic faces was demonstrated earlier [29,30,31]. While the magnitude of this lateral capillary force is negligible for spherical particles with diameter less than 10 μm [30], previous work from Bowden et al. showed that, for planar shaped particles at the liquid-liquid interface, the lateral capillary force is quite significant even for particles with thicknesses of few nanometers [18]. They analyzed the lateral capillary force as the two bodies approach each other from infinite distance. As the two bodies approach each other, the height of the meniscus is related to the change in the arc length. The interfacial energy is then obtained by multiplying the change in arc length, the interfacial tension between two liquids and the aspect ratio of the nanosheet. Following this same approach, calculation of the interfacial free energy shows that the capillary force driven two dimensional self assembly of graphene nanosheets is energetically favorable with a ΔG of more than -10 k_BT at nanosheet thickness of 4 nm with an aspect ratio of 2500. As a result this capillary force drives the graphene nanosheets to each other maximizing their hydrophobic surface area and creating a close packed monolayer at the liquid-liquid interface in exact agreement with our observation and measurement.

Graphene nanosheet film transparency was measured at various film thicknesses. The thickness of the nanosheet depends on the surface area of the parent exfoliated graphene nanosheet. We separated thin sheets of graphene from exfoliated graphene nanosheet with different surface areas. With low surface area materials, the transparency of the film is as low as 10%. With increasing surface area, the thickness of the nanosheet decreases

and the transparency of the corresponding film increases. Figure 2.6 represents the optical transmission profile of graphene film obtained from different thickness nanosheets.

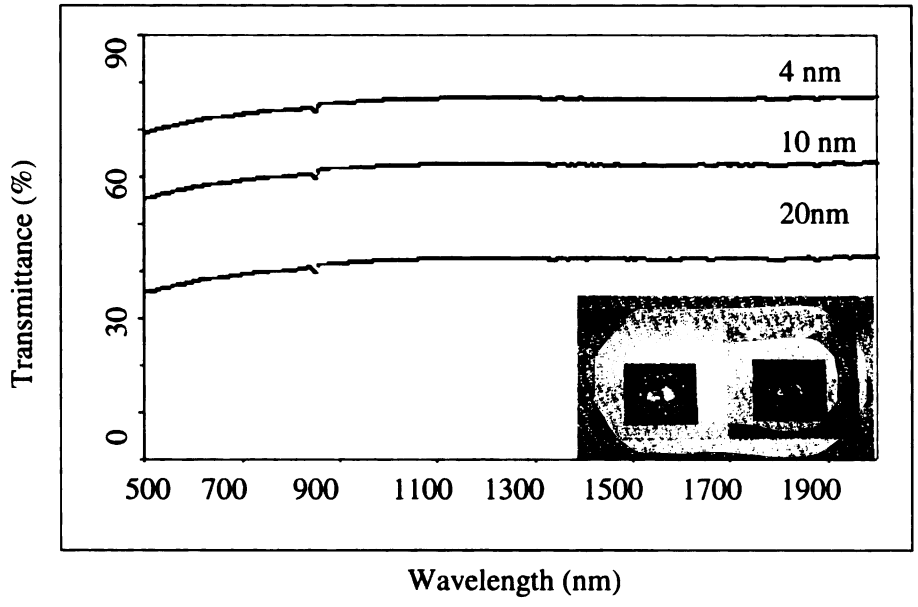

Figure 2.6: **Optical transmission spectra**: Optical transmission spectra from 500 nm to 2000 nm of monolayer film of graphene nanosheets at various nanosheet thicknesses. Inset, the photograph illustrates the clarity and transparency of a 4 nm thickness graphene nanosheet film. The scale bar is 1 inch.

At a wavelength of 500 nm the transmission of graphene nanosheet film having an average thickness of 4 nm is about 70%. The transmission increases to slightly less than 80% at increasing wavelength. In a recent publication by Hersam et al., a similar transparency at 500 nm wavelength was achieved by using high purity metallic carbon nanotubes [8]. The transmission characteristics are very flat in the visible and near infra red region of the electromagnetic spectrum to 2000 nm in contrast to the ITO and FTO

coated glass. This result is consistent with previously published reports on reduced graphite oxide films [10,11,12]. Such an optical transmission profile makes these types of graphene films highly desirable for optoelectronics applications.

The electrical conductivity of the graphene nanosheet film was measured by using the 4 point probe method at 10 different locations on the film. The average sheet resistance of the graphite nanosheet film of 4 nm thickness is 10^2 Ω/sq order of magnitude and the average conductivity is more than 1000 S/cm. The highest electrical conductivity was near 1250 S/cm. This high value of electrical conductivity is comparable with FTO coated glass slides as well as transparent carbon nanotube electrodes [4,7-9]. However, compared to the conventional metal oxides like ITO or FTO, this monolayer film is very thermally stable. After heating a graphene nanosheet specimen at 350^{o} C for more than 3 hours in an ambient atmosphere, the conductivity of the film did not change. In contrast to published report on the graphene nanosheet films made from reduced graphite oxide [10,11,12], the electrical conductivity of this graphene nanosheet film is independent of the film thickness. The average film conductivity is always more than 1000 S/cm regardless of film thicknesses. This observation is consistent with the fact that these nanosheets form a closed packed monolayer at the liquid-liquid interface. This close packed structure ensures high electrical conductivity irrespective of the thickness of the nanosheet.

Conclusion: Previous research [10,11,12] has produced ultrathin layers of graphene using the graphite oxide route allowing water based processing but requiring the use of hazardous chemicals to produce graphite oxide and to reduce it back to graphene. This research has shown that the highly hydrophobic nature of the graphene nanosheet can be

used to self assemble thin graphene nanosheet at the hydrophobic liquid - hydrophilic liquid interface into a close packed monolayer. As a result the native properties of graphene are preserved without requiring chemical transformation of the basal plane. The resulting graphene nanosheet monolayer film is highly compact, optically transparent from the visible to the infra red region and electrically conductive. The large microscopic size of the graphene nanosheets that comprise the film reduces the contact resistance over the macroscopic area of the film. The graphene nanosheets are inexpensive to produce and the process to form a monolayer is easily scalable to very large areas offering a new material and method to replace ITO and FTO coatings for optoelectronics applications.

References:

1. Gan, Y.; Liu, J. X.; Zeng, S. N. Surface Coating Technology 2006, 201, 25-29

2. Rowell, M. W.; Topinka, M. A.; McGehee, M. D.; Prall, H. J.; Dennler, G.; Sariciftci, N. S.; Hu, L.; Gruner, G. Applied Physics Letter 2006, 88, 233506-1-3

3. Mende, L. S.; Fechtenko¨tter, A.; Mu¨llen, K.; Moons, E.; Friend, R. H.; MacKenzie, J. D. Science 2001, 293, 1119.

4. Andersson, A.; Johansson, N.; Bro¨ms, P.; Yu, N.; Lupo, D.; Salaneck, W. R. Advanced Materials, 1998, 10, 859

5. Schlatmann, A. R.; Floet, D. W.; Hilberer, A.; Garten, F.; Smulders, P. J. M.; Klapwijk, T. M.; Hadziioannou, G. Applied Physics Letter, 1996, 69, 1764

6. Lee, S. T.; Gao, Z. Q.; Hung, L. S. Applied Physics Letter, 1999, 75, 1404–1406.

7. Zhuangchun Wu; Zhihong Chen; Xu Du; Jonathan M. Logan; Jennifer Sippel; Maria Nikolou; Katalin Kamaras; John R. Reynolds; David B. Tanner; Arthur F. Hebard; Andrew G. Rinzle. Science 2004, 305, 1273-1276.

8. Alexander A. Green and Mark C. Hersam. Nanoletters 2008, 8, 1417-1422.

9. Bong Sup Shim; Zhiyong Tang, Matthew; P. Morabito; Ashish Agarwal; Haiping Hong; Nicholas A. Kotov. Chemistry of Materials 2007, 19, 5467-5474

10. Xuan Wang; Linjie Zhi; and Klaus Mullen. Nanoletters 2008, 8, 323-327

11. Héctor A. Becerril; Jie Mao; Zunfeng Liu; Randall M. Stoltenberg; Zhenan Bao; and Yongsheng Chen; ACS Nano 2008, 2, 463-470

12. Goki Eda; Giovanni Fanchini; Manish Chhowalla. Nature Nanotechnology 2008, 3, 270 – 274

13. Fukushima H. Graphite "Nanoreinforcements in Polymer Nanocomposites" PhD Dissertation, Michigan State University, East Lansing, MI, 2003

14. Troy R. Hendricks; Jue Lu; Lawrence T. Drzal; and Ilsoon Lee. Advanced Materials, 2008, 9999, 1-5

15. Lu, J.; Drzal, L.T.; Worden, R.M.; Lee, I. Chemistry Materials, 2007, 19, 6240–6246

16. Y. Lin; H. Skaff; T. Emrick; A. D. Dinsmore; T. P. Russell. Science 2003, 299, 226-229

17. Wolfgang H. Binder; Angewandte Chemie International Eddition 2005, 44, 5172 – 5175

18. Ned Bowden; Andreas Terfort; Jeff Carbeck; George M. Whitesides. Science 1997, 276, 233-235.

19. Hongwei Duan; Dayang Wang; Dirk G. Kurth; Helmuth Mohwald. Angewandte Chemie International Eddition, 2004, 43, 5639 –5642

20. Dayang Wang; Hongwei Duan; Helmuth Mohwald; Soft Matter, 2005, 1, 412–416

21. Benard P. Binks, "Colloidal particle at liquid interfaces", 2006 Cambridge University press.

22. Peter A. Kralchevsky, Kuniaki Nagayama "Particle at fluid interfaces and membranes" 2001 Elsevier.

23. Robert J. Stokes; D. Fennell Evans. "Fundamentals of Interfacial Engineering", 1996 Wiley-VCH

24 Adam H. R. Palser. Phys. Chemistry Chemical Physics, 1999, 1, 4459-4464

25 L.A Girifalco; R.A Lad. Journal chemical physics, 1956, 25, 693-697

26. Dan Li; Marc B. Müller; Scott Gilje; Richard B. Kaner; Gordon G. Wallace; Nature Nanotechnology 2008, 3, 101 – 105

27. Nikolina D. Vassileva; Dirk van den Ende; Frieder Mugele; Jorrit Mellema. Langmuir 2005, 21, 11190-11200

28. Ned Bowden; Andreas Terfort; Jeff Carbeck; George M. Whitesides; Science 1997, 276, 233

29. Ned Bowden; Scott R. J. Oliver; George M. Whitesides. J. Physical Chemistry B 2000, 104, 2714-2724

30. P. A. Kralchevsky; V. N. Paunov; N. D. Denkov; I. B. Ivanov; K. Nagayama, J. Colloid Interface Sci. 1993, 155, 420

CHAPTER 3

MULTILAYERED NANO-ARCHITECTURE OF VARIABLE SIZED GRAPHENE NANOSHEETS FOR ENHANCED SUPERCAPACITOR ELECTRODE PERFORMANCE

Abstract: The diverse physical and chemical aspects of graphene nanosheets such as particle size surface area and edge chemistry were combined to fabricate a new supercapacitor electrode architecture consisting of a highly aligned network of large sized nanosheets as a series of current collectors within a multilayer configuration of bulk electrode. Capillary driven self assembly of monolayers of graphene nanosheets was employed to create a flexible, multilayer, free standing film of highly hydrophobic nanosheets over large macroscopic areas. This nano-architecture exhibits a high frequency capacitative response and a nearly rectangular cyclic voltammogram at 1000 mV/sec scanning rate, possesses a rapid current response, small equivalent series resistance (ESR) and fast ionic diffusion for high power electrical double layer capacitor (EDLC) application.

Significance of the research: The diverse physical and chemical aspects of graphene nanosheets such as particle size surface area and edge chemistry were combined to fabricate a new supercapacitor electrode consisting of a highly aligned network of large sized nanosheets as a series of current collectors within a multilayer configuration of bulk electrode. Graphene nanosheets, used in this research, are prepared by direct exfoliation as opposed to the graphene oxide route without altering the attractive, native chemical properties of graphene basal planes. Self assembly of these highly hydrophobic graphene nanosheets driven by the minimization of interfacial energy at the liquid-liquid interface

has a distinctive advantage for the fabrication of a highly dispersed monolayer network over large macroscopic areas. Retention of the strong aromatic character of the graphene nanosheets prepared in this way causes a large inter planar interaction from the capillary force and drying induced collapse of monolayers of graphene nanosheets into a flexible and 100% binder free multilayer, free standing film. Previous research employed a vacuum filtration approach from the water based dispersion of graphite oxide or reduced graphite oxide to produce well packed and highly aligned graphene paper of various thicknesses. A major benefit in our approach is that nanomaterials of a desired architecture along with graphene's attractive physical and chemical characteristics can be synthesized into an architecture consisting of large and small graphene nanosheets into a highly dispersed and aligned network in a bulk macroscopic configuration designed to maximize device performance. Monolayers of large sized nanosheets function as a series of highly electrically conducting current collectors within the mesoporous network of small sized graphene nanosheets for improved rate capability of EDLC electrode. This nano-architecture exhibits a high frequency capacitative response and a nearly rectangular cyclic voltammogram at 1000 mV/sec scanning rate, possesses a rapid current response, small equivalent series resistance (ESR) and fast ionic diffusion for high power electrical double layer capacitor (EDLC) application. These inexpensive graphene nanosheets and the ease of the process to produce the aligned nanostructure make this new material and method highly advantageous for high power supercapacitor applications.

Introduction: Graphene, a two dimensional aromatic macromolecule, is the basic building block for different allotropes of carbon such as carbon nanotubes (CNT), fullerene and graphite [1-4]. Exceptional electrical, thermal, and mechanical properties along with facile manufacturing techniques make this inexpensive, two dimensional monolayer allotrope of carbon unique from other graphitic dimensionalities [1-4]. Acid intercalation followed by thermal exfoliation of natural graphite is an easy approach to produce exfoliated graphene nanosheets with a surface area about 270 m^2/g and an average thickness from 3 to 5 nm with a lateral dimension ranging from sub micron to more than 50 μm [5]. These nanosheets with stacks of few single layer graphene preserve the aromaticity without requiring any extensive chemical oxidation treatment of the graphene basal plane to exhibit low electrical resistivity of 50 X 10^{-6} ohm.cm [5]. Retention of aromaticity of graphene and the absence of significant oxygen functionalities on the graphene basal plane result in high thermal stability (2% wt loss in air) of these nanosheets in the temperature range from 120 to 350 C, where a considerable weight loss is expected for highly oxidized graphene basal plane from the generation of decomposed gaseous products such as CO and CO_2 [6,7,8] (Supporting information Figure 3.S1). XPS elemental analysis further confirms the high degree of aromaticity with a C/O atomic ratio close to 25.7. (Supporting information Figure 3.S2) However, the high degree of hydrophobicity, resulting from the aromaticity, prohibits the dispersion of these nanosheets in water and other polar liquids and results in agglomeration even after extended sonication [9,10] The key to the success of exploiting the unique properties of graphene nanosheets lies in the homogeneous and orderly distribution of

these nanosheets from the nanoscale to the macroscale regime. The primary challenge is to overcome the self-aggregation following the strong van der Waals force of attraction between the large and planar basal planes. Liquid-liquid interfacial adsorption is one approach to overcome this self aggregation to create a monolayer film of these hydrophobic nanosheets from the minimization of interfacial energy at the hydrophobic liquid-hydrophilic liquid interface [10].

An aligned network of these highly electrically conductive graphene nanosheets is expected to demonstrate reduced electronic resistance and rapid charge discharge characteristics for electrochemical energy storage applications. Capillary force driven self assembly of vertically aligned carbon nanotubes into a highly dense and compact structure for electrochemical energy storage application such as electrical double layer capacitors (EDLC) has been well documented in different publications [11,12,13]. However, the construction of an aligned network of CNT from a previously grown bulk carbon nanotube forest on a large macroscopic area often results in formation of microcracks or open cellular structure during the collapse and shrinkage of the CNTs by the capillary force and drying induced condensation [14,15]. This kind of microcrack formation is universal during the drying induced shrinkage of bulk materials such as mud, clay, and others. Instead of using bulk material in an analogous capillary force driven self assembly process we introduce a "bottom-up" approach, starting with a monolayer film of graphene nanosheets to create a highly aligned multilayer, free standing film over large macroscopic areas. The capacitative response of this aligned multilayer configuration is explored for rapid charge discharge characteristics in high power EDLC applications. Then the impact of physical and chemical aspects of the

graphene nanosheets such as particle size, alignment, and surface chemistry is investigated on optimizing the performance of graphene nanosheets based electrodes for EDLC applications.

Result and discussion: In the liquid-liquid interfacial adsorption technique, nanosheets of average lateral dimension of 15 μm and thickness of 3 to 5 nm were first dispersed in chloroform followed by the addition of a small amount of water to create a two phase mixture [10]. This two phase mixture was then briefly sonicated to create a large interfacial area between the two immiscible liquids. At this point, the transport of graphene nanosheet from the bulk phase towards the liquid-liquid interface was driven by the minimization of interfacial energy [10]. The interfacial self assembly approach had the advantage to create a highly dispersed monolayer network of hydrophobic nanosheets over a large macroscopic area without requiring any chemical transformation of the graphene basal plane [10]. With the retention of this strong aromatic character, layers of these highly dispersed networks of graphene nanosheets were expected to interact strongly with each other in a face-to-face union of large basal planes. van der Waals force induced stacking of these nanosheets is the key to our approach to create a highly aligned, multilayer structure from successive depositions of close packed monolayer films one on top of another.

In creating a multilayer structure, first a monolayer film of graphene nanosheets was transferred on a solid substrate such as a microscopic glass slide (Figure 3.1a). The film was then annealed at 100 C to completely drive off the liquid. When a second layer of monolayer film was transferred on top of the first one, a thin film of water always

separates these nanosheets preventing close contact with each other. With continuous evaporation of water, the interlayer separation decreases and the strong capillary force causes the nanosheets spacing to decrease and the layers to collapse on each other. On complete liquid evaporation, strong van der Waals force of attraction adheres these planar nanosheets into a stable bilayer structure. The bilayer film was annealed again at 100 C (Figure 3.1a middle slide).

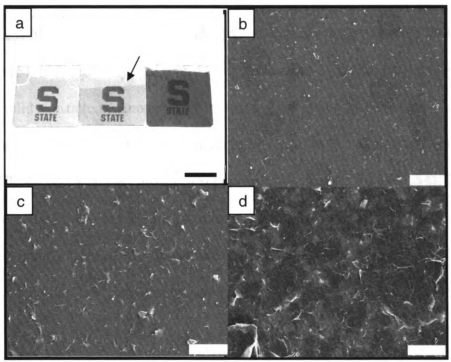

Figure 3.1: **A multilayer structure of graphene nanosheets from successive depositions of monolayer films one on top of another:** a) A stable monolayer, bilayer, and multilayer (four layers) films were deposited on glass substrate and are shown in figure 3.1a (Scale bar 1 cm). Under the marked arrow in the middle slide, two monolayer films were deposited one top of another to create a stable bilayer structure. The optical transparency also decreases linearly with increasing number of depositing layers. b,c,d) From the FESEM morphological characterization beginning with figure 3.1b, a substantial overlap between nanosheets was observed from the monolayer to multilayer configuration in figure 3.1d. (Scale bar 50, 20, 10 μm respectively)

As compared to spherical points or parallel chain molecules, the van der Waals interaction free energy between two parallel planes is much higher and it scales with the separation distance (d) as $(1/d^2)$ [16,17]. Thus when two monolayer films of planar nanosheets are placed one on top of another, a large van der Waals force of attraction causes them to adhere with each other and form a stable bilayer and multilayer structure. It is also possible that the π-electron interaction between the large basal planes also contributes to this interaction [16,17]

This process of capillary and drying induced self assembly of successive monolayers is continued to build a multilayer film of desired thicknesses. The film can then be detached from the solid substrate by immersing it in water which slowly wets the glass surface and causes the displacement of this highly hydrophobic film from the glass surface to a state where it floats on the water surface. (Supporting information Figure 3.S4) The film is then dried at 100 C to obtain a free standing, multilayer film of graphene nanosheets as shown in Figure 3.2. FESEM micrographs clearly show that the film is flexible without any cracks over the large macroscopic area.

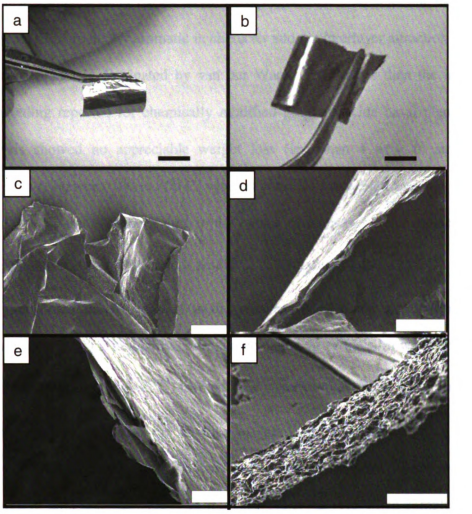

Figure 3.2: Characterization of the morphology of the multilayer, free standing film: a,b) the film is flexible and can be bent or rolled (Scale bar 1 cm) c) FESEM micrograph clearly shows a crumpled film without the formation of large fragments or cracks.(scale bar 500 um) d,e,f) films of various thicknesses from less than 5 um to more than 50 μm (Scale bar 20, 5 and 200 μm respectively).

As shown in Figure 3.2d-f, films of various thicknesses can be prepared by controlling the number of deposited layers. This process results in the formation of a 100% binder free multilayer, free standing film of graphene nanosheets uniformly dispersed and are

strongly attached to each other over a large macroscopic area. The graphene nanosheets comprising this film are highly aromatic in character and the interlayer attraction between the large basal planes is dominated by van der Waals force rather than the interlayer hydrogen bonding reported for chemically modified graphite oxide basal planes [6,7]. TGA analysis showed no appreciable weight loss (less than 4 wt% in air) in the temperature range between 100 to 350 C, where a considerable weight loss was reported for graphite oxide based systems owing to the release of interlayer water molecules and the decomposition of the surface oxides resulting in a mixture of CO and CO_2 from the various oxygen functionalities present on the graphene basal plane [6,7,8] (Supporting information Figure 3.S1). The highly hydrophobic character of the film was also evident from the large contact angle (~96.7^{O}) formed by a water droplet on the film (Supporting information Figure 3.S5). With the absence of interlayer hydrogen bonding and the presence of turbostratic stacking of graphene nanosheets in different layers, the film is strong enough to hold together over large macroscopic areas even when completely bent and rolled in a cylindrical shape (Supporting information Figure 3.S6). The Raman spectra, measured on the multilayer film, exhibits a sharp G band peak at 1575 cm^{-1} and a minor D band peak at 1344 cm^{-1} (Supporting information Figure 3.S7). The aromatic purity of the film is also evident from this low I (D) / I (G) ratio, which is a direct measure of the degree of defects, disorder and structural incoherence of crystalline graphitic domain of the large basal plane on graphene nanosheets [18,19,20]. As a result the 'as-prepared' multilayer film exhibits very high electrical conductivity of the order of

1.24 X 10^4 S/m, measured by using a four point probe set up on an average of four samples.

Self assembly of these successive monolayers can also be accomplished on metal substrates such as stainless steel substrate to create a multilayer configuration of graphene nanosheets as a 100% binder-free electrode for EDLC application (Supporting information Figure 3.S8). For this purpose, thin film electrodes with an average thickness of 20 μm were assembled in a two-electrode configuration and the assembly was immersed in aqueous 6M KOH solution for electrochemical measurement. In EDLC applications, a highly oblique and narrow shaped capacitance-voltage response at high scanning rate is highly undesirable [21]. This shape results from large internal and interfacial contact resistance of the active material inside the bulk electrode [21]. From Figure 3.3a, a nearly rectangular and highly symmetric cyclic voltammogram (CV) curve at an increasing voltage scanning rate from 250 to 1000 mV/sec clearly demonstrates rapid current response, small equivalent series resistance (ESR) and fast ionic diffusion within the aligned network of graphene nanosheets for this multilayer film electrode. Retention of aromaticity of graphene basal plane and the strong overlap between these large sized nanosheets from different layers create a highly conducting network with minimum internal resistance over the macroscopic area of the film. In comparison to other allotropes of carbon, these two dimensional nanosheets lay flat on the solid substrate to generate a large contact area between the active electrode material and the current collector surface.

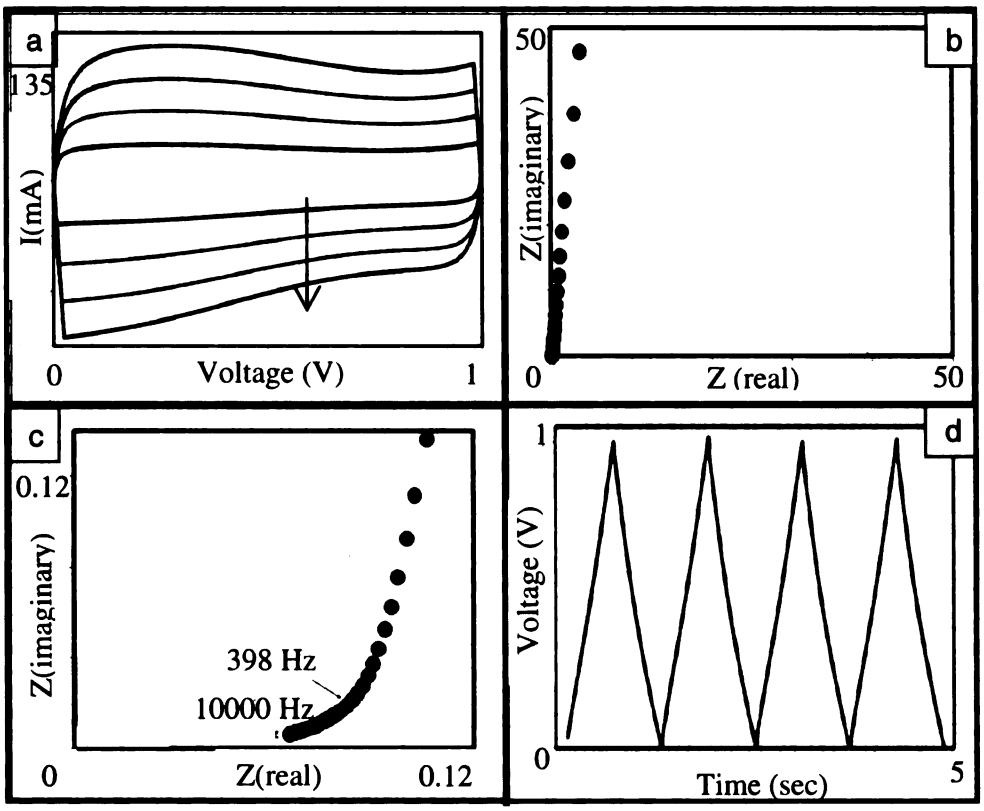

Figure 3.3: **Electrochemical characteristics of multilayer graphene nanosheet film**: a) The retention of nearly rectangular CV at high scanning rates from 250 mV/sec, 500 mV/sec, 750 mV/sec to 1,000 mV/sec b) Complex plane impedance analysis from high to low frequency c) Impedance analysis at high frequency region with the knee frequency appearing close to 398 Hz d) highly symmetric charge discharge characteristics at current density 30 A/g

The impact of low internal resistance and minimum interfacial contact resistance with the current collector was evident from the high frequency capacitative response of the electrode with a knee frequency close to 398 Hz, as shown in Figure 3.3b-c. The appearance of high knee frequency was only comparable to the performance of highly

aligned carbon nanotube network directly grown on the current collector surface [22,23,24]. From the Bode plot, a phase angle close to 90^{o} up to a frequency 10 Hz clearly suggests the device functionality close to an ideal capacitor (Supporting information Figure 3.S9). The average specific capacitance, measured from the discharge slope (shown in Figure 3.3d) at constant current density 30 A/g was close to 36 F/g, which is comparable to the capacitance obtained with highly aligned carbon nanotube electrodes [22,23,24]

In order to investigate the role of edge functionalities and the impact of particle dimension of graphene nanosheets on the capacitative response and the bulk resistivity of the electrode, small sized nanosheets with an average dimension of 500 nm were prepared by mechanical milling of large sized nanosheets without applying any oxidative chemical cleavage of large basal planes [5]. The increase in the surface area of the small sized nanosheets to 550 m^2/g is concomitant with a proportional increase in the ratio of the edge to basal plane area on going from large to small sized nanosheets. XPS analysis of these small sized nanosheets also exhibits an increase in the oxygen atomic concentration to 6.5% from 3.7% for the large sized nanosheets (Supporting information Figure 3.S3). Thus with increasing edge to basal plane area, the relative proportion of oxygen functional groups bound to the active edge sites of these nanosheets increases. While the presence of these oxygen functionalities enhances the wettability of the electrode, the decreasing particle size on the other hand significantly contributes towards a larger electronic resistivity of the electrode from increasing inter particle contact resistance. In order to retain high electronic conductivity of the electrode, here we combine the large and small sized nanosheets in an aligned conformation to achieve

enhanced capacitance while maintaining facile electronic conduction at minimum loading of large sized nanosheets inside the bulk electrode.

As described earlier, to minimize the interfacial contact resistance between the current collector and the active electrode material, a monolayer or bilayer film of large graphene nanosheets was first deposited on a stainless steel plate. As explained in the schematic diagram of Figure 3.4a, multiple layers of small sized nanosheets were then deposited at less than monolayer densities. Subsequently another monolayer of large sized nanosheets was carefully placed to uniformly overlay the small sized nanosheets. From the FESEM characterization in Figure 3.4 b-f, it is evident that a highly dispersed network of large sized nanosheets could uniformly cover the smaller ones. However, the distributed network of these large sized nanosheets was not as closely packed as was found on a smooth glass surface as a result of the surface roughness inherent in the layers of the of small sized nanosheets as compared to the film formed on a clean and smooth glass surface. However, as explained in Fig. 4 b-f, these large sized nanosheets are highly dispersed, laying flat and connected to each other near their edges to create a highly conducting aligned network inside the bulk electrode. The large sized nanosheets interact with the smaller ones through the large basal plane area and at the same time the large graphene nanosheets are also connected with each other. The top layer is firmly attached to the current collector surface. As explained in Figure 3.4 g-i, FESEM characterization clearly shows how a part of the large sized nanosheet is covering the small sized ones and then extending to strongly attach itself with other large sized nanosheets at the top section.

Figure 3.4: **Fabrication of aligned composite of large and small sized nanosheets:** a) The representative schematic diagram in figure 3.4a demonstrates the development of layered structure starting with a stainless steel substrate which was then coated with monolayer of large sized nanosheets followed by the deposition of layers of small sized nanosheets. A monolayer of large sized nanosheets was then deposited on top of the smaller ones not only covering the small sized nanosheets but also extending to the top section covered by the first monolayer film of large nanosheets. This layer by layer deposition continues to develop a multilayer structure as shown by the right most representative schematic image in figure 3.4a. b,c,d,e,f) FESEM characterization in figure 3.4 b-f clearly shows a monolayer coverage of large sized nanosheet placed on top of smaller ones where the large ones are individually connected with each other near their edges. g,h,i) figure 3.4 g-i shows how the large sized nanosheets are connecting the bulk electrode to the top section where it is attached on the current collector surface, the FESEM micrograph clearly shows how a part of the large sized nanosheet is covering the small sized ones and then extending to strongly attach itself with other large sized nanosheets at the top section.

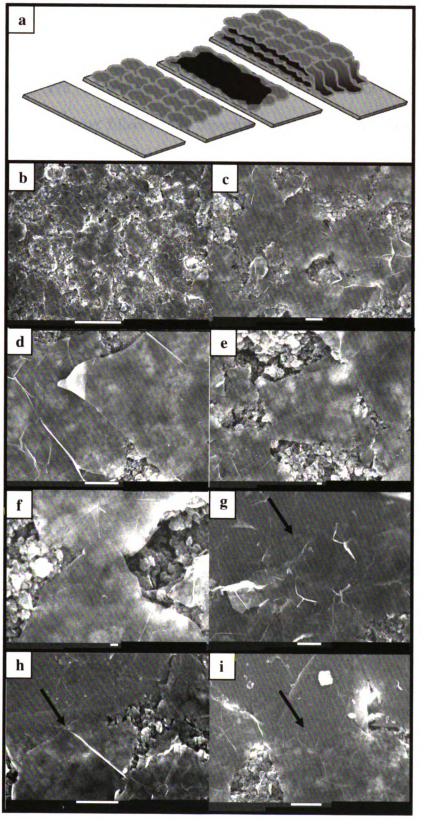
a
b
c
d
e
f
g
h
i

Specimens of this layered structure were prepared by this method to achieve 3 to 4 mg/cm^2 loading and an average thickness of 65 μm of active material for electrochemical measurements. For comparison, and to demonstrate the effect of dimension and distribution of conductive fillers on the capacitative response of the bulk electrode, one additional set of electrodes with similar area and mass loading was prepared in a conventional way by mixing small sized nanosheets with highly conductive carbon black in the presence of a binder.

As can be seen from the CV data in Figure 3.5 a-b, the retention of symmetrical CV response with nearly straight rectangular sides for the aligned configuration at scanning rates as high as 500 mV/sec clearly indicates a minimum internal resistivity and excellent electrolyte ionic accessibility throughout the porous structure of the layer assembled electrode. From the impedance analysis, the measured electrode resistance Rc of the aligned configuration is only 20 to 30 mohm, which is more than one order of magnitude less than electrodes prepared from small sized nanosheets and carbon black in the conventional way (Figure 3.5 c-d). Moreover, the disappearance of a large semi circle response in the impedance curve at high frequency for the aligned configuration again demonstrates minimum interfacial contact resistance and the uniformity of the coverage of the large sized nanosheets on the metal current collector surface.

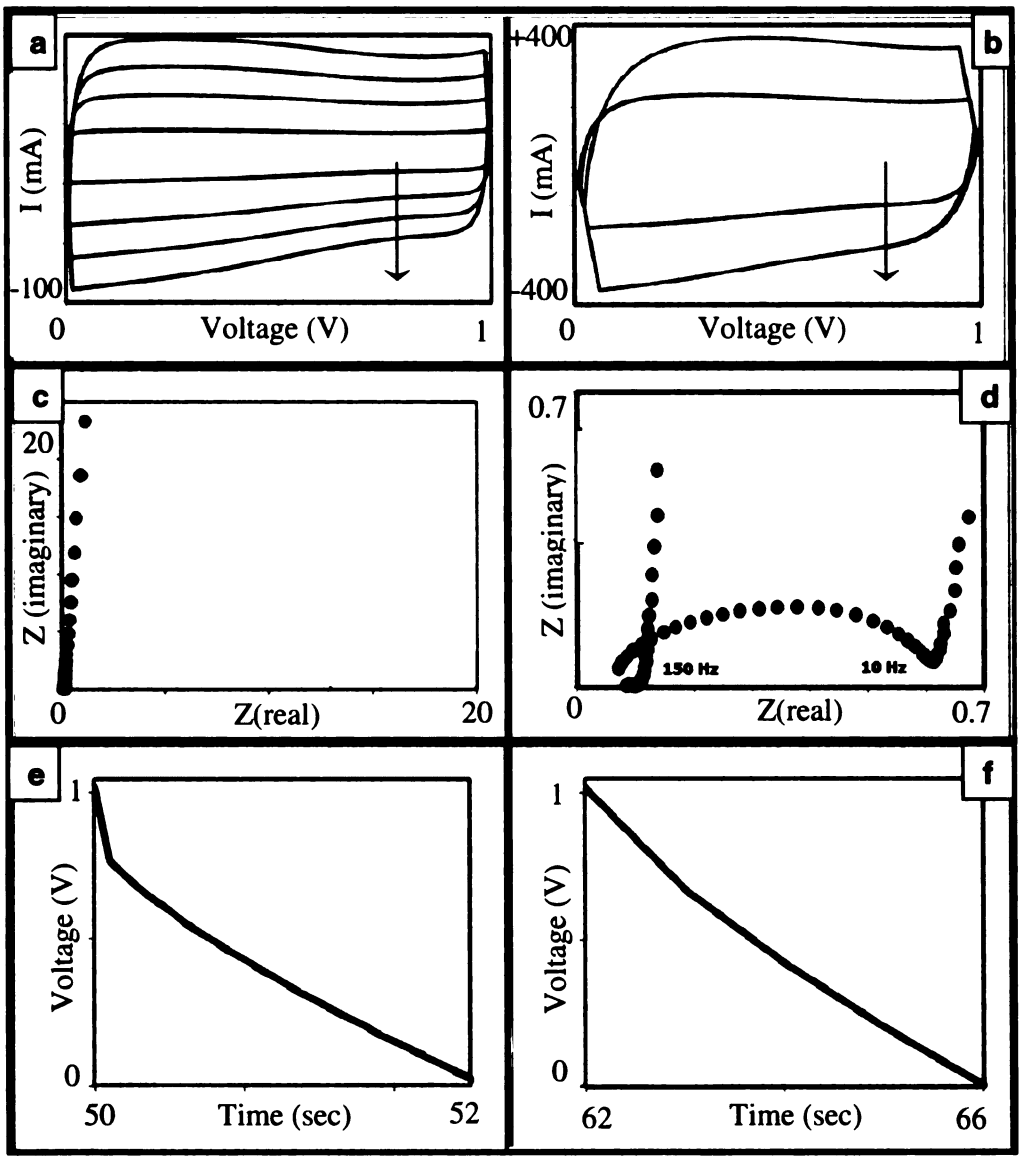

Figure 3.5: Electrochemical characteristics of aligned and randomly mixed composite electrode: a,b) Nearly rectangular CV of aligned configuration of large and small sized nanosheets at increasing voltage scanning rate from 20, 50, 75, 100, 250 to 500 mV/sec as shown in figure 3.5a and 5b. c) impedance spectra of aligned composite from high to low frequency d) high frequency impedance spectra of aligned and randomly mixed composite with the knee frequency close to 150 and 10 Hz respectively. e,f) constant current discharge characteristics of randomly mixed and aligned configuration at 6 and 10 A/g current densities respectively

A nearly vertical low frequency line and a knee frequency close to 150 Hz points to the suitability of the aligned configuration for high power applications as compared to randomly mixed composites where the knee frequency was obtained at around 10 Hz. The high rate capability of the aligned configuration is also evident from the constant current chronopotentiometric measurement. IR drop at the beginning of galvanostatic discharge is an indication of a large internal resistance of the cell [21] As shown in Figure 3.5e, a significant IR drop for the randomly mixed configurations at a current density of 6 A/g considerably limits its high rate performance as compared to the aligned configuration which continues to maintain symmetrical charge discharge characteristics even for high discharge current density at 10 A/g. The average specific capacitance of the aligned composite configuration, calculated from the slope of the discharge curve at 10 A/g, was close to 80 F/g.

From the above analysis, we conclude that this aligned configuration utilizing large sized nanosheets not only contributes towards the double layer capacitance but also acts as a series of current collectors within the bulk electrode structure for facile electronic conduction from the internal structure to the current collector surface through the large sized graphene nanosheets. The high surface area small sized nanosheets on the other hand enhance the specific capacitance by creating a highly mesoporous network and improving the wettability of the electrodes resulting from the presence of oxygen functional groups present at the edges. Moreover, we have demonstrated that the dimension and distribution of conductive fillers inside the bulk electrode have a major impact on the bulk resistivity towards achieving high frequency capacitative response for high power applications.

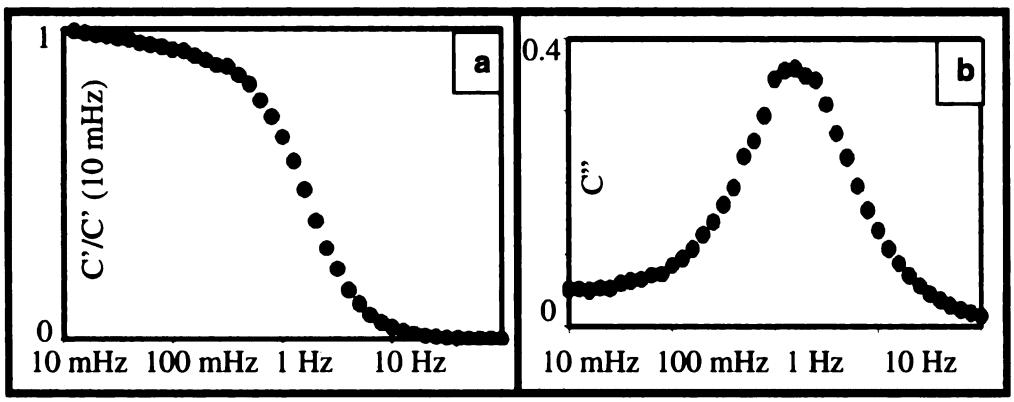

Figure 3.6: **Frequency analysis on the real and imaginary part of the capacitance:** a) Variation of the normalized real part of the capacitance $C'(\omega)/C'$ (10 mHz) with decreasing frequency b) determination of relaxation time constant (τ_0) from the imaginary part of the capacitance for the aligned configuration of large and small sized nanosheets.

The consequence of particle alignment is further evident from the frequency dependent analysis on the real and imaginary part of the capacitance. A nearly invariant capacitance with decreasing frequency for the aligned configuration makes them ideally suited for supercapacitor applications [25,26]. This is also obvious from the Bode angle plot, with a nearly parallel frequency independent phase angle close to 90^{o} up to a frequency 1 Hz (Supporting information Figure 3.S10). The determination of the relaxation time constant from the reciprocal of characteristic frequency (fo) in the frequency dependent imaginary capacitance analysis quantitatively reveals how fast the capacitor device can be reversibly charged and discharged [25,26]. As shown in Figure 3.6b, the calculated relaxation time constant for the aligned configuration is only 633 milliseconds, which was found to be more than one order of magnitude lower than the randomly mixed counterpart.

Conclusion: Self assembly of graphene nanosheets driven by the minimization of interfacial energy at the liquid-liquid interface has a distinctive advantage for the fabrication of a highly dispersed monolayer network over large macroscopic areas. Previous research employed a vacuum filtration approach from the water based dispersion of graphite oxide or reduced graphite oxide nanosheets to produce well packed and highly aligned graphene paper of various thicknesses [6,7]. The use of graphene nanosheets prepared by direct exfoliation as opposed to the graphene oxide route gives rise to a graphene nanosheets without altering the attractive, native chemical properties of graphene basal planes. Retention of the strong aromatic character of the graphene nanosheets prepared in this way causes a large inter planar interaction from the capillary force and drying induced collapse of monolayers of graphene nanosheets into a flexible and 100% binder free multilayer, free standing film. The resulting multilayer film exhibits superior high frequency capacitative properties with a knee frequency close to 398 Hz and a nearly rectangular cyclic voltammogram at 1000 mV/sec for high power EDLC applications. A major benefit in our approach is that nanomaterials of a desired architecture along with graphene's attractive physical and chemical characteristics can be synthesized into an architecture consisting of large and small graphene nanosheets into a highly dispersed and aligned network in a bulk macroscopic configuration designed to maximize device performance. Monolayers of large sized nanosheets function as a series of highly electrically conducting current collectors within the mesoporous network of small sized graphene nanosheets for improved rate capability of EDLC electrode with a specific capacitance of 80 F/g at a high discharge current density of 10 A/g. These inexpensive graphene nanosheets and the ease of the process to produce the aligned

nanostructure make this new material and method highly advantageous for high power supercapacitor applications.

Experimental details:

Formation of multilayer film of graphene nanosheets: Nanosheets with an average thickness of 3 to 5 nm and width 15 μm were first dispersed in chloroform by sonication by using a 1 inch probe Sonicator. The sonication power was kept at 150 Watt during 1 minute of sonication. In this dispersion water was added to get a two phase mixture of water and chloroform. This two phase mixture was then briefly sonicated for one more minute at 150 Watt to get the nanosheets absorbed at the liquid-liquid interface. Once the nanosheets were adsorbed at the interface, they could not be brought back to the bulk phase even after vigorous shaking. However, upon shaking the interface numerous emulsion droplets were formed with the nanosheets still covering the interface between the two immiscible liquids. Droplets, reaching the air water interface, spread in the form of a thin film and the rapid evaporation of chloroform results in a dry film of graphene nanosheet floating at the air-water interface. This film was then lifted by pulling a substrate through the air-water interface. Then it was heated at 100 C to remove the residual water. Multilayer film was formed by successive depositions of these monolayer films one on top of another.

Detachment of multilayer film from the glass substrate: For detachment, the multilayer film on the glass substrate was immersed in slightly warm water at around 50 to 60 C for few hours. At this condition, water slowly wets the glass surface and causes the

displacement of this highly hydrophobic film from the glass surface to a state where it floats on the water surface. The film was then carefully lifted and dried at 100 C.

Electrochemical measurements of the electrodes: Multilayer film developed on the polished stainless steel substrate was directly used as an electrode for electrochemical measurements. All the electrochemical measurements were carried out in 'versaSTATMC' multichannel potentiostat/galvanostat instrument from Princeton applied Research, Ametek. The two electrode cell was constructed by placing a whatman cellulose filter paper (~150 μm thick) in between two electrodes as a separator and the assembly was tightened between two transparent nylon plates by using threaded bolts. For all the measurements, 6M KOH in water was used as electrolyte. The frequency response characteristics were analyzed by using versastudio software from Princeton Applied Research. EIS was measured at a frequency range from 10000 Hz to 0.01 Hz with 0 V mean voltage and amplitude 10 mV. All the results presented here, were recorded after cycling the electrodes for 50 times at 100 mV/sec scanning rate. The electrodes were cycled at increasing current densities from 1 to 30 A/g in constant current galvanostatic measurements.

Preparation of randomly mixed electrode of small sized nanosheets and highly conductive carbon black: The composition of the aligned electrode configuration was measured by a precision balance from weighing the total amount of large sized nanosheets used to prepare the electrode. The average mass of five samples of was taken to determine the composition of small and large sized nanosheets in the bulk electrode. The same composition was maintained for the randomly mixed electrodes. Usually the average loading of the large sized nanosheets in the aligned configuration was less than

7wt%. To prepare randomly mixed electrodes with small sized nanosheets and highly conductive carbon black, the materials in a wt ratio of 89:7:4 were first mixed with a binder PVDF in the presence of isopropanol to make concentrated slurry. The slurry was stirred overnight for better mixing of the ingredients. The slurry was then spread on stainless steel current collector with similar mass and area loading like the aligned configuration and then dried under vacuum at 85 C to remove isopropanol.

Instruments and measurements: TGA analysis was carried out at 5 C/min in air by Hi-Res Thermo Gravimetric Analyzer from TA instrument. For XPS measurements, a Perkin Elmer Phi 5400 ESCA system was used for experimentation with a magnesium K α X-ray source. Samples were analyzed at pressures between 10^{-9} and 10^{-8} torr with a pass energy of 29.35 eV and a take-off angle of 45°. The spot size was roughly 250 μm. Contact angle was measured on KRUSS drop shape analysis system, DSA 10Mk2. The Raman spectra were measured by using LabRAM ARAMIS from Horiba Jobin Yvon at 532 nm wavelength with 10 x aperture.

FESEM images were taken by JEOL JSM-7500F scanning electron microscope. The electrical conductivity was measured by four point probe set up from Keithley 2400 source meter.

Calculations: The capacitance was calculated from the slope of the discharge curve from the constant current galvanostatic measurement according to the equation 1,2 [21]

$$C = I / (dV/dt)$$

where C is the capacitance (F) of the cell, I (A) is the constant discharge current and (dV/dt) is the slope of the discharge curve in V/sec. For this two electrode system, the specific capacitance of the active electrode material was determined from the mass of the single electrode as,

$$Csp = 2C / m$$

The real and imaginary part of the capacitance was determined by using the equations1,2

$$C'real(\omega) = - Z''(\omega) / (2.\pi.f (|Z(\omega)|)^2) \ldots\ldots\ldots(1)$$

$$C''imaginary (\omega) = - Z'(\omega) / (2.\pi.f (|Z(\omega)|)^2) \ldots\ldots\ldots(2)$$

Where f is the frequency and Z', Z'' and Z are the real part, imaginary part and total impedance of the cell.

The conductivity of the film was measured using four point probe technique.

$$\text{Conductivity (S/cm)} = \frac{\text{[Probe spacing (cm)] x [current]}}{\text{[Width of the film (cm)] x [film thickness (cm)] x [voltage]}}$$

The probe spacing and the width of the film were 1 cm and the film thickness was 22 μm.

Supplementary information:

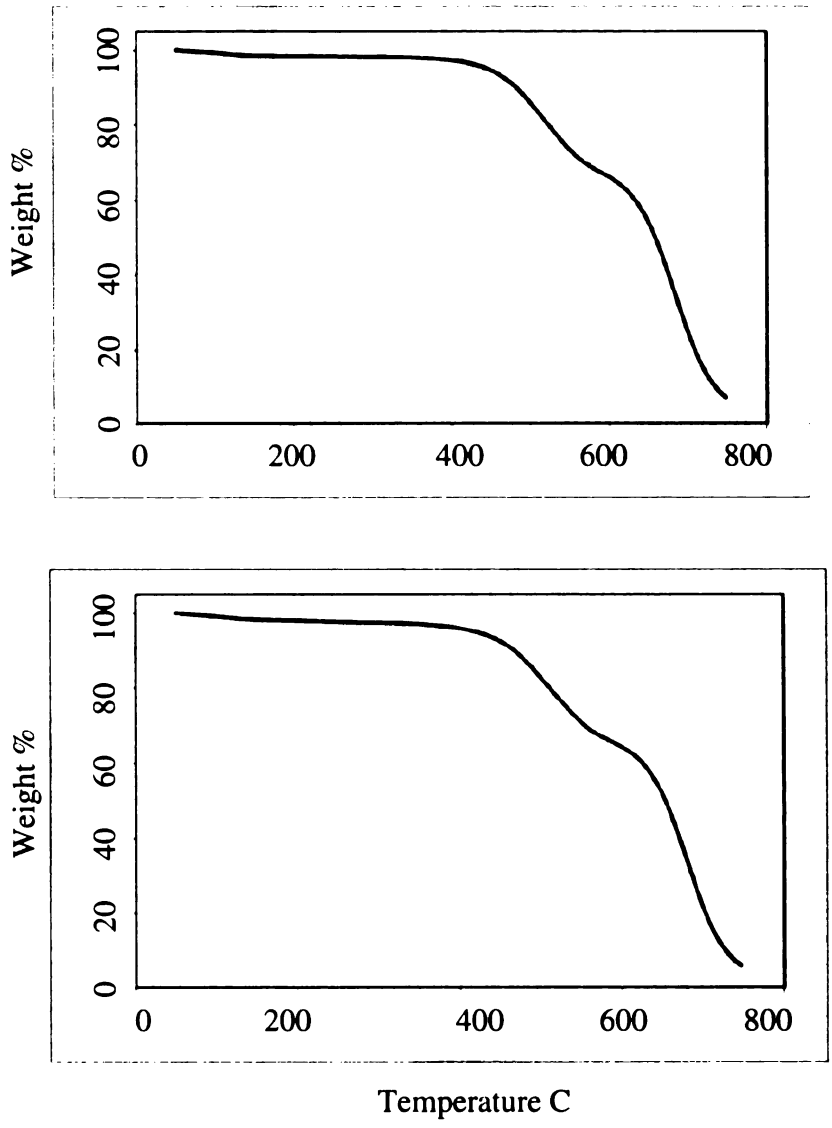

Figure 3.S1: Thermo gravimetric analysis (TGA) of graphene nanosheets (above) and multilayer free standing film (below) in air at 5 C/min temperature ramping rate

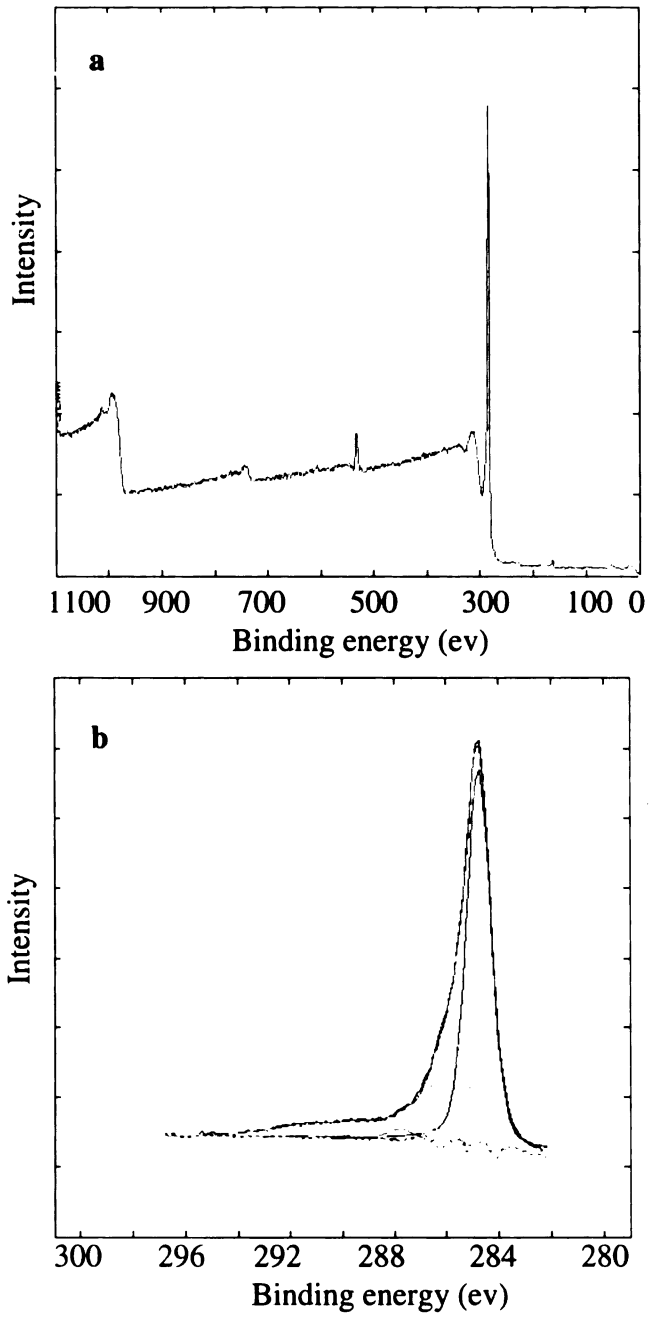

Figure 3.S2: Large sized graphene nanosheets a) survey spectra b) C1s spectra

Atomic concentrations: C1s – 95.70, O1s – 3.71, S2p – 0.59

Elemental traces of acidic residue are sometimes found in the XPS analysis in the form of sulfur or nitrogen. However, the major elemental atomic concentration besides carbon is

always oxygen. Similar result is also found from the elemental XPS analysis for mechanically milled small sized nanosheets as reported in supplementary figure S3.

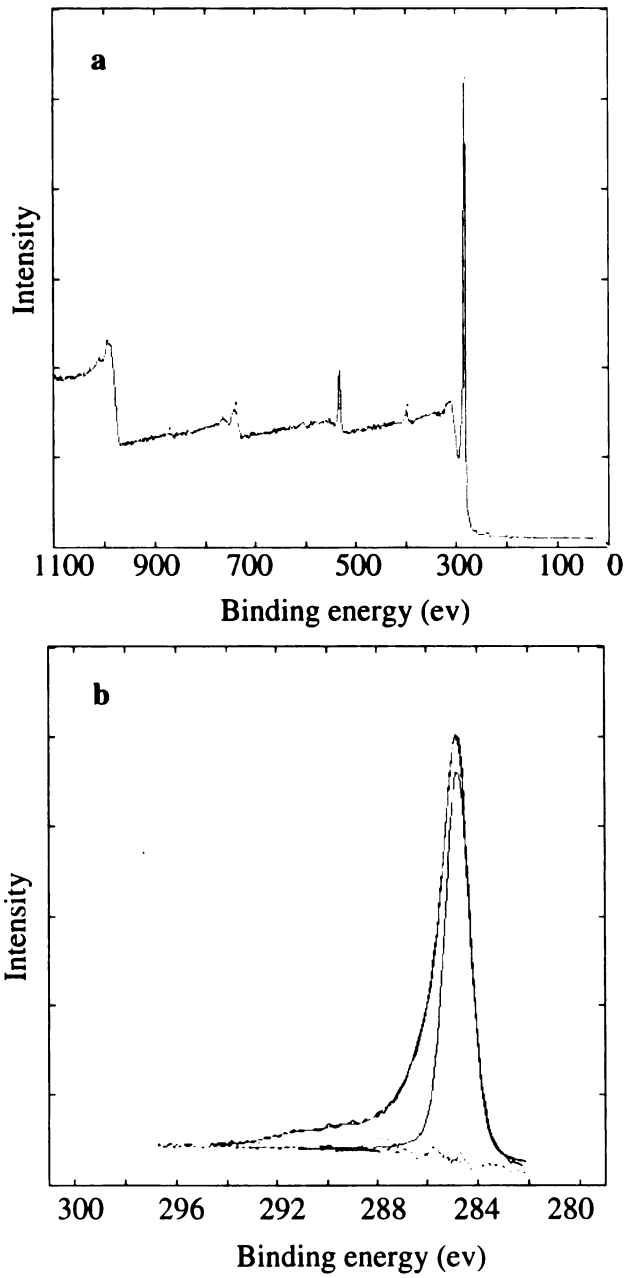

Figure 3.S3: Mechanically milled small sized graphene nanosheets a) survey spectra b) C1s spectra

Atomic concentrations: C1s – 92.47, O1s – 6.32, N1s – 1.21

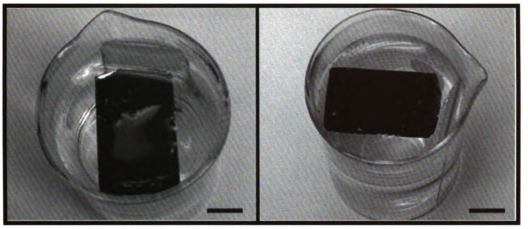

Figure 3.S4: The film is detached from the glass substrate and is floating on the water surface (scale bar is 1 cm)

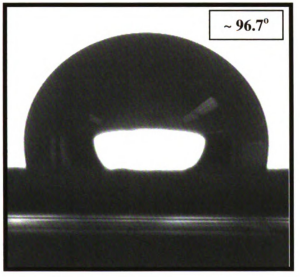

Figure 3.S5: Contact angle measurement of water droplet placed on multilayer graphene nanosheet film

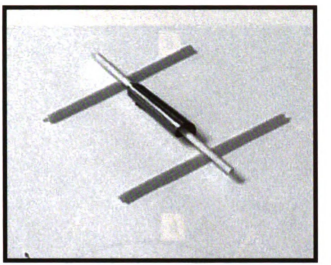

Figure 3.S6: Multilayer graphene nanosheet film scrolled into cylindrical shape

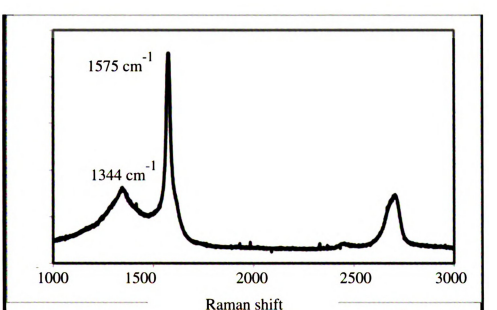

Figure 3.S7: Raman spectra of multilayer film of large sized graphene nanosheets exhibiting a sharp G band peak and a low D band peak.

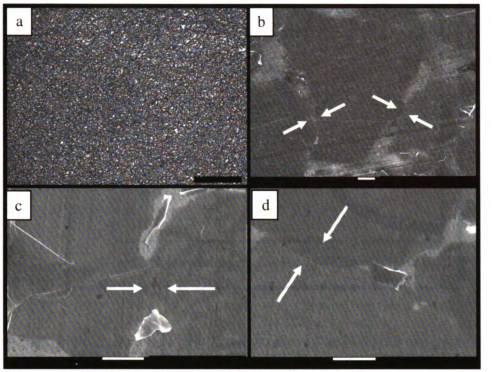

Figure 3.S8: Monolayer distribution of large sized graphene nanosheets on the stainless steel substrate; figure (a) shows the distribution of nanosheets on the substrate at low magnification (scale bar 50 μm) whereas figure (b-d) shows the interconnectivity of flat nanosheets on the substrate at high magnification (scale bar 1 μm), arrows indicate how the nanosheets are connected with each other near their edges

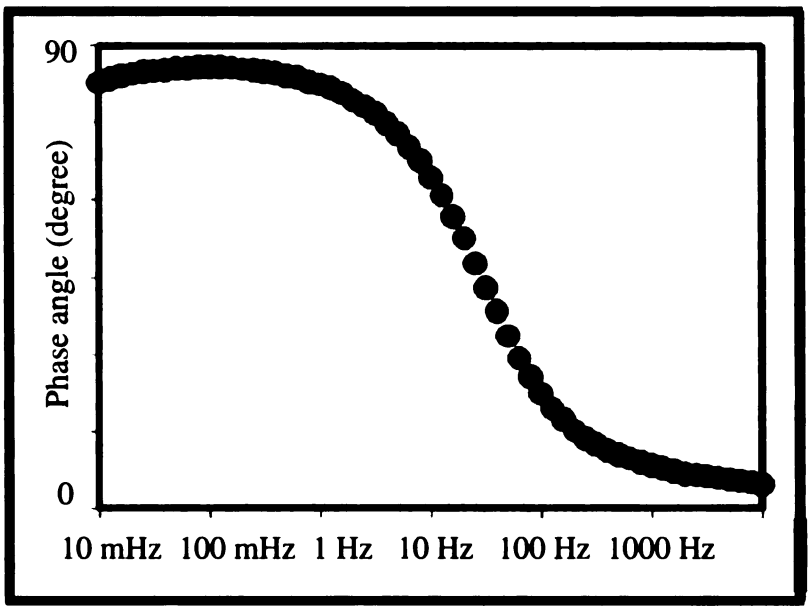

Figure 3.S9: Multilayer film of large sized graphene nanosheets showing a phase angle close to 90^{o} up to a frequency 10 Hz.

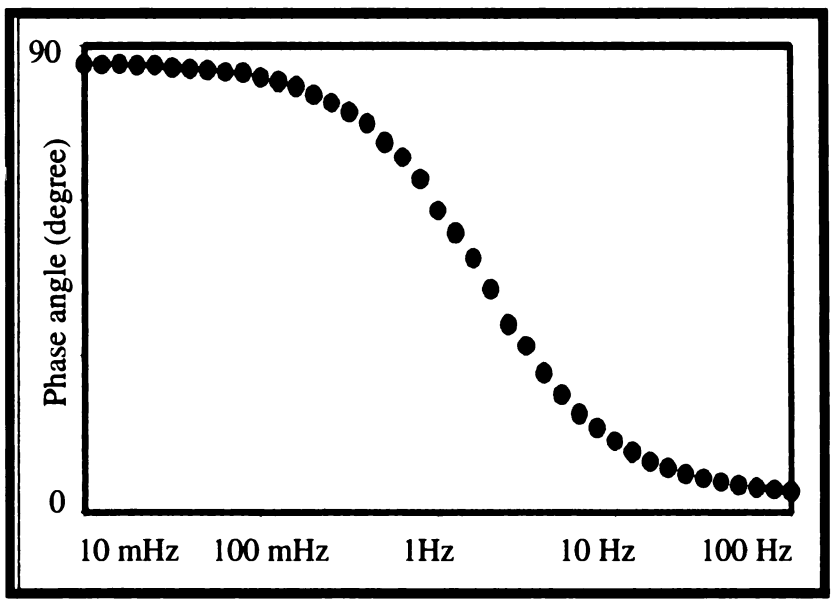

Figure 3.S10: Aligned composite of large and small sized nanosheets showing a phase angle close to 90^{o}

References:

1. Geim, A. K.; Novoselov, K. S. Nature materials **2007**, 6, 183-191

2. Castro, A.H.N; Guinea, F.; Peres, N. M. R.; Novoselov, K. S.; Geim, A. K. Review Modern. Physics, **2009,** 81, 109-162

3. Jang, B. Z.; Zhamu, A. J. Mateials. Scienc, **2008,** 43, 5092–5101

4. Avouris, P.; Chen, Z.; and Perebeinos, V. Nature Nanotechnology **2007,** 2, 605 – 615

5. Drzal, L. T.; Fukushima, H. Expanded graphite and products produced therefrom. US patent application 20040127621

6. Dikin, D. A. Stankovich, S.; Zimney, E. J.; Piner, R. D.; Domett, G. H. B.; Evmenenko, G.; Nguyen, S. T.; Ruoff, R. S.; Nature **2007,** 448, 457-460

7. Park, S.; An, J.; Piner, R.D.; Jung, I.; Yang, D.; Velamakanni, A.; Nguyen, S. T.; Ruoff, R.S.. Chemistry of Materials **2008,** 20, 6592–6594

8. Park, S.; An, J.; Jung, I.; Piner, R.D.; An, S. J.; Li, X.; Velamakanni, A.; Ruoff, R.S.. Nano Lettters, **2009,** 9, 1593-1597

9. Lu, J.; Drzal, L.T.; Worden, R.M.; Lee, I. Chemistry of materials. **2007,** 19, 6240–6246

10. Biswas, S.; Drzal, L. T. Nano Letters, **2009,** 9, 167–172

11. Futaba, D. N., Hata, K.; Yamada, T.; Hiraoka, T.; Hayamizu, Y.; Kakudate, Y.; Tanaike, O.; Hatori, H.; Yumura, M.; Iijima, S. Nature Materials, **2006,** 5, 987 – 994

12. Kaur, S.; Sahoo, S.; Ajayan, P. M.; Kane, R. S. Advanced Materials **2007,** 19, 2984–2987

13. Ci, L.; Manikoth, S. M.; Li, X.; Vajtai, R.; Ajayan, P. M. Advanced Materials, **2007,** 19, 3300–3303

14. Liu, H.; Zhaia, J.; Jiang, L. Soft Matter, **2006,** 2, 811–821

15. Chakrapani, N.; Wei, B.; Carrillo, A.; Ajayan, P. M.; Kane, R. S. Proceedings of National Academy of Science USA **2004,** 101, 4009-4012

16. Cote, L. J.; Kim, F.; Huang, H. J. J. American Chemical Society **2009,** 131, 1043–1049 (2009)

17. Israelachvili, J. N. Intermolecular And Surface Forces 2nd ed. (Academic Press: San Diego, 1992)

18. Graf, D.; Molitor, F.; Ensslin, C.; Stampfer, C.; Jungen, A.; Hierold, C.; Wirtz, L. Nano Letters, **2007,** 7, 238-242

19. Casiraghi, C.; Hartschuh, A.; Qian, S.; Piscance, S.; Georgi, C.; Fasoli, A.; Novoselov, K.S.; Basko, D.M.; Ferrari, A.C. Nano letters, **2009,** 9, 1433-1441

20. Kudin, K. N.; Ozbas, B.; Schniepp, H.C.; Prudhomme, R.K.; Aksay, I.A; Car, R. Nano Letters, **2008,** 8, 36-41

21. Conway, B. E. Electrochemical Supercapacitors: Scientific Fundamentals and Technological Applications (Plenum Publishers: New York, 1999)

22. Du, C.; Yeh, J.; Pan, N. Nanotechnology, **2005,** 16, 350–353

23. Talapatra, S. Kar, S.; Pal, S.K.; Vajtei, R.; Ci, L.; Victor, P.; Shaijumon, M. M.; Kaur, S.; Nalamasu, O.; Ajayan, P. M.; Nature Nanotechnology, **2006,** 1, 112 – 116

24. Du, C.; Pan, N. J. Power Sources **2006, 160,** 1487–1494

25. Chmiola, J.;Yushin, G.; Dash, R.; Gogotsi, Y. J. Power Sources **2006,** 158, 765–772

26. Taberna, P.L; Simon, P.; Fauvarque, J. F. J. Electrochemical Society **2003,** 150, A292-A300 (2003)

CHAPTER 4

MULTILAYERED NANO ARCHITECTURE OF GRAPHENE NANOSHEETS AND POLYPYRROLE NANOWIRES FOR HIGH PERFORMANCE SUPERCAPACITOR ELECTRODES

Abstract: A novel nano architecture is developed by combining the nanostructured conductive polymer polypyrrole with highly electrically conductive graphene nanosheets in a multilayered configuration to achieve high specific capacitance and low electronic resistance for supercapacitor electrode applications. The fibrous network of polypyrrole nanowires with high electrolyte ionic accessibility was interspersed with electrically conductive monolayers of highly aligned large sized graphene nanosheets as a series of current collectors within the macroscopic configuration for enhanced electronic charge transport inside the electrode. A fabrication method relying on capillary force driven self assembly coupled with the strong van der Waals attraction between highly aromatic graphene basal plane and π conjugated conductive polymer chains to create a 100% binder free multilayered composite structure of these two distinct nanoscale elements to construct the electrode. This multilayer composite electrode exhibits a high specific capacitance of ~165 F/g with a nearly ideal rectangular cyclic voltammogram at increasing voltage scanning rates and high electrochemical cyclic stability.

Significance of the research: A novel nano architecture has been developed by combining the nanostructured conductive polymer polypyrrole with highly electrically conductive graphene nanosheets in a multilayered configuration to achieve high specific capacitance and low electronic resistance for supercapacitor electrode applications.

Previous research employed a chemical or electro polymerization approach to uniformly cover graphene nanosheets or carbon nanotubes with thick polymer coatings to prepare composite electrodes for supercapacitor applications. Instead of using chemical or electro polymerization technique to wrap the nanosheets completely, in this new approach aligned monolayers of graphene nanosheets are interspersed within the fibrous network of polypyrrole as a series of current collectors inside the multilayer bulk electrode configuration. Capillary driven self assembly coupled with the strong van der Waals force of attraction between highly aromatic graphene basal plane and π conjugated conductive polymer chains was employed to create a 100% binder free multilayered composite of these two distinct nanostructured elements to construct the electrode. The high performance of this electrode resulted from the strong van der Waals force of attraction between the large graphene basal plane and the π conjugated polymer chain. Impedance analysis clearly demonstrated the low equivalent series resistance obtained from the interlayer charge transport between graphene nanosheets and the polypyrrole nanowires. The facile electronic charge transport between the graphene nanosheets also had a stabilizing affect on the electrochemical cyclic stability of this composite electrode. This multilayer film electrode displays symmetric charge-discharge characteristics and a nearly ideal rectangular cyclic voltammogram with increasing voltage scanning rate from 10 to 100 mV/sec. Maintaining a high frequency capacitative response with a knee frequency close to 50 Hz this nano architecture exhibits ~165 F/g specific capacitance at 1A/g discharge current density at the end of 1000 electrochemical cycles.

Introduction: The highly aromatic two dimensional macromolecule graphene, with exceptionally low intrinsic electrical resistivity is a potential candidate as a novel electrode material for electrochemical energy storage applications [1-3]. Exfoliated graphene nanosheets with stacks of a few single layers of graphene can be simply and inexpensively prepared from acid intercalation and thermal exfoliation of natural graphite without requiring extensive chemical oxidation to graphite oxide and subsequent reduction back to graphene [4,5]. The average thickness of these nanosheets ranges from 3 to 5 nm with a lateral dimension close to 15 μm [4,5]. A homogenous and orderly distribution of these highly aromatic large sized nanosheets in combination with other nanomaterial can be nanostructured into a bulk macroscopic configuration which can exploit the unique properties as well to maximize device performance.

In an electrical double layer capacitor, the electrochemical charge storage ability of aromatic graphene basal plane arises from the electronic and the ionic charge separations at the electrode-electrolyte interfaces [6-8]. On the other hand, the faradic charge transfer mechanism across the electrode-electrolyte interface significantly boosts the charge storage capacity of redox or pseudocapacitors when graphene is combined with conductive polymers [6, 9-14]. The use of a conductive polymer like polypyrrole is particularly promising owing to its high energy storage capacity, good electrical conductivity, ease of low cost synthesis and environmental stability [9-12]. However, the realization of high specific capacitance is only possible with effective electrolyte transport to the active sites for enhanced faradic charge transfer reactions. A nanostructured fibrous network of polypyrrole is therefore expected to demonstrate rapid ionic transport within the bulk matrix [10, 15-17]. However, even with increased ionic

transport to the active sites, the rate capability of conductive polymers is limited by the change in the structural conformation with repeated ion exchange and consequent diminution of electrical properties with increasing electrochemical cycles [18]. Introduction of carbon nanomaterials such as carbon nanotubes or graphene is highly favorable to create an electrically conducting network to improve the electrochemical cyclic stability of the electrode. The conventional techniques such as the electro polymerization or chemical polymerization uniformly encapsulate the carbon nanomaterials with a thick polymer coating and individual nanosheets can no longer form an interconnected network inside the bulk electrode matrix which is highly desirable to reduce the electronic resistance to improve the electrochemical stability and also to achieve rapid charge discharge characteristics at high discharge current densities [12,14, 19-20]. This research shows that it is possible to integrate the polymerized nanostructure polypyrrole with graphene nanosheets in a directed self assembly approach governed by the large van der Waal's force of attraction between the graphene basal plane and the π conjugated polymer in a layered composite structure. Taking advantage of capillary force driven self assembly of layers of polypyrrole nanowires and graphene nanosheets, this approach can create a multilayered nano architecture with a homogeneous and orderly distribution of graphene nanosheets for enhanced performance supercapacitor electrode.

Experimental details: Pyrrole monomer, Cetyltrimethylammonium bromide (CTAB), Ammonium persulfate (APS) and Sodium chloride was purchased from Sigma Aldrich and were used without any further purification.

Graphene nanosheets were prepared by following the method described earlier. Polypyrrole nanowire was prepared by following the method by Wu et al [10]. In this chemical polymerization process, 0.91 gm of the surfactant CTAB is mixed with 0.3 ml of pyrrole monomer in 125 ml of 0.2M aqueous HCl solution. The mixture was then stirred at 0 to 5 C for 2 hrs. Then the oxidizing agent Ammonium per sulfate (APS), dissolved in 10 ml of 0.2 M HCl solution, was added dropwise to the CTAB and Pyrrole mixture. The mixture turned light green to dark green in few minutes. The mixture was allowed to stir at 0 to 5 C for 24hrs. The black precipitate was filtered and washed with copius amounts of water to remove any excess acid or surfactant.

Monolayer films of graphene nanosheets were prepared by following the technique earlier [5]. To prepare the nanowire film, 0.1 gm of nanowire were dispersed in water by sonicating the mixture for few minutes. Then chloroform was added as the second immiscible phase and the mixture was again sonicated to cause the nanowire to adsorb at the liquid-liquid interface. The interface was then shaken to produce emulsified droplets, which float to the air-water surface where the chloroform evaporates leaving a dry thin film of nanowires at the air water interface. This film was then transferred by pulling the substrate through the interface.

For electrochemical measurements, a 1M NaCl aqueous solution was used as electrolyte. The multilayer structure of graphene nanosheets and polypyrrole nanowire was assembled on a stainless steel current collector which was separated by a Whatman filter paper. The two electrode assembly was compressed between transparent nylon plates at the top and bottom and was immersed in the electrolyte for electrochemical measurements.

Instrument: All the electrochemical measurements were carried out in 'versaSTATMC' multichannel potentiostat/galvanostat instrument from Princeton Applied Research, Ametek. The frequency response characteristics were analyzed by using versastudio software from Princeton Applied Research. EIS was measured at a frequency range from 10000 Hz to 0.01 Hz with 0 V mean voltage and amplitude 10 mV. FESEM images were taken by JEOL JSM-7500F scanning electron microscope. The electrical conductivity was measured by four point probe set up from Keithley 2400 source meter. The probe arrangement was linear and the spacing was 1 cm. To measure the electrical properties a thin film of polypyrrole was deposited on a glass slide and the sample was pressed against the probes by spring loaded attachment. The electrical conductivity was measured using the following relation,

$$\text{Conductivity (S/cm)} = \frac{\text{[Probe spacing (cm)] x [current]}}{\text{[Width of the film (cm)] x [film thickness (cm)] x [voltage]}}$$

Result and discussion: Fabrication of multilayered nano architecture with large and small sized nanosheets of graphene nanosheets from the liquid-liquid interfacial approach have been earlier demonstrated to develop a supercapacitor electrode with enhanced capacitance and improved rate capabilities. In this approach, the use of monolayers of highly electrically conductive large sized graphene nanosheets serves as a series of current collectors within the multilayer configuration to achieve rapid charge-discharge characteristics with minimum equivalent series resistance. In a similar approach here we integrate the large sized graphene nanosheets with polypyrrole nanowires to investigate

the effect of reduced electronic resistance and increased ionic accessibility from the presence of fibrous network of nanowires on the electrochemical energy storage, rate capability and cyclic stability of this new composite supercapacitor electrode.

A surfactant assisted soft template approach was employed to prepare polypyrrole nanowire with an average diameter from 40 to 60 nm [10,21]. The specific surface area of the fibrous nanowire, obtained from nitrogen adsorption technique at liquid nitrogen temperature, was 91 m^2/g. The total pore volume obtained from single point adsorption at ~0.98 relative pressure was 0.376 cm^3/g. Self assembly of hydrophobic organic nanowires at the liquid-liquid interface was demonstrated earlier [22]. The hydrophobicity of polypyrrole nanowire was confirmed by the contact angle (~ 69^o) formed by a water droplet on a dry film. With this reasonable hydrophobicity, these nanowires can be adsorbed at a liquid-liquid interface and can be subsequently transported to the air-water interface to form a thin film, floating on the water surface. The film can then be easily transferred on a desired substrate by pulling the substrate through the air water interface.

To investigate the morphology and dispersion of polypyrrole nanowires on the graphene nanosheets, a thin film of nanowires was first transferred to a substrate coated with a monolayer film of graphene nanosheets [5]. The nanowires are wet by a thin film of water and are in close contact with the graphene nanosheets. With continuous evaporation of water, the strong capillary force causes the interlayer separation between the nanowires to decrease and the layers to collapse on each other. After complete liquid evaporation, the strong van der Waal's force of attraction between the highly aromatic

graphene basal plane and the π conjugated polymer film assembles these two nanostructures on top of another. The adhesion of the nanowires to the graphene nanosheets was found to be sufficiently strong to resist removal under flowing water. FESEM micrographs in Figure 4.1a,b clearly show the highly dispersed network of polypyrrole nanowires deposited on the graphene nanosheet.

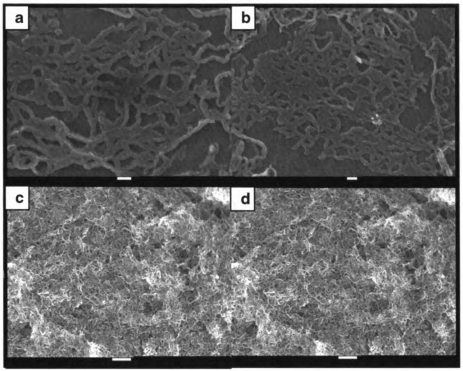

Figure 4.1: Morphology of polypyrrole nanowire: A highly dispersed network polypyrrole nanowire with an average diameter of 40 to 60 nm is attached to the large basal plane of graphene nanosheets in figure a,b. With multilayer deposition, the highly fibrous morphology of these nanowires is shown in figure c,d

The interaction between the nanowires on the aromatic graphene basal plane was investigated by Raman analysis. For graphene the nanosheets in Figure 4.2a, the high

intensity of the G band peak at 1575 cm^{-1} as compared to the low intensity "disordered and defect" D band peak at1344 cm^{-1} demonstrates the aromatic purity of the graphene basal plane. As shown in Figure 4.2b, for the control polypyrrole nanowire sample the appearance of peaks near 1572 cm^{-1} and 1330 cm^{-1} arises from the π conjugated structure and ring stretching mode of the polymer backbone respectively [23-26]. The broad peak obtained near 1046 cm^{-1} corresponds to the C-H in-plane deformation and two small peaks near 927 and 977 cm^{-1} are associated with the quinoid polaronic and bipolaronic structure respectively [23-26]. With the deposition of thin film of polypyrrole nanowire on the graphene nanosheet, the Raman spectra as shown in Figure 4.2c is essentially composed of both pure polypyrrole and graphene nanosheets. For this composite thin film, reappearance of bands near 927, 977 and 1046 cm^{-1} are identical to the pure polypyrrole sample. However, as compared to the pure polypyrrole sample, the increase in the ratio of the sharp G band peak at 1575 cm^{-1} as compared to the defect band near 1338 cm^{-1} reflects the interaction between the π conjugated nanowire and aromatic graphene basal plane without compromising the chemical identity of either of these two nanomaterials.

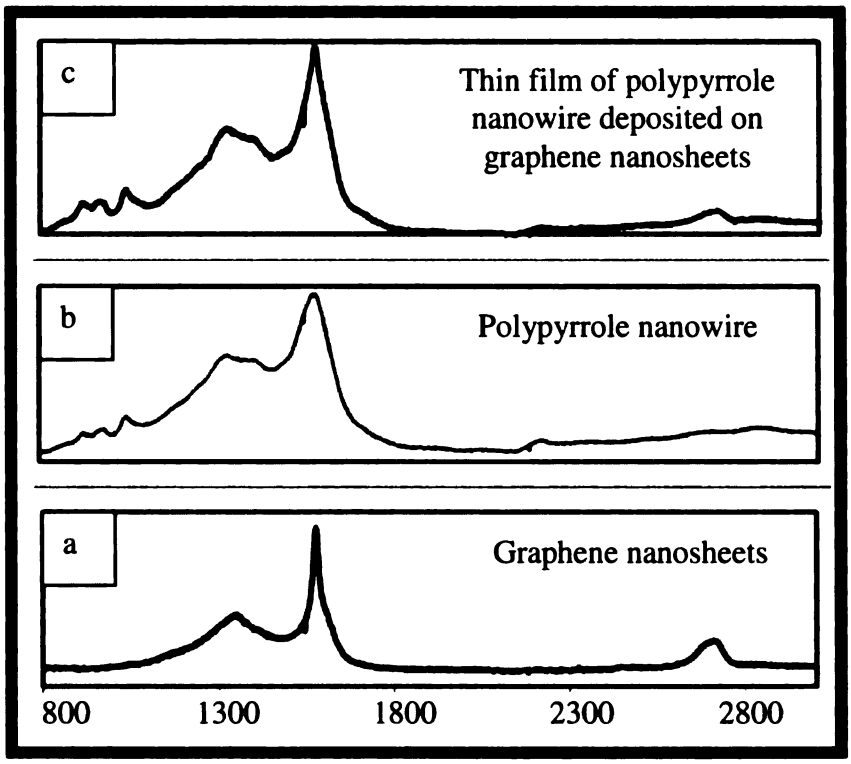

Figure 4.2: Raman spectra analysis: a) Graphene nanosheets with sharp G band, D band and 2D peaks at 1575,1344 cm^{-1} and 2700 cm^{-1} b) Polypyrrole nanowire with peaks near 927, 977, 1046, 1330, 1572 cm^{-1} c) Thin film of polypyrrole nanowire deposited on graphene nanosheets with peaks near 927, 977, 1046, 1338, 1575 and 2700 cm^{-1}

The electrical conductivity of the polypyrrole nanofibrous film was 65 S/m measured with a standard four point probe method. The graphene nanosheet film on the other hand exhibited a two orders of magnitude higher electrical conductivity of the order of 1.25×10^4 S/m. In order to exploit this high electrical conductivity of graphene nanosheets, polypyrrole nanowires were interspersed between graphene nanosheets in a multilayer configuration to form a supercapacitor electrode.

As illustrated in Figure 4.3a, the frabrication of the multilayer film electrode requires the formation and deposition of a bilayer film of large sized graphene nanosheets on the stainless steel plate to minimize the interfacial contact resistance between the active electrode material and the current collector surface. Multiple layers of polypyrrole nanowires were then deposited on top of this monolayer film of graphene nanosheets to create a fibrous network of nanowire as shown in Figure 4.1c,d and Figure 4.3b. Subsequently another monolayer of large sized graphene nanosheets was placed to uniformly cover the fibrous network of polypyrrole nanowires (Figure 4.3c).

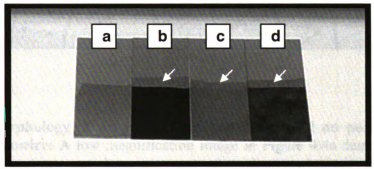

Figure 4.3: Development of multilayer structure of graphene nanosheets and polypyrrole nanowire: In Figure 4.3a, the stainless steel substrate is coated with a bilayer film of graphene nanosheets, in Figure 4.3b multilayer of polypyrrole nanowire was deposited on the bilayer graphene nanosheets film, in Figure 4.3c a monolayer of graphene nanosheets deposited covering the PPy nanowire and also extending to the top section to attach to the current collector surface, in Figure 4.3d one layer of PPy nanowire deposited on monolayer graphene film, the process is repeated to create the multilayer structure

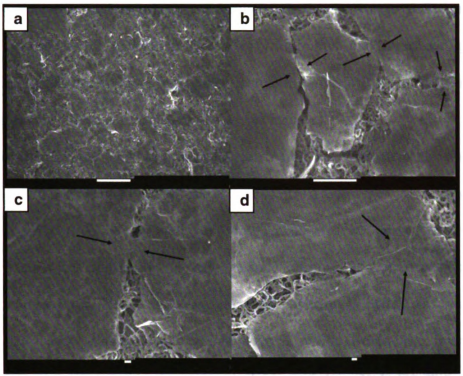

Figure 4.4: Morphology of graphene nanosheets deposited on polypyrrole nanowire: A low magnification image in Figure 4.4a demonstrates the uniform monolayer coverage of graphene nanosheets deposited on the fibrous network of polypyrrole nanowire. High magnification images from Figure 4.4 b,c,d clearly exhibits the dispersed interconnected network of graphene nanosheets near their edges (indicated by the arrows)

The FESEM images in Figure 4.4 show that the nanosheets are highly dispersed and form an edge shared interconnected network to create a highly electrically conductive conduit inside the bulk electrode. These nanosheets are not only connected with each other near their edges (shown by the arrows on Figure 4.4 (b,c,d) but also interact with the polypyrrole nanowire through strong van der Waal's force of attraction with the highly

aromatic graphene basal plane. As shown in Figure 4.3b,c,d (shown by the arrows), in the top section the large sized nanosheets are firmly attached to the current collector surface to serve as a series of current collectors within this multilayer configuration. Multilayered deposition of these two nanostructured materials was repeated to produce a 100% binder free electrode for supercapacitor applications.

The electrochemical property of this multilayered film was characterized using a two electrode cell immersed in 1 M aqueous NaCl solution. To assess the effect of addition of graphene nanosheets on the capacitative response and the electrical properties of the film, a control sample was prepared by the same technique from multilayer deposition of the polypyrrole nanowires directly on the metal current collector. In EDLC performance, an oblique and narrow shaped cyclic voltammogram results from large internal and interfacial contact resistance of the active electrode materials inside the bulk electrode [6]. Figure 4.5 compares the cyclic voltammetry characteristics of the layered composite of polypyrrole nanowires and graphene nanosheets with the control polypyrrole nanowire sample. An nearly ideal rectangular shaped CV for the aligned composite at increasing voltage scanning rate from 10 to 100 mV/sec clearly demonstrates excellent ionic and electronic transport within the bulk multilayered configuration of polypyrrole nanowires and graphene nanosheets. Under similar measurement conditions, the fibrous network of the control polypyrrole sample failed to maintain the capacitative response with increasing voltage scanning rate. While the electrolyte ionic accessibility inside the bulk electrode is highly favorable from the fibrous network of the polypyrrole, it appears that the presence of series of aligned graphene nanosheets within the bulk matrix facilitates

enhanced electronic transport with high capacitative response even with increasing voltage scanning rate.

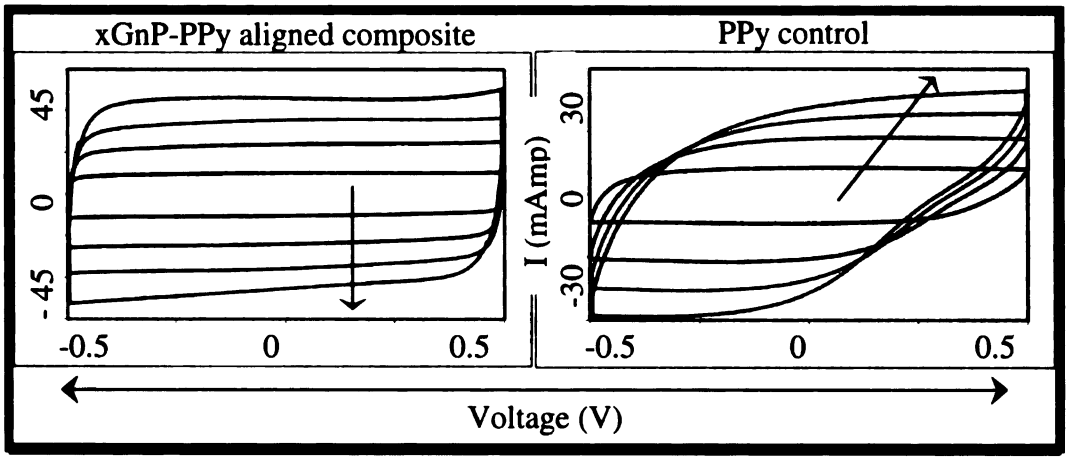

Figure 4.5: Electrochemical characterization: Cyclic voltammetric characteristics of multilayer composite of polypyrrole (PPy) / graphene nanosheets and control polypyrrole sample are compared in Figure 4.5 at increasing voltage scanning rate from 25, 50, 75 to 100 mV/sec

The enhanced electronic transport with the incorporation of aligned graphene nanosheets is also evident from the impedance analysis. The equivalent circuit of different elements from the impedance spectra is presented in Figure 4.6a. This equivalent circuit includes bulk solution resistance Rs, the contact interface resistance Rc, the double layer capacitance C_d and a pseudocapacitative element C_p from the redox process involving the conductive polymer [27,28]. The bulk solution resistance Rs and the contact interface resistance Rc is obtained from the Nyquist plot, where the high frequency semi circle intercepts the real axis at Rs and (Rs +Rc) respectively [27,28]. As shown in Figure 4.6c,d, the bulk solution resistance Rs differs by only 20 to 30 mohm for these two

electrodes. However, the contact interface resistance Rc for the aligned composite is more than one order of magnitude smaller than the control polypyrrole sample. This clearly demonstrates the reduced interfacial contact resistance between the active electrode materials inside the bulk electrode and minimum interfacial contact resistance of two dimensional large sized graphene nanosheets with the current collector surface. Moreover, the above analysis points to the strength of the underlying van der Waal's force of interaction between the polpyrrole nanowire and large aromatic graphene basal plane for facile interlayer charge transport within the composite multilayer configuration. Instead of encapsulating the graphene nanosheets with a thick polymer coating by chemical or electro-polymerization, in this new approach a series of edge shared highly aligned monolayer films incorporated inside this multilayer electrode configuration not only reduce the electronic resistance between the active electrode materials but also enhance the charge transport from the interior of the bulk electrode to the current collector surface through the strongly attached graphene nanosheets at the top section of the electrode. The higher rate capability of the aligned composite is evident from a knee frequency close to 50 Hz as shown in Figure 4.6c.

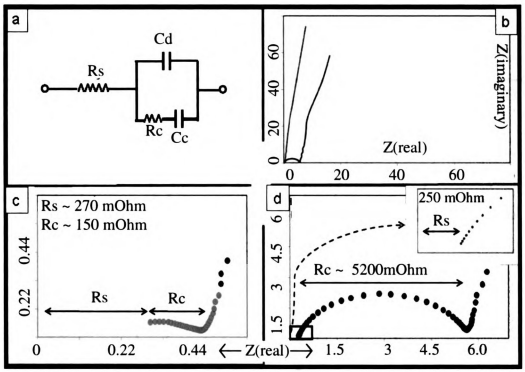

Figure 4.6: Complex plane impedance analysis: Figure 4.6a represents the equivalent circuit diagram of different elements from the impedance spectra analysis. Figure 4.6b compares the complex plane impedance characteristics from high to low frequency for the multilayer composite of polypyrrole / graphene nanosheets (green) and control polypyrrole sample (red), Figure 4.6c,d compares the high frequency responses with corresponding measurement of solution resistance Rs and contact interface resistance Rc

The increase in the charge transport also had a stabilizing effect on the capacity retention of polypyrrole nanowires under continuous electrochemical cycling. As shown in Figure 4.7, at the end of one thousand cycles, the aligned composite electrode maintains a symmetric charge-discharge shape with more than 92% capacitance retention at 1 A/g cyclic discharge current density. With increasing voltage drop (IR drop) the control

specimen of polypyrrole nanowire failed to maintain the capacitative response in less than 250 electrochemical cycles at 1 A/g discharge current densities.

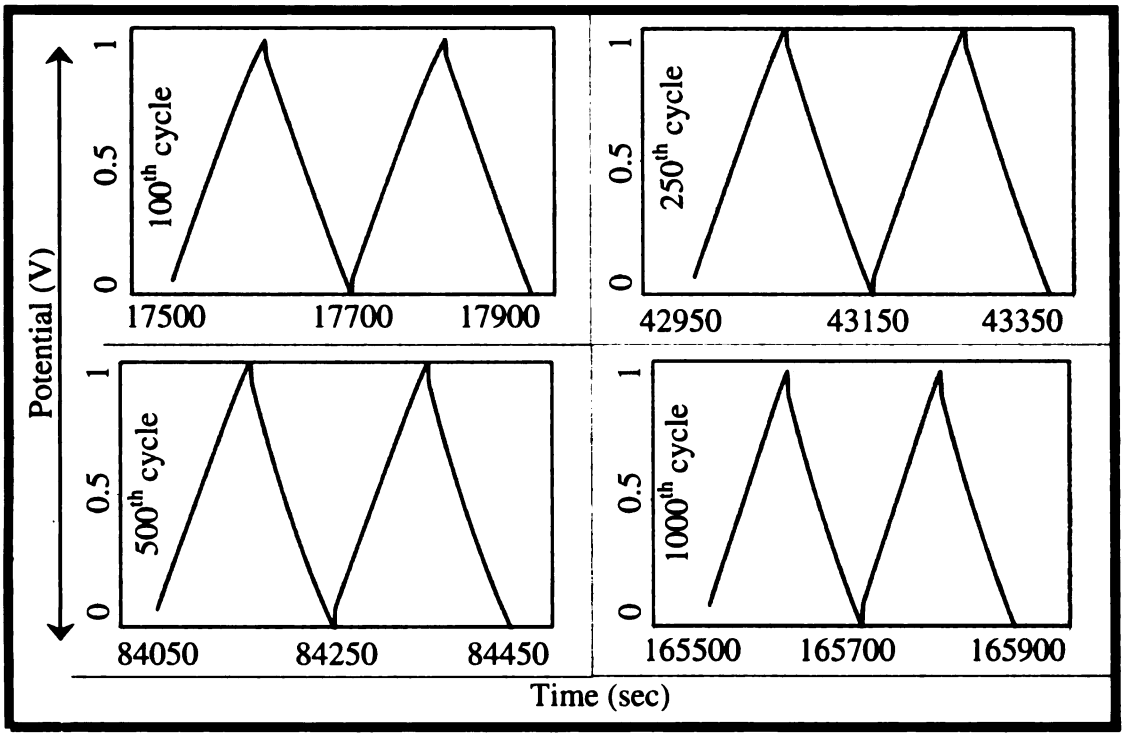

Figure 4.7: Cyclic stability: At 1 A/g constant current density, the multilayer composite of polypyrrole and graphene nanosheets continues to maintain a highly symmetric charge discharge characteristics from 100th to 1000th electrochemical cycles with a potential drop of only 30 mV

The volumetric swelling and contraction of the polymer chain from continuous injection and rejection of solvated ions and electronic charges during the cyclic electrochemical oxidation and reduction process significantly modifies the charge distribution and conformation of π conjugated polymer chains [18]. The increasing IR drop for the control polypyrrole electrode is due to this deteriorating electrical performance with increasing

electrochemical cycling. The high electrochemical stability obtained with the incorporation of graphene nanosheets again verifies the strong interlayer interaction between the aromatic graphene nanosheets and the π conjugated polymer chains for enhanced charge transport within the multilayered nanostructure during electrochemical cyclic stability test. The specific capacitance obtained from the discharge slope of constant current galvanostatic technique was 165 F/g at the end of 1000 cycles at 1 A/g discharge current density.

Conclusion: Previous research employed a chemical or electro-polymerization approach to uniformly cover graphene nanosheets or carbon nanotubes with a thick polymer coating for fabrication of composite electrodes for supercapacitor applications. In this new approach aligned monolayers of graphene nanosheets are interspersed within the fibrous network of polypyrrole to function as a series of current collectors inside the multilayer bulk electrode configuration. This nanostructured electrode exhibits high ionic and electronic transport due to the combined presence of the fibrous network of polypyrrole and electrically conductive graphene nanosheets. Impedance analysis clearly shows the low equivalent series resistance obtained from the interlayer charge transport between the large graphene basal plane and the π conjugated polymer chain. The facile electronic charge transport due to the presence of graphene nanosheets also had a stabilizing affect on the electrochemical cyclic stability of this composite electrode. This multilayer film electrode displays symmetric charge-discharge characteristics and a nearly ideal rectangular cyclic voltammogram with increasing voltage scanning rate from 10 to 100 mV/sec. While maintaining a high frequency capacitative response with a knee

frequency close to 50 Hz, this nanostrctured composite electrode exhibits 165 F/g specific capacitance at 1A/g discharge current density even after 1000 electrochemical cycles.

References:

1. Allen. M. J., Tung. V. c., And Kaner. R. B., "Honeycomb carbon: A review of graphene", Chemical Review, 2010, 110, 132-145

2. Rao. C. N. R., Sood. A. K., Subrahmanyam. K. S., Govindaraj. A., "Graphene: The new two dimensional nanomaterial", Angewandte Chemie-International Edition, 2009, 48, 7752-7777

3. Geim. A. K., "Graphene: Status and prospect", Science, 2009, 324, 1530-1534

4. Fukushima. H., "Graphite Nanoreinforcements in Polymer Nanocomposites" Ph.D. Dissertation, Michigan State University, East Lansing, MI, 2003

5. Biswas. S., Drzal. L. T., Nano letters, 2009, 9, 167-172

6. Conway, B. E. "Electrochemical Supercapacitors: Scientific Fundamentals and Technological Applications" Publisher Kluwer, 1999

7. Chmiola. J., Yushin. G., Gogotsi. Y., Portet. C., Simon. P., Taberna. P. L., Science 2006, 313, 1760-1763

8. Lota. G., Centeno. T. A., Frackowiak. E., Stoeckli. F., Electrochimica Acta 2008, 53, 2210-2216

9. Wang. H. L., Hao. Q. L.,Yang. X. J., Lu. L. D., Wang. X., Electrochemistry communications, 2009, 11, 1158-1161

10. Wu. Q. F., He. K. X., Mi. H. Y., Zhang. X. G., Materials chemistry and physics, 2007, 101, 367-371

11. Zhou. C., Kumar. S., Chemistry of materials, 2005, 17, 1995-2002

12. An. K. H., Jeon. K. K., Jeong. K. H., Lim. S. C., Bae. D. J., Lee. Y. H., Journal of electrochemical society, 2002, 149, A1058-A106

13. Gupta. V., and Miuraa. N., Electrochemical and solid state letters, 2005, 8, A630-632

14. Najafabadi. A. I., Tan. D. T. H., Madden. J. D., Syntehtic metal, 2005, 152, 129-132

15. Arico. A. S., Bruce. P., Scrosati. B., Terascon. J. M., Schalkwikj. W. V., Nature materials, 2005, 4, 366-367

16. Manthiram. A., Murugan. A. V., Sarkar. A., Muraliganth. T., Energy and environmental science, 2008, 1, 621-638

17. Centi. G., Perathoner. S., European Journal Of Inorganic Chemistry, 2009, 26, 3851-3878

18. Otero. T. F., Padilla. J., Journal of Electroanalytical Chemistry, 2004, 561, 167–171

19. Oh. J., Kozlov. M. E., Kim. B. G., Kim. H. K., Baughman. R. H., Hwang. Y. H., Synthetic metals 2008, 158, 638-643

20. Zhou. C., Kumar. S., Doyle. C. D., Tour. J. M., Chemistry of materials, 2005, 17, 1997-2002

21. Zhang. X., Zhang. J., Song. W., Liu. Z., Journal Physical Chemistry B 2006, 110, 1158-1165

22. Zhang. C., Zhang. X., Zhanga. X., Ou. X., Zhang. W., Jie. J., Chang. J. C., Lee. C. S., Lee. S. T., Advanced material, 2009, 21, 4172-4175

23. Wu. T. M, Chang. H. L., Lin. Y. W., Composite science and Technology, 2009, 69, 639-644

24. Fan. J., Wan. M., Zhu. D., Chang. B., Pan. Z., Xie. S., Journal of applied polymer science, 1999, 74, 2605-2610

25. Wanekaya. A. K., Lei. Y., Bekyarova. E., Chen. W., Haddon. R., Mulchandani. A., Myung. N. V., Electroanalysis, 2006, 18, 1047-1054

26. Han. G., Yuan. J., Shi. G., Wei. F., Thin solid films, 2005, 474, 64-69

27. Wang. K. P., Teng. H., Journal of the electrochemical society, 2007, 154, A993-A998

28. Wang. K. P., Teng. H., Journal of the electrochemical society, 2008, 155, A739-A744

CHAPTER 5

EFFECT OF REDUCTION OF OXYGEN FUNCTIONAL GROUPS AT THE EDGES OF GRAPHENE NANOSHEETS ON ELECTRICAL AND CAPACITATIVE PROPERTIES

Abstract: The active edge sites of graphene nanosheets are reduced in a two-step process to reduce the atomic oxygen concentration from 9.49 to 4.78%. A combination of high temperature vacuum annealing followed by hydrogenation protects the reduced edges on the graphene basal plane from recombination with atmospheric oxygen to produce graphene nanosheets with higher thermal stability. The reduced graphene nanosheets exhibit high electrical conductivity and graphitic potential dependent capacitance properties compared to the complex potential dependence of capacitance exhibited by the unreduced nanosheets as a result of removing the redox active oxygen functional groups present at the edges. These reduced graphene nanosheets exhibits high electrochemical cyclic stability for power electrochemical energy storage applications.

Introduction: Graphene can be considered to be a polycyclic aromatic hydrocarbon [1-4]. The basal plane consists of densely packed sp^2 hybridized carbon atoms in a honeycomb lattice structure [1-4]. However, the size of the basal plane of graphite is finite and some of the carbon atoms in the highly aromatic basal plane can terminate at the edges in a non-aromatic state. The carbon atoms present at the edges are highly chemically active as compared to the chemically inert carbon atoms present in the basal plane [5,6]. During preparation of graphene nanoplatelets, the edge carbon atoms can react spontaneously to atmospheric oxygen to create carboxyl, keto, or hydroxyl group

[5-7]. An XPS analysis on natural graphite sample exhibits an oxygen atomic concentration of less than 2 atomic%. As compared to graphene produced via the highly oxidative graphite oxide route, the graphene nanosheets developed by Drzal research group in Michigan State University are prepared by acid intercalation and thermal exfoliation process [7]. This process creates graphene nanosheets with a lateral dimension ranging from 50μm to as small as 500 nm [7]. The number of edge sites is fixed for a given platelet size, as XPS elemental analysis exhibits a proportional increase in the atomic oxygen concentration with decreasing graphene nanosheets dimension. For large sized graphene nanosheets with an average lateral dimension 15 μm and surface area around 270 m^2/g the oxygen atomic concentration is less than 5%. However, for small sized graphene nanosheets with an average dimension less than 500 nm and surface area close to 550 m^2/g the oxygen atomic concentration increases to 10%. The large sized nanosheets not only offer a large highly aromatic basal plane area but also an edge area that is important in electronic transport between nanosheets in a bulk macroscopic sample.

Capacitor applications are dependent on the high electronic conductance from large aromaticity of the aromatic basal plane. However, the hydrophobicity arising from the large area aromatic basal plane often restricts the ionic accessibility of aqueous based electrolytes inside the bulk electrode. It has been demonstrated earlier that the incorporation of small sized graphene nanosheets with higher edge oxygen content provides better wettability of the electrode to facilitate ionic electrolyte transport. The increase in the specific capacitance can be attributed to increased specific surface area and the presence of oxygen functional groups at the nanoplatelet edges. The presence of

oxygen functional groups significantly enhances the specific capacitance from the change in oxidation state at different applied electrode potential [8,9]. At the same time, the changing potential can cause reversible transformation of different oxidation states of the surface functional groups to alter the potential-capacitance relation significantly [8-11]. In comparison to large aromatic basal plane area in large sized graphene nanosheets these small sized nanosheets are therefore expected to exhibit a complex potential-capacitance relation due to the highly surface active oxygen content [10-11]. The complex potential-capacitance relation also affects the performance of electrodes for electrochemical capacitor applications. The increasing edge chemical functionalities introduce a series of contact resistance over the large microscopic areas for enhanced electronic resistance to the electrode. The increasing electronic resistance causes significant voltage drop during the discharge of the capacitors at high current densities. This is also found during the cyclic voltammetry analysis with a highly oblique and narrow shaped capacitance-voltage response at high scanning rate.

Thus this study was undertaken to investigate the effect of reduction of these oxygen functional groups on the electrical and capacitative properties of graphene nanosheets. XPS has been used as an analytical tool to quantify the effect of these functional groups on the complex potential-capacitance relation for large and small sized graphene nanosheets.

Experimental details: In this study, the sample used for chemical reduction was graphene nanosheets with an average surface area 550 m^2/g. These nanosheets are termed as small sized nanosheets with an average lateral dimension less than 500 nm. The large

sized nanosheets has average dimension from 10 to 15 μm. Unless indicated about the use of large sized nanosheets, all the results mentioned here will comprise small sized graphene nanosheets. In the reduction process, first the small sized graphene nanosheets were vacuum annealed at 550 C under high vacuum (2 x 10^{-2} torr) for 30 minutes following the report by Dinger et al. [12]. The TGA analysis for both the reduced and the unreduced sample was carried out in air at 5 C/min ramping rate in air. The XPS analysis was carried out a magnesium K α X-ray source in Perkin Elmer Phi 5400 ESCA system at pressures between 10^{-9} and 10^{-8} torr with pass energy of 29.35 eV and a take-off angle of 45°. The Raman spectra analysis was carried out on a bulk sample and the laser was not focused on the basal plane area of a single nanosheet. The laser diameter used in our experiment was 10 μm, which is large enough to include the edges of 500 nm sized graphene nanosheets from the bulk sample to exhibit a pronounced disorder or defect induced 'D' band peak near 1340 cm^{-1} wavelength. The XRD measurement was carried out at room temperature in air.

Variable sized graphene nanosheets were prepared by the acid intercalation and thermal exfoliation technique as explained earlier [7]. Sodium fluoride and potassium hydroxide were purchased from Sigma-Aldrich and were used without any further purification.

The potential-capacitance analysis was carried out in a two electrode configuration with the area and loading of the active electrode materials in the counter electrode kept much higher than working electrode for the measurement. A 0.1M NaF aqueous solution was used for all the potential-capacitance analysis. For electrochemical stability analysis, the two electrode configuration was used with equivalent loading of active material on both

the electrodes. The loading of graphene nanosheets were close to 4 mg/cm^2. The surface resistance of the film was measured using a four point probe measurement from Keithley 2400 source meter.

Result and discussion: The vacuum annealed sample was XPS analyzed in two parts with the first one without any exposure to the air and the second part exposed to the air. For the unreduced sample the oxygen atomic concentration was 9.49%. After vacuum annealing treatment, when the sample was exposed to air, the oxygen atomic concentration reduced to 7.97%. However, when sample was not exposed to air, the oxygen atomic concentration was as low as 2.14%. This result clearly indicates that even after the reductive treatment the edge sites are still highly reactive to recombine with the atmospheric oxygen to raise the atomic concentration from 2.14 to 7.97%. In order to avoid the recombination of atmospheric oxygen, the sample was thus hydrogenated in the next step for 1 hour at 150 C and 1 h at 200 C. The sample was then exposed to atmosphere and the XPS measurement showed an oxygen atomic concentration of 4.78%. In comparison to the vacuum annealed air exposed sample, the decrease in the oxygen atomic concentration from 7.97 to 4.78% for the hydrogenated sample clearly demonstrates that some of the reactive edge sites are blocked by hydrogenation from the recombination with atmospheric oxygen.

Thermogravimatric analysis (TGA) shown in Figure 5.1 shows that the reduced sample displays enhanced thermal stability with more than 98% weight retention up to at least 400 C. The unreduced sample on the other hand shows a significant drop of more than 10% weight loss near 400 C. The increasing stability of the reduced sample could be

attributed to two factors. First, the vacuum annealing treatment at 550 C for 30 minutes can remove residual amorphous carbon from the sample. Second, replacing the edge oxygen content in the keto or carboxylic acid functional group from with alkane or alkene groups impart higher thermal stability without the generation of a decomposition products like CO or CO_2 [13,14].

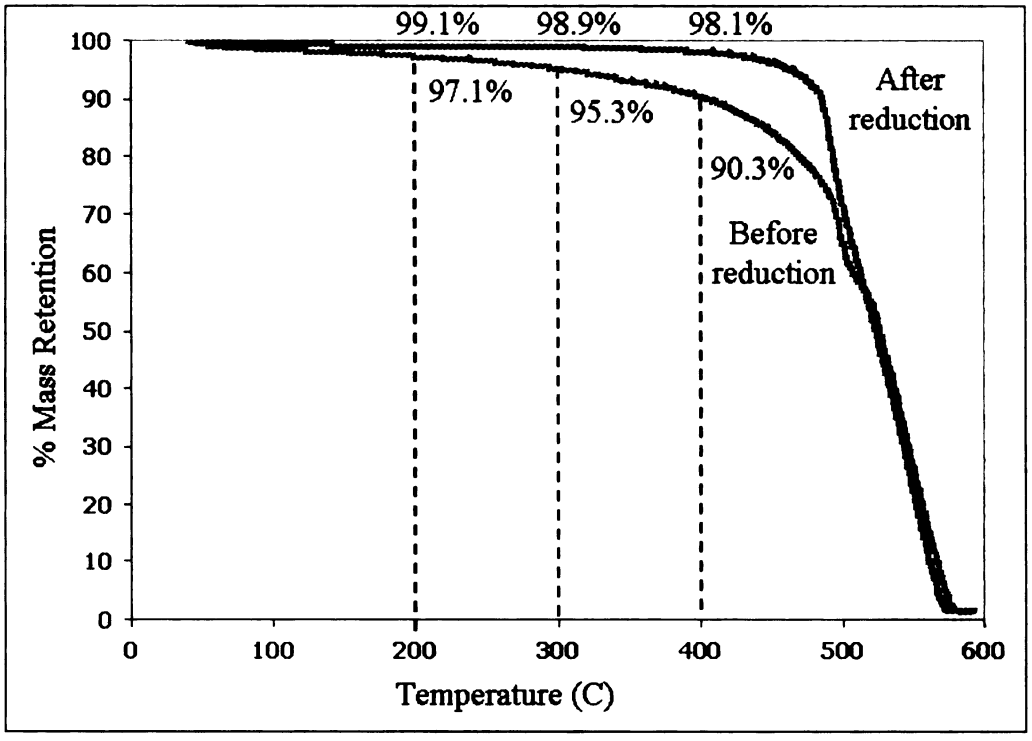

Figure 5.1: Thermogravimetric (TGA) analysis: small sized graphene nanosheets before and after reduction in air at 5 C/min temperature ramping rate

The Raman spectra analysis in Figure 5.2 of the reduced and the unreduced sample of small sized graphene nanosheets reveal that the two step reduction treatment causes no damage to the aromatic character of these nanosheets. It is well documented that the intensity ratio between the G peak to the defect or disorder oriented D peak is an indication about the aromatic purity of the graphene basal plane [15,16]. Even for pure graphitic sample, the D band is expected to be present from the termination of aromatic continuity of the basal plane by the sp^3 hybridized edge area with the presence of oxygen functional groups [15,16]. In our study, the small increase in the G band to the "defect

and disorder" D band intensity ratio for the reduced sample as compared to the unreduced sample indicates the removal of amorphous carbon during the vacuum annealing treatment. However compared to the large sized graphene nanosheets, the G to D band intensity ratio is low for the small sized graphene nanosheets even after the reductive treatment.

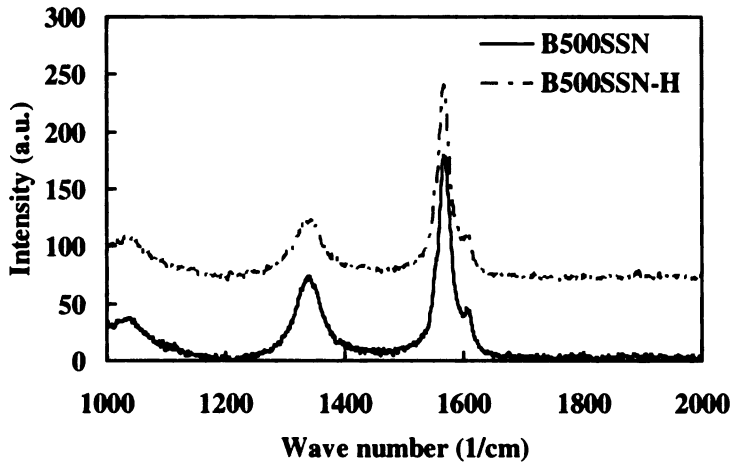

Figure 5.2: Raman spectra analysis: reduced and unreduced graphene nanosheets

The XRD spectra analysis of the reduced and the unreduced sample were inconclusive and a small intensity peak was found for both the samples near 26.2^{o}. This could be expected from the fact that only the edge oxygen groups gets chemically reduced without affecting the basal plane area of graphene nanosheets.

The XPS analysis was used to evaluate the change in the 'C-C' as well as different 'C-O' bonds from the peak analysis in the C1s spectra associated with different bonds. The C1s spectra can be fully deconvoluted into several peaks: C=C/C-C aromatic ring at 284.6 ev; the asymmetrical envelope corresponding to damaged alternate hydrocarbon

with sp^3 radical near ~285.4 ev; the carbonyl group C-O at 286.1 eV; the keto C=O at 287.5 eV; the carboxylic acid group O=C-OH at 289.2 eV; and a broad π- π^* near 290.6 to 291.4 eV [17-19]. For the small sized graphene nanosheets, the C/O atomic ratio for the unreduced sample was 12.7, which increases to 23.2 for the reduced sample indicating the reduction of various oxygen functional groups. Even though the reduction of specific oxygen functional groups to a hydrogenated carbon could not be quantified exactly, the peak intensity analysis gives a clear indication of the reduction of oxygen functional group containing carbon atoms to sp^3 and sp^2 hybridized C-H bonds. The increase in the sp^2 content of the sample with the increase in the intensity ratio of the aromatic C=C/C-C peak at 284.6 eV to the damaged alternate C-H bonded sp^3 peak near 285.5 eV for the reduced sample reveals the successful conversion of sp^3 bonded carbons to sp^2 state. This is also confirmed by the increase in the sp^2 content from the aromatic C=C/C-C peak at 284.6 eV to the peaks associated with different oxygen functional groups at 286.1, 287.5, and 289.2 eV respectively. Table 1 clearly demonstrates the XPS analysis of the concentrations of carbon atoms present in different chemistry for the unreduced and reduced small sized graphene nanosheets.

Table 5.1: Concentrations and molecular assignments of carbon atoms for the unreduced and reduced small sized graphene nanosheets

	C1S sub-peak binding energy (EV) Bond-allocated carbon concentration (ATOM %)					
	sp^2 C	sp^3 C	C-O/ C-O-C	C=O	O-C=O	π-π*
Unreduced graphene nanosheets	284.68 53.87%	285.22 32.75%	286.18 7.14%	287.68 2.01%	289.18 2.93%	290.67 1.30%
Reduced graphene nanosheets	284.74 69.63%	285.80 24.51%	286.24 1.61%	287.74 1.05%	289.24 1.05%	290.39 2.16%

The surface resistance of the thin film was measured for both the unreduced and reduced small sized graphene nanosheets with an average lateral dimension less than 500 nm. The thin film was deposited on a glass substrate by drop coating a dispersion of these small sized nanosheets in isopropanol. The sheet resistance for the unreduced film was an average 12 kOhm/sq which decreases to 7.5 kOhm/sq for the reduced film. The decrease in surface resistance with the vacuum annealing treatment is expected to result from the removal of any amorphous carbon. The chemical reduction of the oxygen functional groups, on the other hand, improves the electrical conductivity possibly from lowering of the edge to edge interparticle resistance over large macroscopic areas. However, the surface resistance of the large sized graphene nanosheets is always at least one order of magnitude lower than the small sized nanosheets indicating the importance of the large

area basal plane and the resulting minimum edge to edge contact area over large macroscopic areas for enhanced electronic conductance.

The potential dependent capacitance characteristics of the electrodes prepared from large and small sized nanosheets in the reduced and unreduced state was determined to investigate the effect of the oxygen functional groups at the edges. As shown in Figure 5.3a, for large sized graphene nanosheets the potential capacitance curve is parabolic in shape with potential minima close to the potential of zero charge (PZC). The typical potential capacitance characteristics for these large sized graphene nanosheets with a nearly linear increase on both sides of PZC is very similar to the characteristic reported earlier for the basal plane of highly oriented pyrolitic graphite [20-23]. The presence of a broad minima and the absence of sharp increase in the slope on both sides of the potential minima near the PZC can be from the result of the presence of charged impurities on the basal plane or the exposed oxygen function groups present at the edges during the electrochemical measurement [20-21, 23].

Figure 5.3: Potential-Capacitance characteristics: Capacitance measured at different applied potential in 0.1 M NaF aqueous solution for different materials a) unreduced large sized b) unreduced small sized c) reduced small sized graphene nanosheets

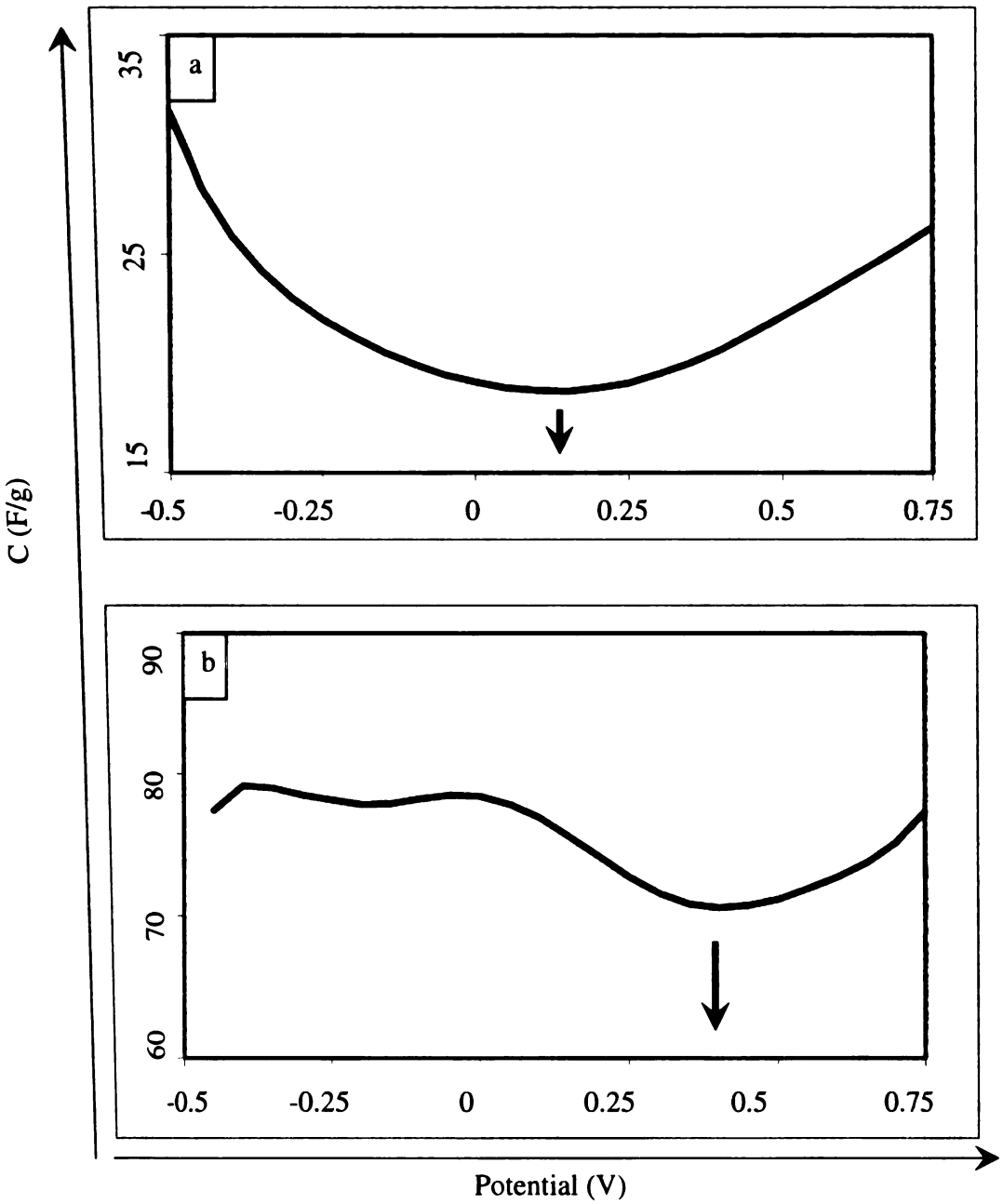

Figure 5.3 (cont.)

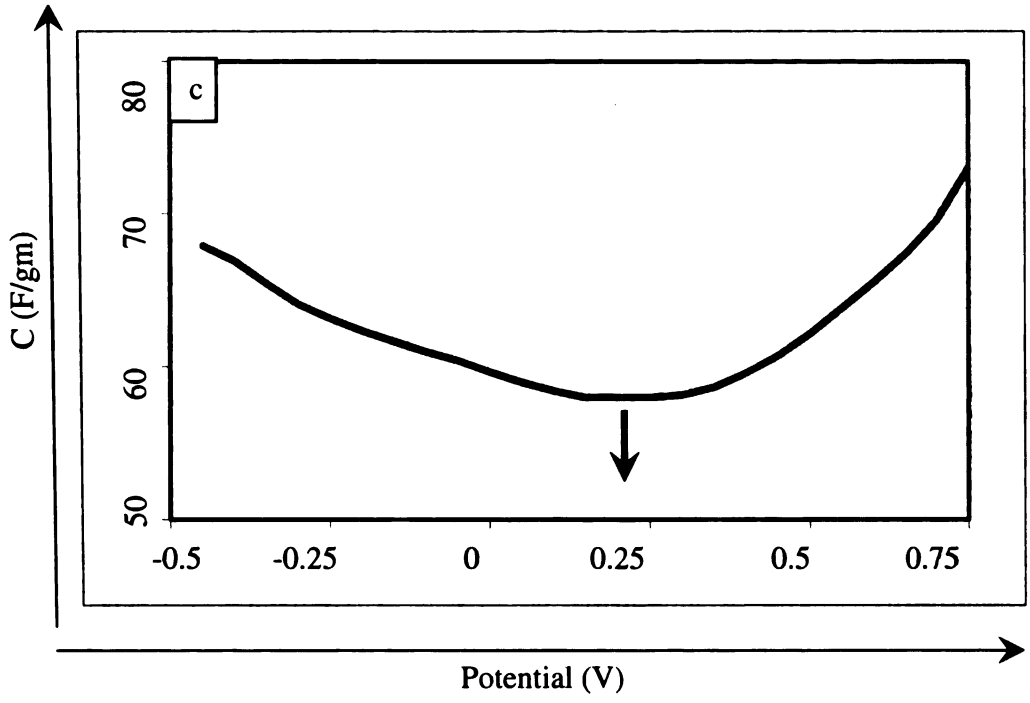

As shown in Figure 5.3b, small sized unreduced nanosheets exhibit much higher capacitance and a complex potential dependence of capacitance over the same potential range. These can be the results of the effect of increased surface area, porosity and the edge oxygen functional groups resulting from going from large to small sized nanosheets [19-23]. The oxygen functional groups contribute to the increasing capacitance from the reversible change in the oxidation-reduction state with the solvated electrolyte ions [23]. The complex potential capacitance behavior also originates from the changing oxidation state at different potentials. The occurrence of the broad and nearly flat band potential-capacitance characteristics for the unreduced nanosheets is a result of the redistribution of

charges in the presence of surface functional groups at the edges as compared to the large and inert basal plane area for the large sized graphene nanosheets [23].

After reduction the specific capacitance decreases as compared to the unreduced state. Interestingly, the complex potential capacitance relation recovers the parabolic characteristics with a broad potential minimum near the PZC as shown in Figure 5.3c. A decrease in the specific capacitance is expected from the reduced contribution to the capacitance from the reduction of oxygen functional groups [19-23]. The reductive process also leads to the recovery of parabolic shape of the response curve implying greater graphitic characteristics of the system. However, the clear shift in the potential minima away from the PZC is possibly due to the contribution of remaining surface active oxygen functional groups as was found for the large sized nanosheet.

From the above results, we concluded that the presence of oxygen functional groups at the edges of graphene nanosheets affects the potential-capacitance characteristics and the specific capacitance of the electrode. The larger the nanosheet, the higher is the graphitic character to exhibit parabolic potential-capacitance characteristics. However, with decreasing particle size active oxygen functional groups bound to the edges of graphene basal plane increase and the changing oxidation state produces a complex potential-capacitance relation. With reduction, the specific capacitance decreases and the parabolic potential-capacitance characteristics are recovered.

The electrochemical stability of the electrodes was compared in a two electrode configuration for the unreduced and the reduced small sized graphene nanosheets material. Without the addition of any binder material, the dispersion of nanosheets was stirred overnight in isoproponol and the slurry was then evenly spread on a stainless steel

current collector and dried at 80 C under vacuum to remove any remaining solvent. The electrodes were then assembled with a cellulose paper separator in a two electrode configuration which was tightened and immersed in 6M aqueous KOH solution for electrochemical characterization. The galvanostatic constant current technique was used to characterize the charge discharge characteristics of these electrodes at 1A/g discharge current density.

As shown in Figure 5.4a,b, the control sample exhibited a voltage drop (IR drop) of ~200 mV at the vertex potential during the discharge cycle. The voltage drop remained almost constant with increasing discharge cycle number from the 50^{th} to 1000^{th} cycles. As shown in Figure 5.4c,d, for the hydrogenated sample the initial voltage drop was close to 200 mV, which decreased to 75 mV with increasing cycle number from 50^{th} to 1000^{th} cycle. For the hydrogenated sample this could be explained by the nanosheet wettability. With the reduction of oxygen functional groups, the hydrophobicity of small sized graphene nanosheets increases and thereby reduces the wettability of the electrode and therefore limits the ease of aqueous electrolytic diffusion to the mesoporous network inside the bulk electrode. With increasing electrochemical cycles, the electrode wettability improves to reduce the voltage drop from 200 to 75 mV. Thus the rate capability for the hydrogenated electrode improves with increasing cycle number. The higher electrical conductivity of the hydrogenated graphene nanosheets could also be another factor for better rate capability of the electrode.

Figure 5.4: Constant current charge discharge characteristics of graphene nanosheets based electrodes at 1A/g discharge current density. (a,b) charge discharge characteristics of unreduced small sized graphene nanosheets at 50^{th} and 1000^{th} cycle, (c,d) charge discharge characteristics of reduced small sized graphene nanosheets at 50^{th} and 1000^{th} cycle

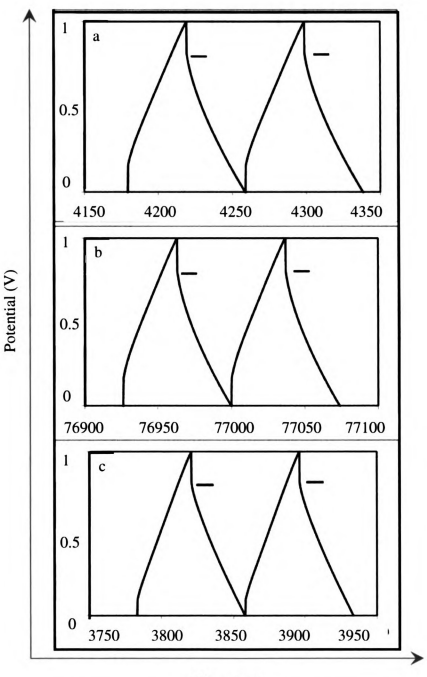

Figure 5.4 (cont.)

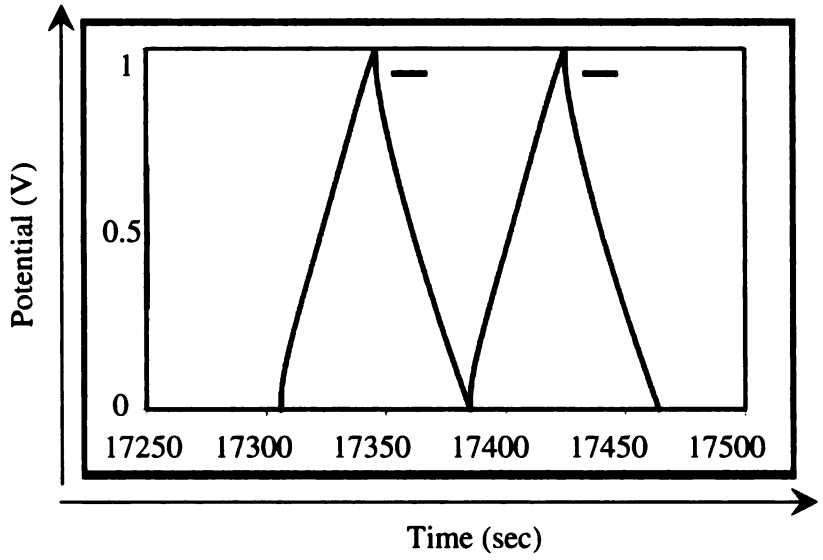

Conclusion: In summary, small sized graphene nanosheets with a high concentration of edge oxygens were vacuum annealed and hydrogenated in a two-step reduction process to reduce the atomic oxygen content from 9.49 to 4.78%. Exposure to air was found to be critical for the vacuum annealed sample as indicated by the spontaneous repopulation of the edge sites on exposure to atmospheric oxygen. Hydrogenation of the vacuum annealed sample is therefore essential to keep the active edge sites passivated and immune from recombination with atmospheric oxygen. XPS analysis clearly reveals an equivalent increase in the sp^2 content of the reduced sample from the unreduced state with the oxygen functional groups present before the two step reduction process. The hydrogenated sample is thermally stable to 400°C in air and the electrical conductivity improves by a factor of approximately 100% as a result of the reduced edge to edge interparticle resistance from the chemical reduction of oxygen functional groups. The

decrease in edge oxygen content was also evidenced by the recovery of parabolic potential-capacitance characteristics for the hydrogenated sample as compared to the unreduced sample. The unreduced sample on the other hand exhibited a complex potential capacitance relation from the reversible oxidation-reduction process associated with the oxygen functional groups present at the edges. The hydrogenated sample demonstrates better stability with increasing electrochemical cycles for high power electrochemical capacitor applications.

Acknowledgement: The collaboration of Dr. Xioabing Li for the reduction of the graphene nanoplatelets is gratefully acknowledged.

References:

1. Geim. A. K. and Novoselov. K. S., Nature Materials, 2007, 6, 183-191
2. Allen. M. J., Tung. V. c., And Kaner. R. B., Chemical Review, 2010, 110, 132-145
3. Rao. C. N. R., Sood. A. K., Subrahmanyam. K. S., Govindaraj. A., Angewandte Chemie-International Edition, 2009, 48, 7752-7777
4. Geim. A. K., Science, 2009, 324, 1530-1534
5. Warner J. H., Schffel F., Rmmeli M. H., Bernd Bchner B., Chemistry of Materials, 2009, 21, 2418–2421
6. Enoki T., Kobayashi Y., Fukui K. I., International Reviews In Physical Chemistry, 2007, 26, 609-645
7. Fukushima. H., Ph.D. Dissertation, Michigan State University, East Lansing, MI, 2003.
8. Mitra S., Sampath S., Electrochemical And Solid State Letters, 2004, 7, A264-268
9. Stoller M. D., Park S. J., Zhu Y. W., An J. H., Ruoff R. S., Nano letters, 2008, 8, 3498-3502
10. Conway, B. E. "Electrochemical Supercapacitors: Scientific Fundamentals and Technological Applications" Publisher Kluwer, 1999
11. Lota. G., Centeno. T. A., Frackowiak. E., Stoeckli. F., Electrochimica Acta, 2008, 53, 2210-2216
12. Dinger A., Lutterloh C., Biener J., Kuppers J., Surface Science, 1999, 421, 17–26
13. Dreyer D. R., Park S., Bielawski C. W., Ruoff R. S., Chemical Society Review, 2010, 39, 228-240
14. Sungjin P., Jinho A., Piner R. D., Inhwa J., Dongxing Y., Aruna. V., Nguyen S. B. T., Ruoff, R. S., Chemistry of Materials, 2008, 20, 6592-6594
15. Calizo, I.,Balandin A. A.,Bao W., Miao F., Lau C. N., Nano Letters, 2007, 7, 2645-2649
16. Kudin K. N., Ozbas B., Schniepp H. C., Prud'homme R. K., Aksay I. A., Car R., Nano letters, 2008, 8, 36-41

17. Yang D. Q., Sacher E., Langmuir, 2006, 22, 860-862

18. Filik J., May W., Pearce S. R. J., Wild R. K., Hallam K. R., Diamond and Related Materials, 2003, 12, 974-978

19. Mattevi C., Eda G., Agnoli S., Miller S., Mkhoyan A.,Celik O., Mastrogiovanni D., Granozzi G., Garfunkel E., Chhowalla M., Advanced Functional Materials, 2009, 19, 2577-2583

20. Baughman R. H., Papadimitrakopolus F., Chattopadhyay D., Wallace G. G., Barisci J. N., Journal of Electrochemical Society, 2003, 150, E409-415

21. Xia J., Chen F., Li J., Tao N., Nature Nanotechnology, 2009, 4, 505-509

22. Randin J. P., Yeager A. E., Journal of Electroanalytical Chemistry, 1972, 36, 257-276

23. Randin J. P., Yeager A. E., Electroanalytical Chemistry and Inter facial Electrochemistry, 1975, 58 313 – 322

CHAPTER 6

SELF ASSEMBLY OF HIGHLY HYDROPHILIC NANOSHEETS OF MANGANESE DIOXIDE AT THE LIQUID-LIQUID INTERFACE FOR ELECTROCHEMICAL ENERGY STORAGE APPLICATIONS

Abstract: Ultrathin film of birnessite type layered manganese dioxide was prepared by directing the transport of MnO_2 nanosheets from the bulk phase to the liquid-liquid interface by reducing the surface charge density and the surface energy of these MnO_2 nanosheets. This was achieved by lowering the pH of the stable aqueous colloidal dispersion of the MnO_2 nanosheets in the presence of another immiscible organic phase such as hexane. The ultrathin film developed on the water surface was then transferred onto a desired substrate in a single or multilayer configuration. The electrochemical properties of this multilayer film were then investigated in combination with highly electrically conductive graphene nanosheets for electrochemical supercapacitor applications.

Introduction: Thin films of manganese dioxide MnO_2 is useful in multiple applications in catalysis, photocatalysis, ion exchange and others [1-4]. There is a considerable interest growing in the field of electrochemical energy storage applications applying nanolayered films of MnO_2 for supercapacitors or battery applications [4-7]. In these applications, the formation of thin films of nanoparticles is the key to produced devices with high energy and power densities. Self assembly of nanoparticles at the liquid-liquid interface is one versatile way to create ordered monolayer on a desired substrate [8,9]. It

has been demonstrated that an ordered array of hydrophobic or uncharged particles can be formed at the liquid-liquid or at the air-water interface [8-13]. For hydrophobic particles the three phase contact angle at the liquid-liquid interface approaches near 90^{o} and the particles are adsorbed at the interface as a result of a substantial gain in interfacial energy [12]. For hydrophilic particles, however, the situation is different since the particles are completely wet by water to produce a highly dispersed stable colloidal suspension. It has been reported earlier that charged gold nano particles with an average diameter 10 to 100 nm can be trapped in an ordered monolayer at the liquid-liquid interface by the addition of ethanol in the aqueous phase [9]. The interaction of ethanol with the charged gold nano crystals causes a decrease in the surface energy and drives the particles from the bulk phase to the liquid-liquid interface to form an ordered array. A similar phenomenon was observed with the addition of alkanethiols on a stable colloidal suspension of charged gold nanoparticles in the presence of an immiscible hexane phase [13]. Park et al. successfully prepared hexagonally close packed monolayer films of metal nanoparticles by using long-chain alkanethiols [13]. The long-chain alkanethiols uniformly coat the charged metal nanoparticles not only to reduce the surface energy but also to induce a strong van der Waal's force of attraction between the charged metal nanoparticles [13]. In addition to the surface chemistry of the nanoparticles, the gain in interfacial energy with the adsorption of nanoparticles at the liquid-liquid interface is also a function of the nanoparticle dimension [14]. In comparison to the spherical nanoparticles, the adsorption of one dimensional tubular nanotubes or two dimensional planar nanosheets at the liquid-liquid interface results in a much higher gain in interfacial energy as a result of their large aspect ratios as compared to spherical nanoparticles [14].

Therefore the particle dimensions as well as the surface charge of nanoparticles direct the transport of nanoparticles from the bulk phase towards the liquid-liquid interface to form an ordered particle array. This research is directed at investigating the adsorption of the birnessite type two dimensional manganese dioxide nanosheets at the liquid-liquid interface from a stable colloidal suspension in water to create an ordered nanolayered film for electrochemical capacitors applications.

Experimental details: Manganese Chloride $MnCl_2$. $4H_2O$, Ethylenediaminetetraacetate (EDTA), Sodium hydroxide, and sodium sulfate were purchased from sigma Aldrich and were used without any further purification. Graphene nanosheets were prepared by following the method described elsewhere [12].

Preparation of manganese dioxide nanosheets: The process was followed from the description given elsewhere [15]. 20 mM of EDTA and 20 mM of $MnCl_2.4H_2O$ were stirred until the the Manganese chloride was completely dissolved. An equal volume 200 mM of NaOH was then added and the mixture was kept in a glass bottle at room temperature for 4 days without any stirring. The deep brown color precipitate was separated by centrifugation and washed thoroughly with water to remove any excess EDTA or NaOH.

Preparation of ultrathin film of manganese dioxide nanosheets at the liquid-liquid interface: 100 mg of manganese dioxide nanosheets were dispersed in 100 ml of water by sonicating the mixture for 5 minutes in a 150 ml beaker. The pH of this colloidal suspension was adjusted either by adding hydrochloric or nitric acid. To create a two phase system with hexane, a small volume was spread on the water surface after the pH

of the colloidal suspension was adjusted to less than 2. The two phase mixture was then briefly sonicated to create a large interfacial area between these two phases to accelerate the adsorption of nanosheets at the liquid-liquid interface. The film formed at the interface was then transferred onto a clean glass substrate for further characterization. The multilayer film was developed from repeated transfer of layers from the water surface onto the glass substrates.

Electrochemical characterization: The multilayer film of graphene nanosheets and manganese dioxide was prepared by following the same technique as was mentioned earlier for graphene nanosheets and polypyrrole composite electrode. 1M aqueous sodium sulfate solution was used as electrolyte in all the electrochemical measurements. A three electrode cell with a Ag/AgCl reference electrode was used for all the measurements.

Results and discussions: The two dimensional MnO_2 nanosheets were synthesized in the presence of a chelating agent ethylenediaminetetraacetate (EDTA) by following the method of Yuya et al. [13]. In this technique, the divalent manganese chloride is oxidized to MnO_2 in the presence of sodium hydroxide and EDTA. The chelating agent EDTA interacts with the divalent manganese cation and leads to the deposition of birnessite type nanosheets with an average thicknesses of less than 7 nm from an aqueous solution. The process and the mechanism were discussed in details by the Yuya et al. [15]. The nanosheets, precipitating out of the aqueous suspension were washed out thoroughly to remove the remaining sodium hydroxide and EDTA prior to further experiments.

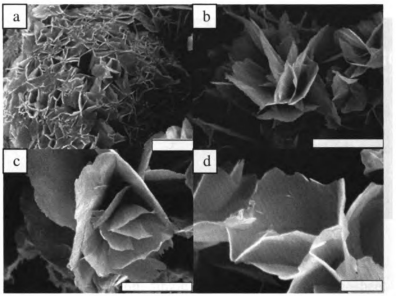

Figure 6.1: FESEM morphological characterization: MnO_2 nanosheets at different magnifications, scale bars a,b,c – 5 μm, d - 1 μm

The morphology of nanosheets is shown by the FESEM images in Figure 6.1. The nanosheets are flat with an average dimension of 1 μm and larger. The crystallinity of these nanosheets is evident from the selected area electron diffraction pattern by the TEM characterization in Figure 6.2 with approximate lattice spacing of 0.267 and 0.138 nm for (100) and (110) planes of birnessite [15].

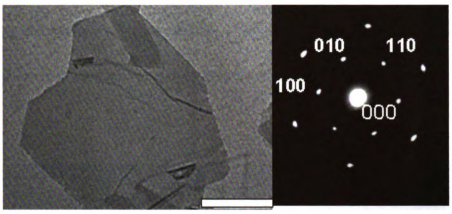

Figure 6.2: **TEM characterization**: single Manganese dioxide nanosheet with a lateral dimension close to 1μm, scale bar 500 nm, the single area diffraction in figure 2b is used to calculate the crystallographic parameters

A colloidal dispersion of these nanosheets can be easily prepared by sonicating the nanosheets in water. As shown in Figure 6.3a, depending on the concentration, the dispersion is light brown to yellow in color and highly stable for days without any visible deposition. The stability of this dispersion is evidenced by the high negative zeta potential value of -30.55mV. The pH of this colloidal dispersion was then reduced from 7 to less than 2 by the addition of nitric or hydrochloric acid. An increase in the zeta potential value was observed with decreasing pH. The increase in zeta potential is the result of the reduction of surface charge of MnO_2 with continuous protonation from the addition of acids. At pH 1.6 the zeta potential was a positive 4.3 mV and particle agglomeration was observed with increasing settling from solution with time. Figure 6.3 b-f clearly exhibits increasing agglomeration and deposition of particles at different time

intervals. The agglomeration and deposition of the MnO_2 particles could be attributed to the decreasing electrostatic repulsion between charged MnO_2 nanosheets and increasing van der Waals force of interaction between protonated nanosheets with decreasing pH.

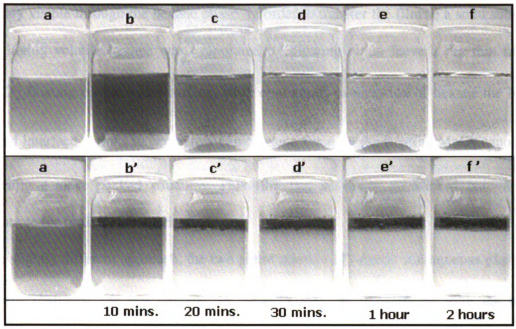

Figure 6.3: **Stability of colloidal dispersion of Manganese dioxide nanosheets and adsorption at the liquid-liquid interface** – figure 6.3a shows a stable colloidal dispersion at pH 7, figure 3 b-f represents the state of the colloidal dispersion at pH~2 at different time intervals, figure 6.3 b'-f' represents the continuous adsorption of nanosheets from the bulk phase to the water hexane interface at different time intervals, instead of settling out of the dispersion as was found with the presence of hexane from figure 6.3 b-f, the nanosheets are clearly adsorbed at the liquid-liquid interface in the presence of immiscible hexane phase

In order to understand the behavior of these protonated nanosheets in the presence another immiscible liquid phase, hexane was spread on the water surface to create a thin film. In a process complete distinct from the earlier observation at pH less than 2 and in the presence of another immiscible phase, the MnO_2 nanosheets started forming a layer at the liquid-liquid interface. As shown in Figure 6.4, the metallic sheen of the film is clearly visible through the hexane phase. In order to transfer the film to a solid substrate, the highly volatile hexane was evaporated by blowing air to leave a dry thin film of MnO_2 floating on the water surface. With continuous evaporation of hexane the liquid-liquid interface shrinks to generate a compression force on the floating MnO_2 nanosheets forming a close packed structure. This film can be easily transferred onto a glass substrate for further characterization.

In a slightly different approach, the two phase mixture of organic and aqueous phase was briefly sonicated for few minutes to create a two phase emulsion with the MnO_2 nanosheets completely adsorbed at the interface. The two phase emulsified mixture was then placed inside a closed glass bottle to prevent hexane loss. A layer of agglomerated nanosheets were observed to form at the liquid-liquid interface with time. Figure 6.3 b'-f' clearly shows the accumulation of nanosheets at the liquid-liquid interface at increasing time intervals. The aqueous portion almost became colorless after 2 hr. These demonstrate that under the presence of a second immiscible liquid phase it is energetically more favorable for the nanosheets to be adsorbed at the liquid-liquid interface rather than settling out from the suspension.

Figure 6.4: **Adsorption of Manganese dioxide at the liquid-liquid interface** – The nanosheets got adsorbed at the water-hexane interface to create a dry thin film with metallic shine from continuous evaporation of hexane

Compared to an electrical double layer charge storage mechanism, the electrochemical characteristics of MnO_2 nanosheets are dominated by the faradic charge transfer process across the electrode electrolyte interface [16,18]. The capacitance obtained from this faradic charge transfer process is known as pseudocapacitance [4-7, 16-18]. Two mechanisms have been proposed involving the inter conversion of (+III) and (+IV) oxidation states of MnO_2 nanosheets to describe the pseudocapacitative characteristics [19,20]. Either of these mechanisms considers the intercalation or surface adsorption of proton or alkali metal cations during reduction and the de-intercalation or desorption during the oxidation [19].

$MnO_2 + H^+ + e^- = MnOOH$ or $MnO_2 + C^+ + e^- = MnOOC$ .....(I)

$MnO_2|_{surface} + C^+ + e^- = MnO_2^-C^+|_{surface}$.....(II)

The birnessite type layered MnO_2 is unique as the interlayer spacing of 0.7 nm offers the maximum free space as compared to any other crystallographic forms of MnO_2 for easy access of hydrated alkali metal cations during the electrochemical oxidation or reduction process [21]. However, the poor electrical property of these nanosheets often requires the addition of electrically conductive additive materials such as carbon nanotubes or graphene nanosheets for enhanced electrochemical performance [22-26]. The electrochemical characteristics of multilayer thin films of manganese dioxide were characterized by constructing a multilayer electrode using graphene nanosheets as the conducting element. It is interesting to note here that the both graphene as well as manganese dioxide are planar in shape and therefore a maximum constant area between these two nanosheets could be expected for facile charge transfer during the electrochemical process. The multilayered composite film between these two materials was prepared by following the same approach as reported earlier for graphene nanosheets and polypyrrole to form multilayer electrodes.

A three electrode cell having an electrode of manganese dioxide and graphene nanosheets was characterized with cyclic voltammetry and constant current charge-discharge at 1A/g.

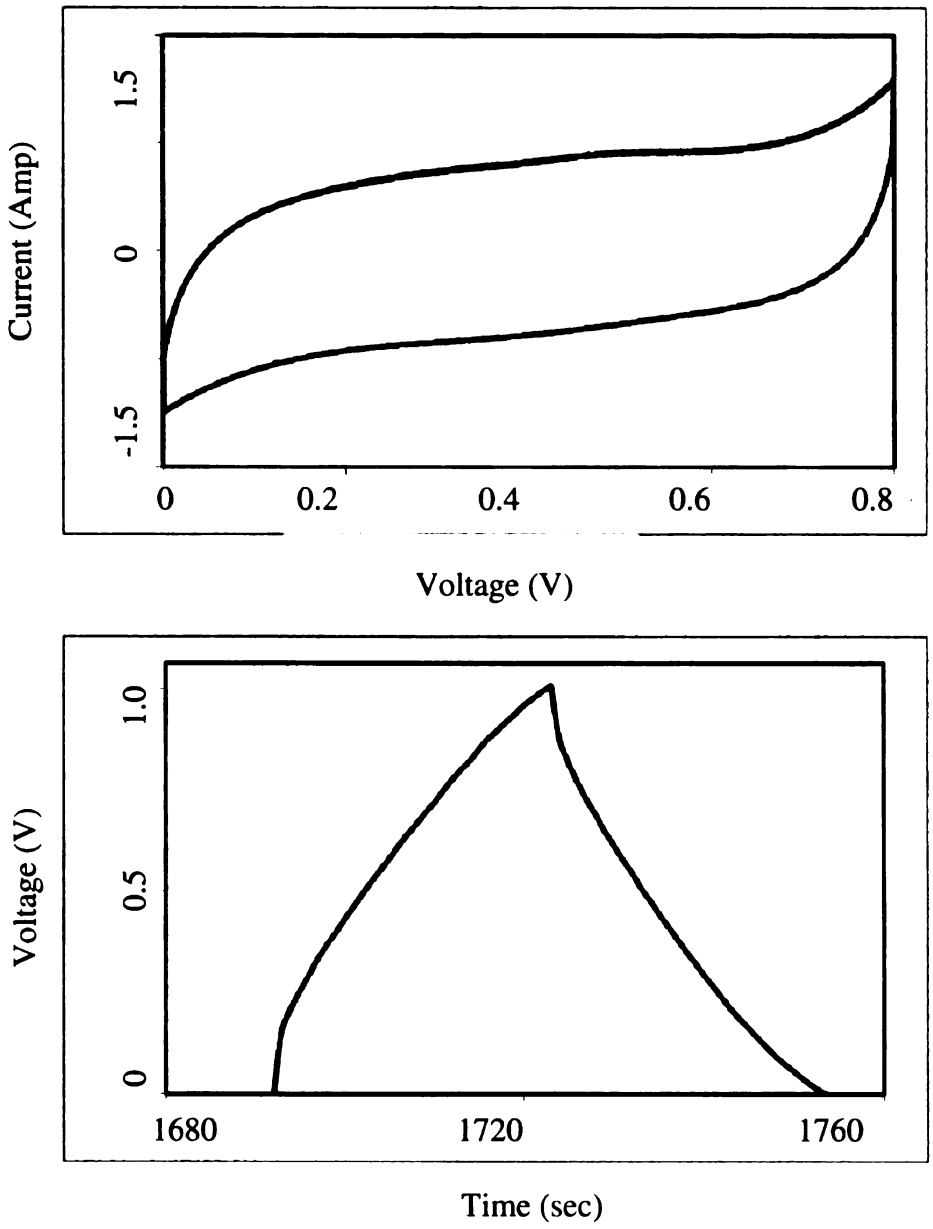

Figure 6.5: **Electrochemical characterization of Manganese dioxide and graphene nanosheets composite films** – Figure 6.5a represents the cyclic voltammogram characteristics of the composite film at 50 mV/sec voltage scanning rate, Figure 6.5b represents of the constant current charge discharge characteristics at 1A/g discharge current density

Figure 6.5 displays the cyclic voltammetry characteristics of this multilayer thin film electrode in 1 M Na_2SO_4 aqueous solution. The well developed symmetrical rectangular shaped cyclic voltammogram clearly exhibits the suitability of this material and the thin film electrode for electrochemical capacitors applications. This symmetrical CV shape was maintained at increasing voltage scanning rate from 5 to 50 mV/sec. However, at higher scanning rates, deviation from the rectangular characteristics was observed which could be due to polarization resistance [27]. The constant current chronopotentiometry measurement also exhibits highly symmetric charge discharge characteristics as shown in Figure 6.5. The minimum voltage drop during the reverse scanning at the peak potential demonstrates the high electrolytic as well as electronic conductivity from the presence of large gallery spacing of manganese dioxide and electrically conductive graphene nanosheets. The average specific capacitance for this composite electrode was close to 210 F/g. A complete analysis on the impedance characteristics and the cyclic stability at different discharge current densities will be forthcoming in a future study of this composite electrode.

Conclusion: In summary, the adsorption of birnessite type MnO_2 nanosheets at the liquid-liquid interface was investigated. It was found that reducing the surface charge by protonation at low pH causes agglomeration and deposition of these MnO_2 nanosheets from a stable aqueous dispersion. Measurement of the zeta potential also showed a change from a high negative value for the stable aqueous dispersion to a slightly positive value at low pH. The addition of a second immiscible phase causes the MnO_2 nanosheets

to migrate from the bulk phase to the liquid-liquid interface and deposit as an ultrathin film which can be subsequently transferred to a glass or other substrate. With the continuous evaporation of hexane from the top surface, the shrinking area of the liquid-liquid interface generates a compressive force on the floating nanosheets to create a compact array of the MnO_2 nanosheets on the water surface. This liquid-liquid interfacial approach can be used to develop a multilayer assembly of MnO_2 nanosheets for electrochemical capacitors applications. The composite electrodes prepared from the layered graphene nanosheets and manganese dioxide exhibit a high gravimetric capacity density along with highly symmetric charge discharge characteristics which are attractive for high energy electrochemical capacitor applications.

References:

1. Shen Y.-F.; Zerger, R. P.; DeGuzman, R. N.; Suib, S. L.; McCurdy, L.; Potter, D. I.; O'Young, C. L. Science 1993, 260, 511

2. Lianzhou Wang L., Omomo Y., Sakai N., Fukuda K., Nakai I., Ebina Y., Takada K., Watanabe M., Sasaki, T., Chemistry of Materials, 2003, 15, 2873-2878

3. Brock S. L., Sanabria M., Nair J., Suib S. L., Ressler T. J., Phys. Chem. B 2001, 105, 5404

4. Rao, C. N. R., Cheetham, A. K., Mahesh, R., Chemistry of Materials 1996, 8, 2241

5. Ni J. P., Lu W. C., Zhang L. M., Yue B. H., Shang X. F., Lv Y., Journal of Physical Chemistry C, 2009, 113, 54-60

6. Xu C. J., Li B. H., Du H. D., Kang F. Y., Zeng Y. Q., Journal of Power Sorces, 2008, 184, 691-694

7. Athouel L., Moser F., Dugas R., Crosnier O., Belanger D., Brousse T., Journal of Physical Chemistry C, 2008, 112, 7270-7277

8. Binder W. H., Angew. Chem. Int. Ed. 2005, 44, 5172 – 5175

9. Reincke F., Hickey S. G., Kegel W. K., Van maekelbergh D., Angew. Chem. Int. Ed. 2004, 43, 458-462

10. Sasaki T., Iyi N., Geng F., Ozawa T. C., Ma R., Hu L., Chemical Communication, 2008, 4897–4899

11. Lee K. Y., Han S. W., Bull. Korean Chem. Soc. 2005, Vol. 26, 1306-1309

12. Biswas S., Drzal L. T., Nano Letters, 2009, 9, 167-172

13. Park Y. K., Park S., Chemsitry of Materials, 2008, 20, 2388–2393

14. Binks B. P., Colloidal Particle at Liquid Interfaces; Cambridge University Press, New York, 2006

15. Oaki. Y., Imai H., Angewandte Chemie International Edition 2007, 46, 4951 – 4955

16. Jiang R. R., Huang T., Liu J. L., Zhuang J. H., Yu A. S., Electrochimica Acta, 2009, 54, 3047-3052

17. Chang J. K., Hsu S. H., Tsai W. T., Sun I. W., Journal of Power Sources, 2008, 177, 676-680

18. Nam K. W., Kim K. B., Journal of Electrochemical Society, 2006, 153, A81-A88

19. Toupin M., Brousse T., Be´langer D., Chemistry of Material 2004, 16, 3184-3190

20. Chun S. E., Pyun S. I., Lee G. J., Electrochimica Acta, 2006, 28, 6479-6486

21. Ghodbane O., Pascal J. L., Favier F., ACS Applied Materials & Interfaces, 2009, 1, 1130-1139

22. Raymundo-Pinero E., Khomenko V., Frackowiak E., Beguin F., Journal of Electrochemical Society, 2005, 152, A229-A235

23. Xie X. F., Gao L., Carbon, 2007, 45, 2365-2373

24. Ma S. B., Nam K. W., Yoon W. S., Yang X. Q., Ahn K. Y., Oh K. H., Kim K. B., Journal of Power Sources, 2008, 178, 483-489

25. Bordjiba T., Belanger D., Journal of Electrochemical Society, 2009, 156, A378-A384

26. Zhang M., Wang M., Qie Z., Wei T., Fan Z., Yan J., Materials Science and Engineering: B, 2008, 25, 174-178

27. Conway, B. E. "Electrochemical Supercapacitors: Scientific Fundamentals and Technological Applications" Publisher Kluwer, 1999

CHAPTER 7

ASSEMBLY OF THIN FILMS OF GRAPHENE NANOSHEETS BY INTERFACIAL FORCED CONVECTION

Abstract: Thin films consisting of electrically conductive graphene nanosheets or carbon nanotubes were prepared in a single step using convective self assembly coupled with electrostatic interaction between the carbon nanomaterials and a polyelectrolyte coated glass substrate. A small amount of a graphene nanosheets or carbon nanotube water suspension is placed between two glass slides to allow continuous evaporation of the water from the three phase contact line. The resulting capillary pressure forces the charged particles from the bulk suspension to be deposited on oppositely charged glass substrates resulting in a well packed and ordered array of particles. This simple and quick technique can be used to create a thin film of graphene nanosheets or other carbon based nanoparticles (e.g. carbon nanotubes) with an average surface resistance 3.5 and 2.6 kOhm/sq respectively.

Introduction: The layer by layer electrostatic self assembly technique is a versatile process to create ultra thin to multilayer film of nanoparticles on large area substrates with the aid of charged polymer species [1-7]. The traditional sequential dipping process to create dense and compact ultra thin films of nanoparticles requires long processing time as a result of the sequential deposition of oppositely charged species in a multi step technique [1-7]. Continuous growth of ordered and compact monolayers to multilayer films of fine particles on a smooth solid substrate can also be achieved via this process of convective transport of particles [8-13]. In this technique, a wettable plate is placed in

contact with a water suspension of fine particles. As shown in Figure 7.1, continuous evaporation of the water from the three phase contact line at the plate-suspension-air drives the particles to the meniscus edge resulting in continuous growth of a particle array [8-13]. Increasing capillary pressure from the increasing curvature of the menisci between the particles with continuous evaporation of water generates a pressure difference with respect to the hydrostatic pressure to produce a flux of water and particles towards the meniscus edge [8-13]. As the substrate is uniformly pulled from the stable suspension of particles in water, a particle array on a smooth solid substrate is produced by this convective evaporation technique.

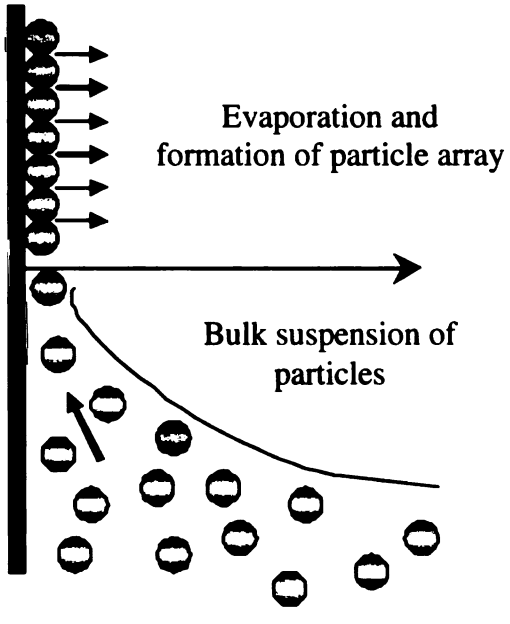

Figure 7.1: **Particle array formation** - Mechanism of ordered array of particle formation on the solid substrate from continuous evaporation of water from the three phase contact line [19]

Hydrophobic carbon nanomaterials such as carbon nanotubes or graphene nanosheets are difficult to disperse in water [14]. Charged polymer species such as sodium polystyrene sulfonate (SPS) are often used to create a stable suspension of these hydrophobic nanomaterials in water [15-18]. Layer by layer electrostatic self assembly of negatively charged SPS coated carbon nanotubes and positively charged polyelectrolyte such as poly(diallyldimethylammonium chloride) PDAC can be used to develop an electrically conductive network of carbon nanotube on a glass substrate using this sequential multilayer deposition approach [18]. However, a forced convection of charged particles towards the oppositely charged species on a solid substrate can create a well packed monolayer to multilayer structure in a single step by taking advantage of convective transport of particles from the bulk suspension towards the three phase contact line with continuous evaporation of water. This single step technique can be used to create a well packed assembly of carbon nanotubes or graphene nanosheets for electrically conductive coating applications.

Experimental details: Multiwalled carbon nanotube was kindly provided Nanocyl S.A. Belgium. The exfoliated graphene nanosheets were prepared by acid intercalation of natural graphite followed by thermal exfoliation [20]. Exfoliated graphite nanosheets used in this experiment have a lateral dimension 1 μm with an average thickness 5 to 10 nm. Poly(diallyldimethylammonium chloride) (PDAC, Mw~70,000), sulfonated poly(styrene), sodium salt (SPS, Mw~150,000) were purchased from Sigma Aldrich.

SPS coated graphene nanosheets or carbon nanotubes were prepared by mixing 0.1 gm of nanotubes or nanosheets in 0.01 M SPS and 0.01 M NaCl in 100 ml volume. The mixture was sonicated for 30 mins and then was stirred overnight (Virsonic 100, SP Industries Inc, Warminster, PA). The dispersion was filtered, washed and re dispersed back in 100 ml solution before the final use. During the re dispersion process, an additional sonication of 5 minutes was applied..

Substrate preparation: The microscopic glass substrates were cleaned by Alconox (Alconox Inc., New York, NY) detergent in a water bath sonicator for 20 mins. The slides were then washed in distilled water by batch solication for 10 mins and finally dried in a nitrogen stream. Oxygen plasma treatment was carried out in by Harrick Plasma chamber (Harrick Scientific Corporation, Broadway Ossining, New York) for 10 min at a pressure of 125 mTorr. The oxygen plasma treated glass slides were immediately immersed in 0.01 M PDAC in 0.1 M NaCl solution for 20 mins.

Characterization: Surface resistance of the film was measured by using 4 point probe technique by 2400 source meter from Kiethley Instruments. SEM characterization was done on JOEL 6400V microscope.

Result and discussion: To produce a stable dispersion of these hydrophobic nanomaterials, both carbon nanotubes and graphene nanosheets were individually dispersed in water in the presence of negatively charged polymer sulfonated polystyrene (SPS) [15-18]. While the aromatic moiety of SPS interacts strongly with the aromatic basal plane of the carbon nanotube or graphene nanosheet, it is the repulsion between the charged sulfonated tails that prevents the agglomeration of these hydrophobic species in

water. The suspension was filtered and thoroughly washed with plenty of water to remove any excess amount of polyelectrolyte present in the system. After washing, the material was re-dispersed in water to produce a stable dispersion of SPS wrapped carbon nanotubes or graphene nanosheets. However, a stable dispersion could not be obtained for graphene nanosheets with a lateral dimension of more than 5 μm. The strong hydrophobic interaction between the graphene basal surfaces coupled with gravitational settling of large nanosheets is responsible for increasing aggregation of the large graphene nanosheets observed with time. These results are limited to graphene nanosheets with an average lateral dimension of less than1 μm.

Similar to layer by layer approach, a clean glass substrate is first oxygen plasma treated to introduce negative charges on the surface [15-18]. The negatively charged surface is then coated with positively charged polymer PDAC by dip coating the substrate in a 10 mM solution of PDAC in water. The substrate is then thoroughly washed to remove any loosely bound PDAC on the glass surface. In order to utilize the mechanism of forced convection of negatively charged SPS coated carbon nanotubes or graphene nanosheet towards the positively charged glass surface, the substrate is immersed in a water suspension of carbon nanotube or graphene nanosheets in a beaker to allow the evaporation of water from the three phase contact line as shown in Figure 7.1. The time necessary to produce the film varies with the volume of water to be evaporated. Large volumes of suspensions require long process times and also lead to very thick coatings of particles. A small volume of liquid suspension, therefore, not only reduces the processing time but also insures better control over the thickness of the depositing layers.

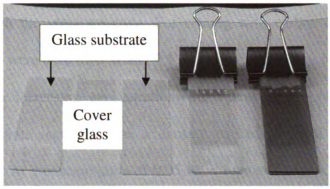

Figure 7.2: **Assembly of device** - Two glass substrates are shown in the above figure with a microscopic cover glass of average thickness 150 μm in between. A binder clip is used to attach these glass substrates with the microscopic cover glass in between at the top. The small separation between these two glass slides creates a strong capillary force when few liquid droplets are placed at the bottom to fill up the entire space with the liquid suspension as shown above

To minimize the liquid suspension volume, two glass substrates separated by a microscope cover glass of 150 μm thickness were attached to each other separated by a binder clip at the top as show in Figure 7.2. For a glass substrate dimension of 3 x 1 inch, this small separation distance can hold a liquid volume as small as 200 μL. In order to fill the empty space between the glass substrates, liquid suspension droplets were placed at the bottom of the assembled device to generate a strong capillary force to suck the liquid up and fill up the entire volume between the two glass substrates. The assembly is then placed inside a dehumidifier (Relative humidity 25%) at an approximate angle of 20^{0} with the bottom substrate coated with positively charged polymer PDAC. At this condition, the small volume of water evaporates to create an ordered array of particles deposited on the solid substrate.

Figure 7.3 shows the FESEM image of network of carbon nanotubes and graphene nanosheets deposited on the glass substrate. For coating with carbon nanotubes two different concentrations were used 0.05 M and 0.1 M in water. From the FESEM images it is evident that with increasing concentration, the extent of coverage by carbon nanotubes on the substrate increases with a densely packed structure obtained at a concentration of 0.1 M. At a concentration of 0.05 M in Figure 7.3 (a,b), the nanotubes are well dispersed with minimum aggregation over a large macroscopic area. At 0.1 M concentration in Figure 7.3 (c,d), the overlap and entanglements between nanotubes increases to produce a thicker and dense coating on the substrate. For graphene nanosheets with a concentration of 0.1 M, the formation of dense and compact layer of nanosheet on the surface is evident from the FESEM micrograph in Figure 7.3 (e,f).

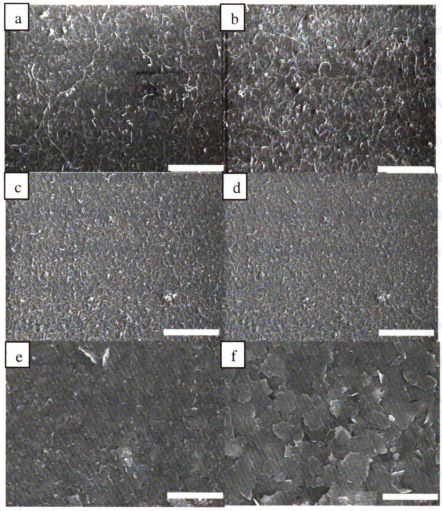

Figure 7.3: **Coating of carbon nanomaterials on glass substrates** – (a,b) carbon nanotube film prepared on a glass substrate from 0.05 M suspension concentration. (c,d) carbon nanotube film prepared from 0.1 M suspension concentration . (e,f) a well packed coating of graphene nanosheets of average dimension less than 1 μm on the glass substrate, the concentration of graphene nanosheets in the suspension was 0.1 M. Scale bar from figure 7.3 (a-e) 2 μm and for figure 7.3 f 1μm

In this technique with a small volume of liquid trapped between two glass substrates, the evaporation process to remove the entire volume of liquid in less than 2 hours of time. At

the same time, changing the concentration of liquid suspension allows better control over the thickness of the depositing layer on the solid substrate. Once the space between the glass substrates is filled with the liquid suspension of carbon nanotubes or graphene nanosheets, water evaporates continuously from the three phase contact line. At this condition, under the action of the strong capillary force, convective transport drives the suspended particles towards the meniscus edge. Once at the meniscus edge, the negatively charged SPS coated nanoparticles interact strongly with the positively charged PDAC coated glass substrate to create an ordered and compact array of particles on the solid substrate as evidenced by the FESEM characterization.

It has been well documented that monolayer to multilayer deposition could be possible from convective self assembly of particles by adjusting the meniscus withdrawal rate with respect to the crystal growth or particle array formation rate on a solid substrate [8-13, 19]. The particle volume fraction and the solvent evaporation rate determine the fixed velocity at which the meniscus must be withdrawn in order to achieve monolayer deposition of particles [8,19]. However, in this research the meniscus withdrawal is not controlled by any mechanical device rather it is the evaporation of water at a nearly constant humidity that brings the liquid suspension level down with continuous withdrawal of meniscus in a direction opposite to the particle array formation on the glass substrate. As the FESEM images show, randomly scattered aggregated domains of particles are not observed at the different concentrations and the constant humidity level maintained during the film formation indicating that the meniscus withdrawal rate is either close to or lower than the rate of particle array formation [8,19].

Besides the low meniscus withdrawal rate, the formation of multilayers of the deposited particles is also dependent on obtaining a uniform mono dispersion of these hydrophobic carbon nanotubes and graphene nanosheets in water. Another important factor is the strong van der Waals force of attraction between the particles when their concentration increases near the meniscus edge from the continuous convective flow of the particles from the bulk suspension [8,19]. However, the convective transport of particles insures a compact and dense particle array in a single step to exhibit good electrical conductivity.

The surface resistances of these thin films of carbon nanotube and graphene nanosheets were measured by four point probe technique. For the carbon nanotube film prepared from concentrations 0.05 M, 0.1 M the respective surface resistances were 3.5 kOhm/sq and 5.2 kOhm/sq. For graphene nanosheets at a concentration of 0.1 M the average surface resistance was 2.6 kOhm/sq. The decrease in surface resistance with increasing carbon nanotube concentration confirms the formation of denser and highly packed network of carbon nanotubes on the glass substrates. For graphene nanosheets, the low surface resistance obtained at 0.1 M concentration clearly indicates the formation of compact layer in a single step technique without requiring multistep process such as layer by layer approach to achieve electrically conductive network.

Conclusion: A convective self assembly approach was applied to create ultrathin films of carbon nanomaterials such as carbon nanotubes or graphene nanosheets on glass substrates. In comparison to the layer by layer electrostatic self assembly, in this technique two oppositely charged species such as the positively charged PDAC and

negatively charged SPS coated carbon nanomaterials are assembled as a result of forced convection from the continuous evaporation of water at the three phase contact line between plate-suspension-air. A strong capillary force generates the transport of the particles from the bulk suspension to create an ordered and compact particle array for electrically conductive coating on glass substrate. A simple device consisting of two microscopic glass slides separated by a distance of only 150 μm to hold liquid volume as small as 200 μL was used to validate this approach. In this single step technique, with this small volume of liquid suspension the process time can be minimized and thin films of carbon nanomaterials can be deposited depending on the particle concentration in the bulk suspension.

References:

1. Schonhoff. M., Current Opinion In Colloid & Interface Science, 2003, 8, 86-95

2. Kovtyukhova. N. I., Ollivier. P. J., Martin. B. R., Mallouk. T. E., Chizhik. S. A., Buzaneva. E. V., Gorchinskiy. A. D., Chemistry of Materials, 1999, 11, 771-778

3. Kim. B., Sigmund. W. M., Langmuir, 2004, 20, 8239-8242

4. Paloniemi. H., Lukkarinen. M., Aaritalo. T., Areva. S., Leiro. J., Heinonen. M., Haapakka. K., Lukkari. J., Langmuir, 2006, 22, 74-83

5. Kim. B. S., Kim. B., Suh. K. D., Journal of Nanoscience and Nanotechnology, 2008, 8, 3895-3899

6. Yan. X. B., Chen. X. J., Tay. B. K., Khor. K. A., Electrochemistry Communications, 2007, 9, 1269-1275

7. Kim. B. S., Kim. B., Suh. K. D., Journal of Polymer Science Part A-Polymer Chemistry, 2008, 46, 1058-1065

8. Prevo. B. G., Velev. O. D., Langmuir, 2004, 20, 2099-2107

9. Prevo. B. G., Kuncicky. D. M., Velev. O. D., Colloids And Surfaces A-Physicochemical And Engineering Aspects, 2007, 311, 2-10

10. Cha. N. G., Echegoyen. Y., Kim T. H., Park. J. G., Busnaina. A. A., Langmuir, 2009, 25, 11375- 11382

11. Canpean. V., Astilean. S., Petrisor. T., Gabor. M., Ciascai. I., Materials letters, 2009, 63, 1834-1836

12. Chang. S. T., Velev. O. D., Langmuir, 2006, 22, 1459-1468

13. Zhang. J., Alsayed. A., Lin. K. H., Sanyal. S., Zhang. F., Pao. W. J., Balagurusamy. V. S. K., Heiney. P. A., Yodh. A. G., Applied Physics Letter, 2002, 17, 3176-3178

14. Biswas. S., Drzal. L.T., Nano Letters, 2009, 9, 167-172

15. Artyukhin. A. B., Bakajin. O., Stroeve. P., Noy. A., Langmuir, 2004, 20, 1442-1448

16. Paloniemi H., Lukkarinen M., Aaritalo T., Areva S., Leiro J., Heinonen M., Haapakka K., Lukkari J., Langmuir, 2006,22 74-83

17. Xue W., Cui T. H., Nanotechnology, 2007, 18, 145709

18. Shim. B. S., Tang. Z., Morabito. M. P., Agarwal. A., Haiping Hong. H., Kotov. N. A., Chemistry of Materials, 2007, 19, 5467-5474

19. Dimitrov. A. .S, Nagayama. K., Langmuir, 1996, 12, 1303-1311

20. Fukushima H. Graphite nanoreinforcements in polymer nanocomposites. PhD Thesis, Michigan State University, East Lansing, MI, USA, 2003

CHAPTER 8

SUMMARY AND CONCLUSIONS

In summary, it has been found that controlling the physicochemical properties of graphene nanosheets is essential to process and fabricate devices for successful technological applications. Exfoliated graphene nanosheets prepared by Drzal research group in Michigan State University are unique and can be assembled into nanosheets of diverse physicochemical properties. While the large sized nanosheets are highly aromatic and offer exceptionally low electrical resistivity, the small sized nanosheets on the other hand contain multiple oxygen functional groups at the edges but since their edge to surface ratio is smaller, they offer better solution processability and better aqueous ionic accessibility than the large sized nanosheets for electrochemical energy storage applications.

As a result of their high degree of aromaticity, the large sized graphene nanosheets offer minimum interparticle resistance over large macroscopic areas. However the high degree of hydrophobicity limits processing of these nanomaterials in the most common solvent, water. By taking advantage of highly hydrophobic nature of the graphene nanosheets, a new process was developed to self assemble them at the hydrophobic liquid - hydrophilic liquid interface into a close packed monolayer. Driven by the minimization of interfacial energy these planar shaped graphene nanosheets produce a closed packed monolayer structure at the liquid-liquid interface without agglomeration and restacking. As a result the native properties of graphene are preserved without requiring any chemical transformation of the graphene basal plane. The large microscopic size of the graphene

nanosheets that comprise the film reduces the contact resistance over the large macroscopic area of the film. The resulting graphene nanosheet monolayer film is highly compact, optically transparent from the visible to the infra red region and electrically conductive.

The strong aromatic character of the graphene nanosheet monolayer film prepared in this way causes a large inter planar interaction from the capillary force and drying induced collapse of monolayers of graphene nanosheets into a flexible and 100% binder free multilayer, free standing film. For carbon nanomaterial based electrodes for electrochemical energy storage applications, the high electrical conductivity and the high specific surface area are prerequisites to achieve minimum electronic resistance and high specific capacitance. The large sized graphene nanosheets used this study has an average surface area of 270 m^2/g and the electrical conductivity of the multilayer film is an average of 1.25×10^4 S/m. The multilayer film electrode prepared from these large sized graphene nanosheets exhibits an average gravimetric specific capacitance of 36 F/g with an exceptionally low equivalent series resistance (ESR) to discharge the accumulated power in less than 50 milliseconds for high power electrochemical capacitor application. The specific capacitance of the electrode was improved by using small sized graphene nanosheets with high surface area and increased edge oxygen functionalities as compared to large sized nanosheets. While the presence of these oxygen functionalities enhances the wettability of the electrode and facilitates aqueous ionic diffusion within the bulk electrode, the decreasing particle size on the other hand significantly contributes towards the larger electronic resistivity from increasing inter particle contact resistances. In order to minimize the electrical resistance associated with the small sized graphene nanosheets,

the large and small sized nanosheets were combined in a bulk supercapacitor electrode architecture consisting of a highly aligned network of monolayers large sized nanosheets as a series of current collectors within a multilayer configuration of bulk electrode. This nano-architecture exhibits a high frequency capacitative response and a nearly rectangular cyclic voltammogram at 1000 mV/sec scanning rate, possesses a rapid current response, small equivalent series resistance (ESR) and fast ionic diffusion for high power electrical double layer capacitor (EDLC) application. The gravimetric capacitance increased to 80 F/g with a time constant less than 700 millisecond for high power supercapacitor applications.

An investigation into the effect of reduction of edge oxygen functional groups on the electrical and capacitative properties of small sized graphene based electrodes revealed that the electrical conductivity improves by at least 50% from reduced edge to edge interparticle resistance from the chemical reduction of oxygen functional groups. The specific capacitance on the other hand decreases from the reduced contribution of the pseudocapacitative effect of oxygen functional groups after reduction. The decrease in edge oxygen content was also evidenced by the recovery of parabolic potential-capacitance characteristics for the hydrogenated sample as compared to the unreduced sample. The reduction of the edge functionalities also resulted in better stability of the electrode with increasing electrochemical cycles for high power electrochemical capacitor applications.

This multilayer configuration of highly electrically conductive large sized graphene nanosheets was combined with other functional nanomaterials such as conductive polymers and metal oxide nanosheets to achieve higher gravimetric capacitance while

keeping minimum electronic resistivity. The multilayer combination of conductive polymer polypyrrole nanowire and large sized graphene nanosheets resulted in high electrochemical cyclic stability from enhanced interlayer charge transport between the large graphene basal plane and the π conjugated polymer chain of polypyrrole. Maintaining a high frequency capacitative response with a knee frequency close to 50 Hz this composite nano architecture exhibits ~165 F/g specific capacitance at 1A/g discharge current density at the end of 1000 electrochemical cycles. A similar improvement was observed with the incorporation of manganese dioxide nanosheets in the multilayered nanoarchitecture of large sized graphene nanosheets to achieve a gravimetric capacitance of more than 200 F/g.

A summary of results of graphene nanosheets based electrodes is shown in table 8.1

Table 8.1: Electrochemical properties of graphene nanosheets based electrodes

Active electrode materials	Capacitance (F/g)	Electrode contact resistance (mohm)	Time constant (msec)
Large sized graphene nanosheets	36 F/g at 50 A/g discharge current density	30	<50
Aligned composite of large and small sized graphene nanosheets	80 F/gm at 10 A/gm discharge current density	30	633
Aligned composite of Polypyrrole nanowire and large sized graphene nanosheets	165 F/g at 1 A/gm discharge current density	150	1584

As a result of these investigations, it has been shown that the combination of diverse physical and chemical aspects of graphene nanosheets such as particle size surface area and edge chemistry in an ordered and highly aligned nanoarchitecture is essential for different technological applications. These inexpensive graphene nanosheets used in this research and the ease of the process to produce the aligned nanostructure make this new material and method highly advantageous for optoelectronics to electrochemical energy storage applications.

Future investigations and opportunities: In this study the formation of edge shared network of highly aromatic graphene nanosheets monolayer presents a unique opportunity to investigate how the electronic charge transport between two highly aromatic graphene nanosheets is affected by the presence of oxygen functional groups at the edges. Quantitative identification of the chemical functional groups and the measurement of their effect on the electronic transport at the edge to edge junction between nanosheets over large macroscopic areas can provide guidance to manipulate the electrical properties of graphene nanosheets from the two step reduction process we described in the study to achieve desirable properties for diverse electronics applications. This investigation can also be extended to find the effect of other chemical functional groups such as nitrogen based amine or amide groups on the electronic transport between two highly aromatic graphene nanosheets at their edges.

For electrochemical energy storage applications, the future challenge for applying graphene nanosheets is achieving high energy density to match the performance of lithium ion batteries. The energy density of graphene nanosheets based electrodes are

limited by participation of only a few number of conduction band electrons to form the electrical double layer as compared to large number of valence electrons involved in the charge transfer mechanism for batteries. The energy density for graphene based supercapacitor electrodes can be improved from the incorporation of metal oxide nanoparticles. The participation of reversible faradic charge transfer process across the electrode-electrolyte interface for the metal oxide nanoparticles can enhance the energy density. However, in spite of achieving high specific capacitance or energy density, poor electrical conductivity of metal oxides nanoparticles often restricts these materials from exhibiting rapid charge-discharge characteristics for high power applications. Therefore an optimized combination of metal oxide nanoparticles and graphene nanosheets can not only achieve a high energy density to match the performance of batteries but also to achieve rapid charge discharge characteristics from the presence of highly electrically conductive graphene nanosheets. However, the challenge remains to investigate and understand of the mechanism of electronic charge transport between these two distinct nanomaterials to achieve high power characteristics. In this regard, the deposition of metal oxide nanoparticles on the monolayer of large sized graphene nanosheets could be useful to understand the mechanism of charge transport to the graphene basal plane from a detail analysis of scanning tunneling or conductive probe atomic force microscopic measurements. Once the effect of different particle dimensions, crystallographic nature and orientations of metal oxide nanoparticles on the facile electronic charge transport to the graphene basal plane is understood, aligned nano architectures between these elements can be easily optimized to fabricate new supercapacitor electrodes that can challenge the performance of batteries.

APPENDIX

ELECTRICAL AND MECHANICAL PROPERTY ENHANCEMENT IN EXFOLIATED GRAPHENE NANOPLATELET/LIQUID CRYSTALLINE POLYMER NANOCOMPOSITES

Abstract: A liquid crystalline polymer (LCP) poly(benzoyl-1,4-phenylene)-co-(1,3-phenylene)], nanocomposite was prepared with exfoliated graphene nanoplatelets (xGnP) to achieve both high mechanical modulus and electrical conductivity. The fabrication technique and the dispersion of nanoplatelets have been shown to be critical to achieve high mechanical modulus at low filler loading. A loading of only 1 vol% of the xGnP particles improved the modulus of the LCP nanocomposite by 25% and 55% at a loading of 5vol%. The electrical conductivity the non-conductive LCP improved to a very high value of $4.5x10^{4}$ S/cm with the addition of 5 vol% of xGnP nanoparticles.

Introduction: Dispersion of carbon nano-materials inside polymer matrices has been the subject of intensive research during the last decade. The tremendous potential of expanded graphite nanoplatelets (xGnP) as nano-fillers inside the polymer matrices has generated much interest among researchers. xGnP has unique mechanical and electrical properties [1-4]. The theoretical elastic modulus of a single graphene sheet is over 1 TPa and the Young modulus is about 1060 MPa [1-4]. It has excellent electrical properties with a surface conductivity $50x10^{-6}$ ohm.cm [1-4]. xGnP can be produced in any platelet morphology with a thickness of about 5nm and with different diameters, e.g., xGnP-1 and xGnP-15, which correspond to sizes of 1 and 15 micron diameter particles respectively [1,5,6]. Depending on the properties of the filler materials, the nanoscale interaction of

the filler with the host material can improve both the mechanical and electrical properties of nanocomposites. Since xGnP has an excellent combination of mechanical, thermal and electrical properties similar to carbon nanotubes, if it can be effectively dispersed inside the host polymer matrix, the properties of the resulting nanocomposite could be greatly improved over the bulk matrix.

The major factor to achieve better dispersion is to negate the strong van der Waals force of attraction between the nanoplatelets by selecting a suitable dispersing medium. As compared to spherical or tubular shaped nanoparticles, xGnP is planar and the interaction potential between two nanoplatelets varies with the separation distance as d^2 [7]. Depending on the solvent media, the interaction between these nanoplatelets could either increase or decrease. For polymer nanocomposites, when the attractive interaction dominates, a high degree of platelet agglomeration takes place inside xGnP/polymer composites. For carbon nanomaterials based nanocomposites, homogeneous dispersion and strong interfacial interaction between the graphene basal plane and the polymer matrices are essential to achieve the desired nanocomposite properties. The dispersion and interfacial adhesion depends on physicochemical properties of the polymer matrices and xGnP, the fabrication technique and the processing conditions during the fabrication.

Liquid crystalline polymers (LCPs) were first produced in 1970 [8]. These polymers have unique properties in that the orientational ordering of the polymer chains in the melt phase distinguishes it from the isotropic phase at high temperature [8,9]. The ordering of the liquid crystalline phase is a molecular scale phenomena and this ordering can be either temperature or concentration directed [8,9]. A thermotropic phase occurs at a certain temperature range, whereas the lyotropic phase depends on the range of

concentrations of polymer in the solvent [8,9]. Thermotropic liquid crystalline polymers show two different phases: nematic and smectic [8,9]. In the smectic phase, the molecules tend to align themselves in layers and planes. In the nematic phase, molecules have no positional order, but they point in the same direction [8,9]. The alignment of LCP molecules is crucial to its mechanical and electrical properties [10,11]. Several processes leading to controllable alignment have been described. For example, it was reported that for a dip coated LCP film, the molecules tend to align in the direction of withdrawal from the polymer solution [10,11]. A mechanical process called buffing is another process through which polymer chains in smectic and nematic phases can be homogeneously aligned in the direction of the shear in the solid state [9,10,11]. This process is similar to the cold drawing of the bulk polymer samples, and it is believed that alignment is caused by the application of light shear force on the LCP film. During the buffing process, the polymer gets trapped between a moving and a stationary phase; the movable source exerts a shear force on the polymer molecules, causing those to align in the direction of the shear force [10,11].

LCP are also known to have the highest moduli of polymers in general. Because of the high ordering between LCP polymer chains it is of interest to determine if the graphene nanoplatelets would be dispersed into the LCP and cause the mechanical properties and electrical conductivity to be improved. The dispersion of large sized xGnP-15 inside a liquid crystalline polymer matrix, where the intrapolymer forces are large, is the objective of this study.

Experimental details:

Materials: Liquid crystal polymer [poly(benzoyl-1,4-phenylene)-co-(1,3-phenylene)], Parmax, was obtained from MISSISSIPPI POLYMER TECHNOLOGIES, INC., Mississippi, USA. Parmax has extraordinary high mechanical strength, stiffness and high temperature stability. Tensile strength of this polymer is around 207 MPa, whereas its tensile modulus is 6 GPa. Exfoliated graphite nanoplatelets were prepared from thermal exfoliation of acid-intercalated graphite following the method described elsewhere [1]. Chloroform was purchased from Sigma Aldrich and was used without any further purification.

Nanocomposite fabrication:

a) Solution casting and compression molding: A solution casting method was used to prepare a film of the xGnP-15/Parmax nanocomposite. Approximately one gram of the polymer powder was first dissolved in chloroform by sonicating the mixture for 1 hr at a constant power output of 50 Watt by a half inch sonicator. The polymer gets completely dissolved in chloroform as evidenced by a light yellow colored solution. xGnP-15 of specified amount was added to this solution and further sonicated for 1 hr to insure efficient dispersion of xGnP-15 in the solution. Thin nanocomposites films were obtained by placing a few drops of Parmax/xGnP-15 dispersions in chloroform inside silicone molds, and allowing complete evaporation of the solvent. These nanocomposite films were then compression molded at 2000 psi and at 275 C, corresponding to the smectic phase of this liquid crystalline polymer.

b) Doctor blade method: In the second fabricating approach, a doctor blade was used to prepare the nanocomposite film to investigate the effect of light shear force on the alignment of liquid crystalline film in the presence of xGnP-15. This method was used to apply a controlled shear on the xGnP-15 and LCP molecules to align them in a particular direction. In a typical experiment, Parmax powder was first dissolved in chloroform and xGnP-15 was then dispersed in the solution. A few drops of the dispersion were placed on a glass slide and light shear force was applied by a doctor blade to get a thin nanocomposite film. A number of such films were made to build up the desired thickness and then compression molded at a temperature, corresponding to the smectic phase of LCP.

Methods: a) Thermal analysis: differential scanning calorimetry (DSC) - Thermal transitions in Parmax was investigated using a 2920 Modulated DSC (TA Instruments). The runs were performed under nitrogen flow, after calibrating the DSC instrument using an Indium standard. For each run, a fresh sample (5-10 mg) was used at a heating rate of 5 C/min.

b) Thermo-mechanical analysis: dynamic mechanical analysis (DMA) - The storage moduli of Parmax and Parmax/xGnP-15 composites were evaluated using a 2980 Dynamic Mechanical Analyzer (TA Instruments, New Castle, DE). The reported values are for storage modulus at room temperature, and represent the average of three measurements per xGnP-15 concentration in the Parmax.

c) Field emission scanning electron microscopy (FESEM) - The morphology of the nanocomposite film was determined by using a JEOL 6300F field emission scanning electron microscope.

d) Electrical impedance - Two point probe Femtostat was used for electrical impedance measurement from Gamry Instruments.

Results and discussion: Morphological characterization of xGnP: SEM was used to characterize the exfoliated graphene nanoplatelets, as well as the dispersion of xGnP-15 in the Parmax matrix. The platelets were first dispersed in chloroform by sonication and few drops were dried on a cellulose acetate filter membrane for FESEM characterization. The FESEM image of xGnP-15 is shown in Figure 9.1a. The thinness of the platelet is evidenced by the translucent image on the cellulose acetate filter paper membrane. The average platelet size is around 10 to 15 μm. xGnP-1 particle is shown Figure 9.1b. The average particle dimension is close to 1 μm.

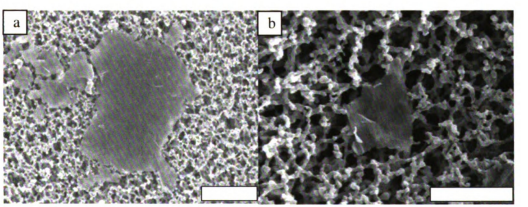

Figure A.1: **Morphological characterization of exfoliated graphene nanoplatelets** a) xGnP-15 b) xGnP-1, scale bar 5 μm and 500 nm respectively

Thermal characterization: The phase transition behavior of Parmax powder at different temperatures is shown by differential scanning calorimetry (DSC) results in Figure 9.2.

Figure A.2: **Differential scanning calorimetry analysis (DSC)** – a) Parmax control powder at different temperature dependent phase transitions for: 1. glass transition peak, 2. melting transition to a smectic phase, 3. smectic to nematic transition b) Powder sample after heat treated to 275 C c) Powder sample after heat treated to 330 C

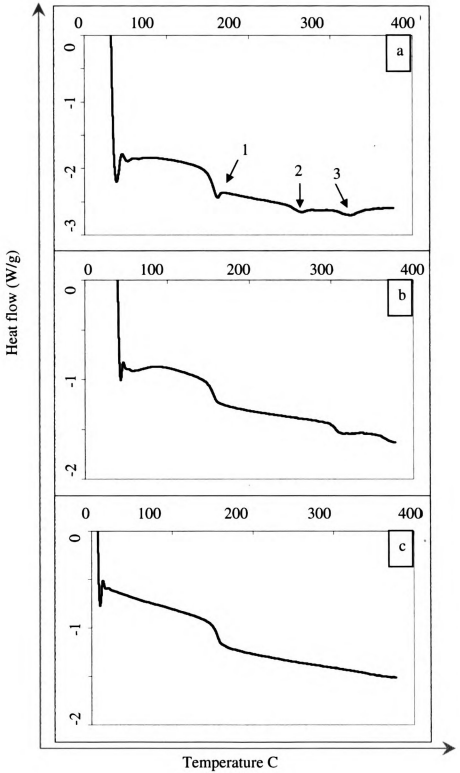
Heat flow (W/g)
Temperature C
a
b
c
1
2
3
0
100
200
300
400
-1
-2
-3

The first peak near 159 C corresponds to the glass transition peak and it appears that the second peak, at 270 C corresponds to a melting transition to a smectic phase and the third transition, at 325 C is likely to be the smectic to nematic transition. To have a better insight of the processing temperature during the composite fabrication, the control powder sample was heated at two different temperatures corresponding to the nematic and smectic phases at 275 C and 330 C respectively. The sample was heated during the thermal analysis to the desired temperature at 5 C/min and then it was cooled down also at 5 C/min to the room temperature before starting the second heating cycle. As shown in Figure 9.2b the DSC analysis on the heat treated sample from the smectic phase of the polymer, closely resembles the liquid crystalline characteristics of the control polymer powder sample with a well-defined peak corresponding to the melting to the smectic phase transition. However, when the control sample was heat treated to the nematic phase of the polymer, a deviation was observed from the liquid crystalline characteristics as it is evident from Figure 9.2c that no observable peaks corresponding to any of the phase transitions were found in the thermal analysis curve. Thus the processing temperature for the composite fabrication during the compression molding process was restricted to 275 C corresponding to the smectic phase of the polymer.

Two different fabrication techniques were used for Parmax/xGnP composite fabrication; the solution casting method and the doctor blade technique as described earlier. Large sized xGnP-15 at different concentrations was used to investigate the effect of particle alignment on the nanocomposite mechanical properties. Thin films of nanocomposites prepared by both these techniques were compression molded at 275 C and the storage modulus of the resulting sample was measured by DMA. At low loading the modulus of

nanocomposite film prepared from the doctor blade technique exhibited better mechanical modulus than the film prepared by the solution casting method. For the control sample the average mechanical modulus was 6 GPa. With 1 vol% addition of xGnP-15, the sample prepared from the doctor blade technique showed an average 25% increment (7.5 GPa) in mechanical modulus compared to 16% increment (6.9 GPa) for the sample prepared from solution casting technique only. However at higher loading of 5 vol% of xGnP-15, the increment in mechanical modulus was equivalent and it was 55% (9.4 GPa) compared to the control Parmax sample. The enhanced mechanical properties from the doctor blade processed sample at low loading is possibly due to better dispersion and alignment of large sized xGnP-15 with the liquid crystalline polymer chains within the bulk polymer matrix than the sample prepared from the solution casting technique only. It is possible that the light shear force applied during the fabrication of the film made with the doctor blade technique causes the polymer chains and the xGnP particles to align and distribute homogeneously for better mechanical properties. At higher loading however, the number density of particles within a specific volume increases to create a very large interfacial area along with a very small distance between nanoparticles. Such packing of xGnP with the polymer matrix can improve the load transfer to achieve the maximum interfacial area with the polymer matrix for better load transfer under applied stress. At lower loadings the load transfer between polymer chains may be weaker.

The morphology of xGnP-15 within the bulk matrix was compared for both of these samples and the SEM characterization in Figure 9.3 b-d demonstrates randomly oriented high particle concentration at 5 vol% of filler loading. The sample with 1 vol% loading of xGnp-15 prepared by the doctor blade technique was polished for better understanding of

particle alignment within the bulk polymer matrix. Figure 9.3 e,f clearly exhibits the highly dispersed and aligned network of xGnP-15 within the bulk polymer matrix.

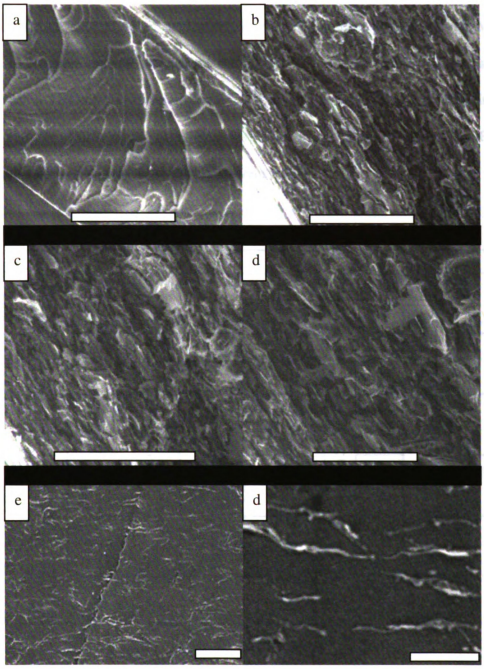

Figure A.3: **Dispersion of xGnP-15 inside the polymer matrix**: a) control polymer sample b, c, d) dispersion of 5 vol% of xGnP-15 inside the polymer matrix e,d) dispersion of 1 vol% of xGnP-15 inside the polymer matrix, the sample is polished to expose the edges of these platelets as white lines in the image

The effect of filler particle size on the mechanical properties of the nanocomposite was also compared with xGnP-15 and xGnP-1 with the samples prepared from the doctor blade technique. Figure 9.4 compares the mechanical modulus of sample prepared with xGnP-15 and xGnP-1 at different loadings. The difference in mechanical modulus at a fixed particle volume fraction is evident for different particle dimension of xGnP and the modulus obtained with xGnP-15 is higher than xGnP-1.

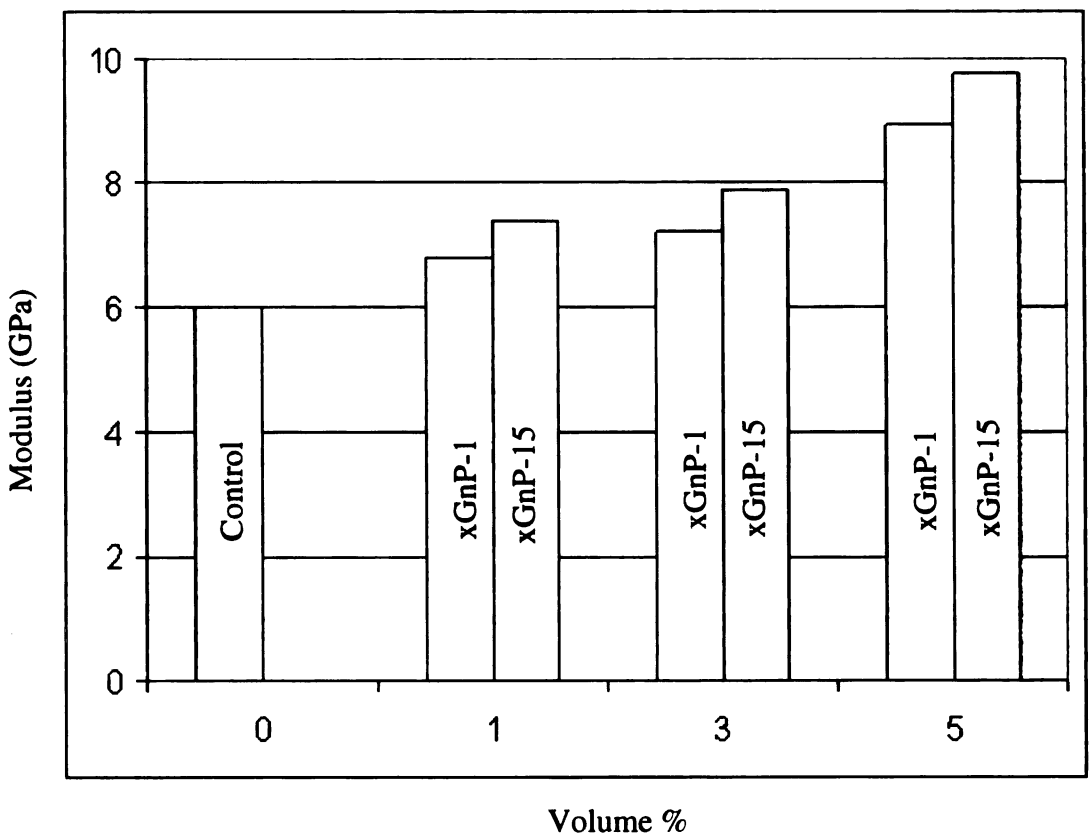

Figure A.4: Mechanical modulus of xGnP particles of various sizes at different filler loading level

This finding is surprising considering the earlier reports where higher mechanical modulus was obtained with smaller xGnP particle size [2,4]. On reducing the particle dimension, the particle number density within the bulk matrix increases to improve the mechanical modulus from enhanced particle distribution within the bulk matrix. In epoxy and vinyl ester matrix systems, the large sized xGnP-15 particles were not as effective as the smaller xGnP-1 particles. Aggregation and agglomeration of large sized xGnP-15 is another possible reason for reduced mechanical modulus as compared to xGnP-1. Parmax LCP is highly aromatic and it would be expected to interact strongly with the xGnP basal plane through pi-pi interactions. [2,4]. It is possible that this high degree of aromaticity of parmax coupled to the high chain stiffness and smectic morphology helps to disperse the larger sized xGnP particles better. The aromaticity of xGnP also depends on the particle dimension. While the basal plane area is highly aromatic, the active edge area is populated with oxygen functional groups. Reducing the particle size increases the edge to basal plane area. XPS analysis reveals an oxygen atomic concentration for the large sized xGnP particle close to 5% which increases to more than 9% for small sized nanosheets. It is possible that with aromatic polymer parmax, large sized xGnP particle disperses much better inside the polymer matrix than small sized particles of higher oxygen content. Thus the better dispersion and distribution cause enhanced modulus for nanocomposites prepared from large sized xGnP than small sized ones. The high degree of crystallinity of Parmax could be another reason for the difference in modulus for xGnP-1 and xGnP-15 nanocomposies. Other studies have shown that the xGnP basal plane is an excellent nucleator for semicrystalline polymers such as polypropylene and nylon [12]. Crystallization temperature increases of as high as 20 C has been measured and

spehreulitic crystallkite reduction of greater than 10X have also been measured in these systems [12]. The crystallization of this LCP polymer chain from the melt phase might cause the concentration and aggregation of small sized xGnP particles to the outside of the crystalline regions whereas the large size particles are too large to be displaced by the process of crystallization to cause any degree of concentration and agglomeration. The highly dispersed network of large sized xGnP-15 in Figure 9.3 d,e supports this hypothesis.

The highly aromatic graphene basal plane has a very high intrinsic electrical conductivity and imparts high electrical conductivity to these xGnP-LCP nanocomposites. The percolation of the nanoplatelets within the bulk polymer matrix is the key factor to achieving high electrical conductivity at low concentration. Parmax is electrically insulating, however, with the addition of xGnP the electrical conductivity improves to $4.5x10^{-4}$ S/cm at 5 vol% loading of xGnP-15. A marked improvement in conductivity to $6.8x\ 10^{-6}$ S/cm was measured at 3 vol% addition of xGnP-15. Based on the particle diameter of xGnP-15, the percolation point has been estimated to be at about to 3 vol%. This loading level for xGnP-15 could be the optimum to create an interconnected network of particles within the bulk matrix to reach the percolation threshold.

Conclusion: A homogeneous dispersion and alignment of xGnP particles within the bulk LCP polymer matrix is essential to achieving enhanced mechanical and electrical performance. The highly aromatic liquid crystalline polymer used in this study is significantly responsible for the high degree of interaction between it and the basal plane of the xGnP nanoparticle resulting in very good dispersion of the large sized xGnP-15

within the LCP matrix. The different fabrication techniques such as solution casting and doctor blade processing have demonstrated that the particle alignment and distribution at low filler loading is critical to achieving maximum mechanical modulus under applied load. The mechanical property improvements measured were also found to be dependent on the xGnP particle size with the larger xGnP-15 particles causing higher modulus than the small sized xGnP-1. At 1 and 5 vol% addition of xGnP-15, the mechanical modulus of the film improved by 25% and 55% respectively. SEM characterization clearly revealed a highly dispersed and aligned network of xGnP-15 particles within the bulk polymer matrix. The incorporation of xGnP-15 also produces a percolated network at low concentration resulting in high electrical conductivity in this insulating LCP polymer.

References:

1) Fukushima H. Graphite nanoreinforcements in polymer nanocomposites. PhD Thesis, Michigan State University, East Lansing, MI, USA, 2003

2) Kyriaki Kalaitzidou *, Hiroyuki Fukushima, Lawrence T. Drzal "Multifunctional polypropylene composites produced by incorporation of exfoliated graphite nanoplatelets" Carbon 45 (2007) 1446–1452

3) Kim. S., Drzal. L. T., Composites Science and Technology, 2009, 294, 196-205

4) Jiang. X., Drzal. L.T., Polymer Composites, Early view, 10.1002/pc.20896

5) Lu. J., Do. I., Drzal. L.T., Worden. R.M., Lee. I., ACS Nano, 2008, 2, 1825-1832

6) Lu. J., Drzal. L.T., Worden. R.M., Lee. I., Chemistry of Materials, 2007, 19, 6240-6246

7) Jacob N. Israelachvili., "Intermolecular and Surface Forces", Science, 1991

8) Peter J Collings and Michael Hird, "Introduction to liquid crystals" Published 1997 CRC Press

9) J.M.Geary, J.W.Goodby, A.R.Kmetz, and J.S.Patel "The mechanism of polymer alignment in liquid crystal polymer" J. Applied Physics,1987,62, 4100-4108

10) K. Hongladarom and W. R, Burghardt, S. G. Baek, S. Cementwala, and J. J. Magda, "Molecular Alignment of Polymer Liquid Crystals in Shear Flows" Macromolecules 1993, 26, 772-784

11) Hamley I.W.1; Davidson P.; Gleeson A.J. "Shear-induced layer alignment in the smectic phase of a side chain liquid crystal polymer" Polymer, 1999, 40, 3599-3603.

12) Kalaitzidou. K., Fukushima H., Askeland P., Drzal L. T., Journal of Materials Science, 2008, 43, 2895-2907